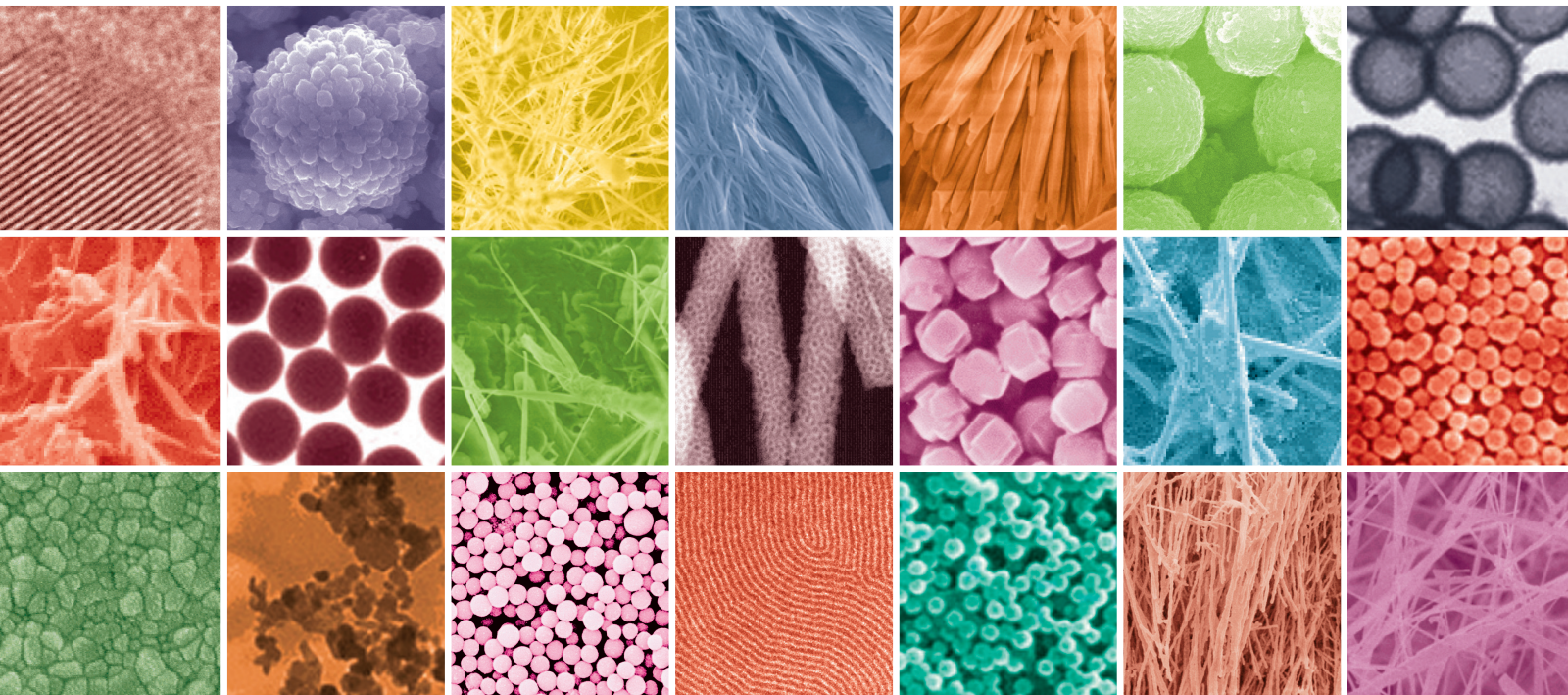


Nanostructured Bioceramics

Guest Editors: Eng San Thian, Jie Huang, Mamoru Aizawa,
and Sander Leeuwenburgh





Nanostructured Bioceramics

Journal of Nanomaterials

Nanostructured Bioceramics

Guest Editors: Eng San Thian, Jie Huang, Mamoru Aizawa,
and Sander Leeuwenburgh



Copyright © 2013 Hindawi Publishing Corporation. All rights reserved.

This is a special issue published in "Journal of Nanomaterials." All articles are open access articles distributed under the Creative Commons Attribution License, which permits unrestricted use, distribution, and reproduction in any medium, provided the original work is properly cited.

Editorial Board

Katerina E. Aifantis, Greece
Nageh K. Allam, USA
Margarida Amaral, Portugal
Xuedong Bai, China
Lavinia Balan, France
Enrico Bergamaschi, Italy
Theodorian Borca-Tasciuc, USA
C. Jeffrey Brinker, USA
Christian Brosseau, France
Xuebo Cao, China
Shafiq Chowdhury, USA
Kwang-Leong Choy, UK
Cui Chunxiang, China
Miguel A. Correa-Duarte, Spain
Shadi A. Dayeh, USA
Claude Estourns, France
Alan Fuchs, USA
Lian Gao, China
Russell E. Gorga, USA
Hongchen Chen Gu, China
Mustafa O. Guler, Turkey
John Zhanhu Guo, USA
Smrati Gupta, Germany
Michael Harris, USA
Zhongkui Hong, China
Michael Z. Hu, USA
David Hui, USA
Y.-K. Jeong, Republic of Korea
Sheng-Rui Jian, Taiwan
Wanqin Jin, China
Rakesh K. Joshi, UK
Zhenhui Kang, China
Fathallah Karimzadeh, Iran
Alireza Khataee, Iran

Do Kyung Kim, Korea
Alan K. T. Lau, Hong Kong
Burtrand Lee, USA
Jun Li, Singapore
Benxia Li, China
Xing-Jie Liang, China
Shijun Liao, China
Gong Ru Lin, Taiwan
J.-Y. Liu, USA
Tianxi Liu, China
Jue Lu, USA
Songwei Lu, USA
Daniel Lu, China
Ed Ma, USA
Gaurav Mago, USA
Santanu K. Maiti, India
Sanjay R. Mathur, Germany
Vikas Mittal, UAE
Weihai Ni, Germany
Sherine Obare, USA
Atsuto Okamoto, Japan
Abdelwahab Omri, Canada
Edward Andrew Payzant, USA
Kui-Qing Peng, China
Anukorn Phuruangrat, Thailand
Suprakas Sinha Ray, South Africa
Ugur Serincan, Turkey
Huaiyu Shao, Japan
Donglu Shi, USA
Vladimir Sivakov, Germany
Marinella Striccoli, Italy
Bohua Sun, South Africa
Saikat Talapatra, USA
Nairong Tao, China

Titipun Thongtem, Thailand
Somchai Thongtem, Thailand
Alexander Tolmachev, Ukraine
Valeri P. Tolstoy, Russia
Tsung-Yen Tsai, Taiwan
Takuya Tsuzuki, Australia
Raquel Verdejo, Spain
Mat U. Wahit, Malaysia
Zhenbo Wang, China
Ruiping Wang, Canada
Shiren Wang, USA
Cheng Wang, China
Yong Wang, USA
Jinquan Wei, China
Ching-Ping Wong, Hong Kong
Xingcai Wu, China
Guodong Xia, Hong Kong
Zhi Li Xiao, USA
Ping Xiao, UK
Yangchuan Xing, USA
Shuangxi Xing, China
N. Xu, China
Doron Yadlovker, Israel
Yingkui Yang, China
Khaled Youssef, USA
Kui Yu, Canada
William W. Yu, USA
Haibo Zeng, China
Tianyou Zhai, Japan
Renyun Zhang, Sweden
Bin Zhang, China
Yanbao Zhao, China
Lianxi Zheng, Singapore
Chunyi Zhi, Hong Kong

Contents

Nanostructured Bioceramics, Eng San Thian, Jie Huang, Mamoru Aizawa, and Sander Leeuwenburgh
Volume 2013, Article ID 594060, 1 page

An Investigation of Optimum NLC-Sunscreen Formulation Using Taguchi Analysis, Pao Chi Chen, Jun-Wei Huang, and Jimmy Pang
Volume 2013, Article ID 463732, 10 pages

Hierarchical Structures and Shaped Particles of Bioactive Glass and Its *In Vitro* Bioactivity, U. Boonyang, F. Li, and A. Stein
Volume 2013, Article ID 681391, 6 pages

β -Tricalcium Phosphate Micron Particles Enhance Calcification of Human Mesenchymal Stem Cells *In Vitro*, Yusuke Nakagawa, Takeshi Muneta, Kunikazu Tsuji, Shizuko Ichinose, Yasuharu Hakamatsuka, Hideyuki Koga, and Ichiro Sekiya
Volume 2013, Article ID 426786, 13 pages

Polymer-Assisted Hydrothermal Synthesis of Hierarchically Arranged Hydroxyapatite Nanoceramic, A. Joseph Nathanael, Sung Soo Han, and Tae Hwan Oh
Volume 2013, Article ID 962026, 8 pages

Preparation of CaO-SiO₂ Glass-Ceramic Spheres by Electrospraying Combined with Sol-Gel Method, Hirotaka Maeda, Yuki Nakano, and Toshihiro Kasuga
Volume 2013, Article ID 463048, 5 pages

Preparation and *In Vitro* and *In Vivo* Performance of Magnesium Ion Substituted Biphasic Calcium Phosphate Spherical Microscaffolds as Human Adipose Tissue-Derived Mesenchymal Stem Cell Microcarriers, Dong-Hyun Kim, Tae-Wan Kim, Ju Dong Lee, Keun-Koo Shin, Jin Sup Jung, Kyu-Hong Hwang, Jong Kook Lee, Hong-Chae Park, and Seog-Young Yoon
Volume 2013, Article ID 762381, 9 pages

The Investigation of Bioactivity and Mechanical Properties of Glass Ionomer Cements Prepared from Al₂O₃-SiO₂ Glass and Poly(γ -glutamic acid), Jinkun Liu, Yoshimitsu Kuwahara, Yuki Shirosaki, and Toshiki Miyazaki
Volume 2013, Article ID 168409, 6 pages

Mineralization and Osteoblast Cells Response of Nanograde Pearl Powders, Jian-Chih Chen, Jung-Chang Kung, Chih-Hsin Hsieh, Mei-Ju Hou, Chi-Jen Shih, and Chun-Cheng Hung
Volume 2013, Article ID 752863, 7 pages

Fabrication of Novel Biodegradable α -Tricalcium Phosphate Cement Set by Chelating Capability of Inositol Phosphate and Its Biocompatibility, Toshiisa Konishi, Minori Mizumoto, Michiyo Honda, Yukiko Horiguchi, Kazuya Oribe, Hikaru Morisue, Ken Ishii, Yoshiaki Toyama, Morio Matsumoto, and Mamoru Aizawa
Volume 2013, Article ID 864374, 11 pages

Editorial

Nanostructured Bioceramics

Eng San Thian,¹ Jie Huang,² Mamoru Aizawa,³ and Sander Leeuwenburgh⁴

¹ Department of Mechanical Engineering, National University of Singapore, Singapore 117576

² Department of Mechanical Engineering, University College London, London WC1E 7JE, UK

³ Department of Applied Chemistry, Meiji University, Kawasaki 2148571, Japan

⁴ Department of Biomaterials, Radboud University Medical Center, 6500 HB Nijmegen, The Netherlands

Correspondence should be addressed to Eng San Thian; mpetes@nus.edu.sg

Received 22 September 2013; Accepted 22 September 2013

Copyright © 2013 Eng San Thian et al. This is an open access article distributed under the Creative Commons Attribution License, which permits unrestricted use, distribution, and reproduction in any medium, provided the original work is properly cited.

With an increase in the world's population, there are enormous demands annually for various biomedical implants to repair diseased or lost tissues. Conventional tissue replacement materials such as autografts and allografts are associated with several problems, which have triggered the development of novel bioceramic materials during the past three decades. However, it is clear that bioceramics used in a wide range of medical applications still require further improvement. Conventional bioceramics traditionally have maintained a physical function without eliciting specific host tissue responses, whereas modern bioceramics are designed to provide a positive interaction with the host tissue. In that respect, nanobioceramics have become particularly appealing to improve the functionality of conventional microstructured bioceramics in terms of bioactivity and mechanical properties.

This special issue is dedicated to the recent advances in the field of nanobioceramics. The issue includes a contribution by U. Boonyang et al., on the fabrication of bioactive glass particles with controllable structure and porosity via a dual-templating technique. Another research article by Y. Nakagawa and his group investigated the biological effects of β -tricalcium phosphate particles on the proliferation, toxicity, and calcification of mesenchymal stem cells. A. J. Nathanael et al. at Yeungnam University, Korea, synthesised and studied flower-like hydroxyapatite nanostructures via a polymer-assisted hydrothermal technique. H. Maeda's group at Nagoya Institute of Technology, Japan, fabricated and studied CaO-SiO₂ glass-ceramic spheres with nanosized pores via an electrospray technique. D.-H. Kim et al. demonstrated the potential of using porous spherical magnesium-substituted

biphasic calcium phosphate scaffolds as stem cell microcarriers. J. Liu and his group from Kyushu Institute of Technology, Japan, studied the bioactivity and mechanical properties of glass ionomer cement prepared from Al₂O₃-SiO₂ glass and poly(γ -glutamic acid). A research article by J.-C. Chen et al. from Kaohsiung Medical University, Taiwan, studied the biological properties of pearl nanocrystallites. Finally, T. Konishi et al. developed and studied a biodegradable α -tricalcium phosphate cement based on chelating capability of inositol phosphate.

Acknowledgments

The editors would like to thank all authors for their contributions to this special issue. In addition, we would like to acknowledge all reviewers for their valuable contributions and dedicated services in the peer review process of the manuscripts submitted to this issue.

*Eng San Thian
Jie Huang
Mamoru Aizawa
Sander Leeuwenburgh*

Research Article

An Investigation of Optimum NLC-Sunscreen Formulation Using Taguchi Analysis

Pao Chi Chen,^{1,2} Jun-Wei Huang,¹ and Jimmy Pang³

¹ Department of Chemical and Materials Engineering, Lunghwa University of Science and Technology, No. 300, Section 1, Wanshou Road, Guishan, Taoyuan 333, Taiwan

² Taiwan Shine Tide Biotech Co., 6F-11, No. 1180, Zhongzheng Road, Zhonghe, New Taipei City 235, Taiwan

³ Taiwan AC Scientific Inc., 6F-5, No. 82, Section 2, Sin Sheng S. Road, Taipei 106, Taiwan

Correspondence should be addressed to Pao Chi Chen; chenpc@mail2000.com.tw

Received 9 April 2013; Accepted 1 August 2013

Academic Editor: Jie Huang

Copyright © 2013 Pao Chi Chen et al. This is an open access article distributed under the Creative Commons Attribution License, which permits unrestricted use, distribution, and reproduction in any medium, provided the original work is properly cited.

This study used three kinds of wax and three kinds of oil, with fixed mixture ratio including UV-blocking materials of ethylhexyl methoxycinnamate, oxybenzone, and avobenzone, and applied hot high-pressure homogenization process to prepare nanolipid sunscreen formulations. The measured particle size of the sunscreen formulations was 100~300 nm around PDI of 0.2 having a moderate polydisperse system. The distribution of zeta potential was -50 mV to -35 mV, showing a stable system. The UV light-absorbing range of 9 groups of sunscreen formulations was 275 nm~380 nm ranging within UVA and UVB. The rheological analysis found that the viscosity change is shear, thinning exhibiting colloid behavior. Taguchi analysis found that the optimum combinations are the carnauba wax and the blackcurrant oil combination for crystallinity and the beeswax and CPG oil for UV absorption. In addition, UV-blocking ability shows that the SPF was 51.5 and PFA was three stars for SU9 formulation. Finally, the effect of temperature on the properties of sunscreen formulations was also explored.

1. Introduction

Nanostructured lipid carriers (NLC), which are expected to become an important carrier of cosmetics and medicine in the future, are at present used for skin care and treatment. Since their introduction to the market in 2005, they have attracted wide attention, which has led to numerous studies of their possible applications [1, 2]. With continuous development, the drug-loading capacity and storage stability of a medicine can be improved. By overcoming the defects of previous liposomes, the percutaneous absorption of a medicine or its principal composition can be improved, and any side effects can be reduced. Numerous studies have indicated the medicament forms of lipid carriers in recent decades [3], such as liposomes and O/W emulsion. Liposomes can be made into micro emulsion, multiple emulsion and solid particles, well combined with excipient; they can be made in quantity. Although the liposome protects the active compound inside the capsule from chemical degradation and regulates and controls the release effect of the compound, it is difficult to

store [1]. The substance inside the capsule leaks rapidly, and the reaction of the hydrophilic substance inside the capsule with the bilaminar membrane makes the structure unstable. The substance inside the capsule cannot be covered stably, and the substance inside the liposome is unstable, thereby limiting the application of liposome.

In order to remedy the defects of liposome, a new carrier was developed in 1990. Solid lipid nanoparticles (SLNs) are a solid colloidal particle drug delivery system with a particle size of 50~1000 nm, which uses solid-state natural or synthetic lipids as the carrier [4-12]. These lipids are biodegradable and are tolerated by the human body. The preparation process of SLN is free of organic solvent, the drug leakage amount is minimal, and it is convenient for mass production, thus making it a promising drug delivery system. In general, SLNs are composed of 0.1% (w/w) to 30% (w/w) solid lipid dispersed in an aqueous medium and if necessary stabilized with preferably 0.5% (w/w) to 5% (w/w) surfactant. However, SLN has some drawbacks: a single solid lipid forms lipid crystal, which limits its drug loading capacity. It changes to

perfect crystal gradually, and the drug is pushed out of the lattice during storage [13].

As the use of SLN is limited, NLC was developed in 2000. NLC is made of mixed lipids, and the liquid lipids are mixed in different physical states into the solid lipid and mixed with aqueous phase [4]. The addition of a liquid phase can disorder the regular lattice structure of solid lipid; increasing the ratio of the irregular crystallographic form in the nanoparticle structure, as well as the spatial content loading fat-soluble drug, enhances the drug loading capacity of the carrier. NLC then maintains the advantages of SLN, and its stability is enhanced. The encapsulation of actives in NLC can be found in the literature on medicine and cosmetic applications [1, 14–17].

In addition, NLC represents a breakthrough from the old emulsification technology. For example, there was only the W/O or O/W emulsion forms in the past; however, with NLC technology the solid lipid and the liquid lipid are mixed in the water solution of the surfactant. Furthermore, as the molecules of all the old emulsions had large particle sizes, when they covered the skin surface, the moisture inside the skin evaporated from the pores between the particles, thus rendering the moisture retention inefficient. NLC forms stable fine particles, which improves both the touch feeling and moisture retention. The effects of lipids, surfactants, and storage conditions on the stability of NLC have been reported in the literature [18, 19]. In addition, for cosmetic applications, the adjustment of the formulation to enhance the mechanical barrier and lubricating effect of lipid nanoparticles can protect against skin scratching in the case of skin irritation or an allergic reaction [18]. This is mainly controlled by the selection of the type of lipids and surfactants used for the production of the nanoparticles, which influences the particle size, zeta potential, occlusion, and crystallinity [2, 4, 19]. For example, tripalmitin and tristearin are high purity lipids which create high occlusions, while tricaprln and trilaurin do not show the occlusive effect [2].

The application of NLC for sunscreen formulations with a high sun protection factor (SPF) is a new development. The studies on sunscreen formulations found in the literature [13, 20, 21] report that increased crystallinity improves the UV-blocking effect and that the particulate character also acts as a UV blocker. The incorporation of molecular sunscreen into the particle matrix leads to a synergistic effect for both the molecular sunscreen and UV scattering by the particles [4]. Sunlight contains infrared rays, visible light, and ultraviolet radiation. The most harmful for the human body is ultraviolet radiation, which is divided into UVA, UVB, and UVC. UVB (wavelength 290–320 nm) has higher energy, and as it only reaches the cubicle layer of the skin, the skin turns red and burns. Sunburned skin has pigment precipitate; thus, the horny layer is thickened and the skin is darker. UVA (wavelength 320–420 nm) has a lower energy but is more penetrative; it can penetrate through glass into the dermal layer of the skin. It also stimulates the overgrowth of melanocytes, so that melanins accumulate and spots form when the accumulation is large enough. In addition, the collagen fiber and elastic fiber are destroyed, which causes atrophy. Thus, the skin lacks moisture and elasticity and

becomes flabby and wrinkly. UVC has the highest energy, but it is shielded by the ozonosphere and does not reach the ground. The harm caused by UVA and UVB to the human body is the main concern.

The common evaluation methods for the sun-protection ability of products include (1) sun protection factor (SPF) value-based evaluation and (2) UVA-protection factor (PFA) value-based evaluation. The SPF value is determined by an evaluation of the sunburned red spots and PFA by the degree of suntan. There are physical sunscreens and chemical sunscreens used in sunscreen formulations. The physical sunscreen uses powder to reflect or scatter ultraviolet. In chemical sunscreens the product is mixed with ultraviolet absorbent which can effectively filter the ultraviolet source in the sunlight and let other nonharmful light sources pass through. The physical sunscreen ingredients are mainly made of inorganic powders, such as TiO₂, ZnO, silica, and ZrO. TiO₂ and ZnO are the ones most commonly used. The chemical sunscreen ingredients are mainly made of chemosynthetic esters, known as ultraviolet absorbents for example, para aminobenzoic acid, salicylates, cinnamates, benzophenones and other ultraviolet absorbing ingredients.

The disadvantage of physical powder sun-screening agents is that they block pores and obstruct the natural permeability of the skin, so the skin loses gloss and elasticity. The experiment herein used chemical sun-screening agent and NLC to minimize the pore blocking, and the chemical composition of the sun-screening agent improved the quality of traditional sun-screening agent as well as the drug loading capacity [20]. Most sunscreen formulations on the market are micron-sized single physical sunscreen products consisting of submicron particles (smaller than 50 nm), which are likely to block pores and have a greasy feeling. NLC can reduce the drug release so that the product is not greasy; thus, it has become the mainstay for cosmeceutical products. Therefore, this study used NLC as the carrier in the sunscreen formulations in order to add to the technology of NLC applications and to develop a new formula of sunscreen formulations at the same time. This study is important for the application of NLC and the development of a new formula. The purposes of this work were to find the most appropriate combination of three kinds of wax and three kinds of oil as reference for sunscreen formulations by using Taguchi analysis [22], to examine the stability of sunscreen formulations, to determine the SPF of the sunscreen formulations, and to find the structure of NLC obtained in this study.

2. Materials and Methods

2.1. Experimental Design. The experimental compositions shown in Table 1 include oil, wax, pentylene glycol, decyl glucoside, lecithin, water, and the UV-protection agents of S1, S2, and S3. S1, S2, and S3 denote 4-methoxy-cinnamic acid-2-ethylhexyl ester, phenyl ketone-3, and avobenzone, ingredients which resist UVA and UVB. In addition, the oil and wax were those common in the literature, such as echium lycopis oil, blackcurrant oil, and CPG oil and carnauba wax, Compritol 888 ATO, and beeswax. This experiment tested three kinds of oil and wax, using a thermal high-pressure

TABLE 1: NLC-sunscreen formulation conducted in this work (in wt.%).

B(oil) (mL)	A(wax) (g)	S1 (mL)	S2 (g)	S3 (g)	Pentylene glycol (mL)	Decyl glucoside (mL)	Water (mL)	Lecithin (g)
17%	10%	5.2%	3.5%	1.3%	2%	4.5%	56%	0.5%

TABLE 2: Orthogonal table showing levels of wax and oil*.

Series	A(wax)	B(oil)
SU1	Carnauba wax(1)	Echium lycopsis oil(1)
SU2	Carnauba wax(1)	Blackcurrant oil(2)
SU3	Carnauba wax(1)	CPG oil(3)**
SU4	Compritol 888 ATO(2)	Echium lycopsis oil(1)
SU5	Compritol 888 ATO(2)	Blackcurrant oil(2)
SU6	Compritol 888 ATO(2)	CPG oil(3)
SU7	Beeswax(3)	Echium lycopsis oil(1)
SU8	Beeswax(3)	Blackcurrant oil(2)
SU9	Beeswax(3)	CPG oil(3)

*1, 2, and 3 indicate the level of parameter.

** A kind of triglyceride oil which is extracted from natural plants.

homogenization method (APV, APV2000). The prepared sunscreen formulations were characterized by instrument analysis using a UV/vis analyzer (Jusco, V-670) for UV-absorbance, TGA/DSC (TA, SDT-600) for thermal data analysis, particle-size analyzer (Malvern, Zetasizer, Nano-ZS) for particle-size measurement, zeta-potential meter (Malvern, Zetasizer, Nano-ZS) for stability analysis, TEM (JEM, 2100) for structure analysis, and a rheology meter (Malvern, Gemini2 Rotonetic™ Drive2) for viscosity and dynamic analysis. The number of experiments is shown in Table 2, which is an orthogonal table from the Taguchi experimental design. The optimal set values of the parameters were determined through experiment, according to the different factor numbers and level numbers of the various factors.

2.2. Experimental Procedures and Methods. The operating conditions of mixture ratio, temperature, and pressure were fixed: 5 min preemulsification at 8000 rpm and high-pressure homogenization at 800bar were repeated 5 times to produce the sunscreen formulation, while only the oil and wax ingredients were changed. First, the oil phase ingredient and water phase ingredient were heated separately to 85°C; then, the oil phase was added to the water phase, and the temperature was maintained at 85°C. The mixture was put in the homogenizer for preemulsification at rotation speed of 8000 rpm for 5 min, the preemulsified sample was put in the high-pressure homogenizer, and the experiment was conducted at a pressure of 800bar for 5-cycle times. The sunscreen formulation sample was collected and characterized when it cooled to room temperature. In order to compare the effect of storage temperature on the property of NLC, the sample was divided into two parts, with one part kept at 5°C and the other at 25°C. The sunscreen formulation samples were used to examine the particle size, zeta potential, thermal data, UV-absorption, rheological behavior, TEM, and SPF.

3. Results and Discussion

3.1. Absorption Range of NLC-Sunscreen Formulations. Figures 1(a) and 1(b) show the absorption range of the prepared sunscreen formulation measured using UV/Vis on different days: day 1 and day 45. The peaks exhibited marked differences, depending on the formulations. On the first day, the main absorption peaks of SU1~SU9 were 275 nm to 380 nm, as shown in Figure 1(a), for the absorption ranges of UVA and UVB. After 45 days of storage, the measured UV absorption range, as shown in Figure 1(b), was also in the range of 275 nm to 380 nm, meaning that the prepared sunscreen formulation had UV absorption stability. The absorption range obtained here was comparable with the formulations reported in the literature [4]. The absorption peaks for beeswax (SU7, SU8, and SU9) were higher than those for Compritol 888 ATO or carnauba wax. This could be explained from the viewpoint of particle size and crystallinity. The particle size on the first day for beeswax (115–142.3 nm) was smaller than that for Compritol 888 ATO (140.8–160.1 nm) or carnauba wax (180.7–216.7 nm). The larger particles in the Compritol 888 ATO and carnauba wax NLC formulations were able to scatter and reflect incoming UV radiation, resulting in a decrease of outgoing UV light [20]. A similar report was found in the literature [23]. Crystallinity is another factor which affects UV-blocking ability. This phenomenon was reported by Müller et al. [4], who found that highly crystalline solid lipid nanoparticles act as particulate UV blockers by scattering the light efficiently. In the present study, the crystallinity for Compritol 888 ATO (13.57–22.30%) was smaller than that for carnauba wax (52.86–72.98%) or beeswax (47.63–82.54%), leading to a lower UV-blocking ability. The particle size and crystallinity will be discussed later.

3.2. Particle Size of NLC-Sunscreen Formulations. The particle size and its distribution are very important for the stability of the colloid system. This study used a thermal high pressure homogenization method to prepare NLC under changes in oil and wax production and storage temperature. The particle size and PDI are shown in Tables 3 and 4. As shown in Table 3 and Figure 2, the particle size was about 110~210 nm on the first day; for all systems, the particle size at 5°C was smaller than that at 25°C. In addition, for all particles, the size increased with an increase in storage time, most significantly at a 25°C storage temperature. Generally, the wax affecting the particle size in order of significance was carnauba wax > Compritol 888 ATO > beeswax. Using SU1 (carnauba waxes) as an example, as shown in Table 3 and Figure 2, the sizes were 216.7 nm, 410.2 nm, and 507.1 nm for day 1, day 30, and day 60, respectively. This indicated that the particles became aggregates with increased storage time. On the other hand, for SU7 (beeswax), the sizes were 142.3 nm (day 1), 147.5 nm

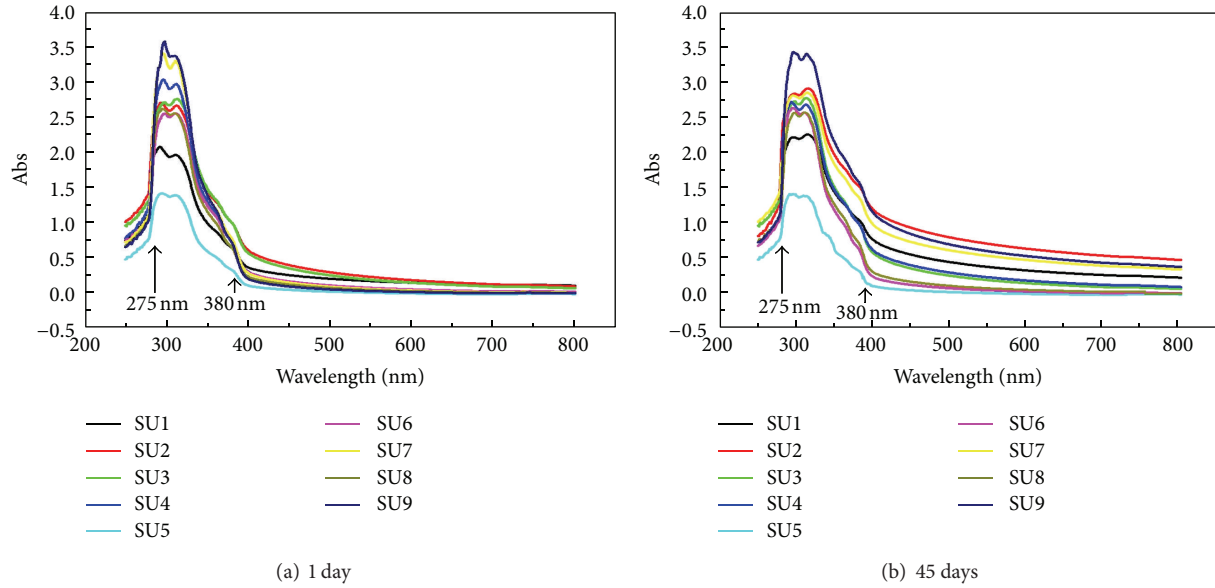


FIGURE 1: SU1~SU9 UV absorption peaks at different days, showing the stability of sunscreen formulation obtained in this work.

TABLE 3: Particle size at different storage times.

	d (nm) (day 1)	d (nm) (day 30)		d (nm) (day 60)	
		5°C	25°C	5°C	25°C
SU1	216.7 ± 20.96	235 ± 2.458	410.2 ± 10.4	253.9 ± 6.03	507.1 ± 8.10
SU2	180.7 ± 9.763	248.7 ± 3.15	250.9 ± 5.10	323.5 ± 8.61	310.3 ± 9.72
SU3	185.2 ± 3.798	266.8 ± 0.77	304.1 ± 4.91	303.1 ± 5.78	306.8 ± 4.22
SU4	140.8 ± 6.165	185.5 ± 5.08	182.8 ± 3.55	186.3 ± 3.87	195.3 ± 3.50
SU5	145.4 ± 9.296	191.6 ± 4.2	210.3 ± 4.36	182.3 ± 4.32	222.4 ± 6.10
SU6	160.1 ± 7.204	205.2 ± 4.65	244.1 ± 3.87	208.5 ± 4.45	314.8 ± 11.2
SU7	142.3 ± 4.120	142.9 ± 3.89	147.5 ± 3.10	143.2 ± 4.39	154.5 ± 4.39
SU8	127.9 ± 1.931	145.1 ± 4.47	151.8 ± 2.66	150.5 ± 5.26	156.2 ± 4.33
SU9	115.5 ± 2.951	141.7 ± 2.61	143.4 ± 2.27	153.6 ± 3.25	149.8 ± 4.36

(day 30), and 154.5 nm (day 60), indicating little change in size, with more stable formulations obtained from beeswax as compared with those from the other waxes.

The PDI value shows the distribution of particle size. Monodispersion occurs when the PDI is less than 0.05; it approaches monodispersion at a PDI of less than 0.08. A moderate dispersion system has 0.08~0.7 PDI, and a multidispersion system has PDI greater than 0.7. Table 4 shows the PDI values of NLC. As seen, the PDI value was about 0.1 on the first day, except for the carnauba wax formulations; thus, the prepared NLC was a moderate dispersion system, which remained within 0.2 for most samples after long-time storage. The samples had a consistent particle size, indicating that the prepared sunscreen formulations had particle size distribution and size stability.

3.3. Zeta Potential (ζ) of NLC-Sunscreen Formulations. The physical stability of NLC can be evaluated by measuring the zeta potential. According to the theory of DLVO, a system can be regarded as stable if the electrostatic repulsion dominates

the attractive van der Waals forces [18]. Generally, a zeta potential above $|30|$ mV means that the colloidal system is in a stable state [15]. There is less particle aggregation because of the electrostatic repulsion between colloidal particles. According to the literature, a zeta potential of $|60|$ mV means that the colloidal system has super high stability, a zeta potential of $|15|$ mV means that the colloidal particles may have aggregation, and a zeta potential below $|5|$ mV means that the colloidal particles have severe aggregation.

Data in Table 5 and Figure 3 show that the zeta potential value was about -40 mV after preparation, which is considered particle dispersion with good stability. The interface potential value did not change significantly after long-term storage, indicating that the prepared NLC had good stability. The effects of storage temperature and long-term storage on the zeta potential were compared. Although temperature affects the zeta potential, the NLC prepared in the experiment stayed above -35 mV, whether it was stored at 25°C or 5°C, and was in a stable colloid distribution state. In addition, the zeta potential for beeswax was higher than that for carnauba

TABLE 4: PDI for various materials at different storage times.

	PDI (day 1)	PDI (day 30)		PDI (day 60)	
		5°C	25°C	5°C	25°C
SU1	0.349 ± 0.035	0.264 ± 0.04	0.400 ± 0.01	0.305 ± 0.03	0.408 ± 0.01
SU2	0.186 ± 0.015	0.164 ± 0.05	0.176 ± 0.01	0.281 ± 0.01	0.164 ± 0.01
SU3	0.185 ± 0.007	0.179 ± 0.01	0.215 ± 0.02	0.143 ± 0.01	0.201 ± 0.01
SU4	0.076 ± 0.002	0.097 ± 0.03	0.098 ± 0.02	0.119 ± 0.01	0.074 ± 0.02
SU5	0.057 ± 0.015	0.125 ± 0.02	0.161 ± 0.01	0.109 ± 0.01	0.099 ± 0.03
SU6	0.090 ± 0.046	0.137 ± 0.01	0.154 ± 0.03	0.166 ± 0.01	0.138 ± 0.02
SU7	0.202 ± 0.025	0.095 ± 0.01	0.096 ± 0.02	0.080 ± 0.02	0.129 ± 0.01
SU8	0.082 ± 0.003	0.105 ± 0.02	0.124 ± 0.01	0.113 ± 0.02	0.144 ± 0.01
SU9	0.078 ± 0.008	0.083 ± 0.01	0.095 ± 0.01	0.077 ± 0.02	0.099 ± 0.01

TABLE 5: Zeta-potentials for various samples at different storage times.

	ζ (mV) (day 1)	ζ (mV) (day 30)		ζ (mV) (day 60)	
		5°C	25°C	5°C	25°C
SU1	-28.4 ± 0.987	-29.3 ± 1.03	-35.2 ± 0.99	-35.7 ± 2.00	-36.8 ± 1.65
SU2	-27.5 ± 1.160	-45.9 ± 0.69	-35.8 ± 0.38	-40.4 ± 1.60	-37.0 ± 1.45
SU3	-33.5 ± 0.240	-39.5 ± 0.50	-46.6 ± 0.46	-42.5 ± 0.55	-45.8 ± 0.61
SU4	-28.0 ± 1.41	-38.1 ± 0.99	-45.5 ± 0.9	-38.9 ± 1.45	-37.4 ± 1.75
SU5	-32.0 ± 2.76	-39.0 ± 2.70	-46.6 ± 0.45	-34.4 ± 0.97	-44.1 ± 0.49
SU6	-31.5 ± 0.70	-40.4 ± 1.31	-42.6 ± 1.65	-38.1 ± 1.28	-40.2 ± 1.06
SU7	-32.5 ± 2.65	-49.2 ± 0.61	-50.6 ± 1.37	-42.1 ± 1.63	-40.5 ± 2.07
SU8	-18.1 ± 1.03	-56.8 ± 0.30	-58.6 ± 1.03	-44.9 ± 0.96	-45.1 ± 2.45
SU9	-15.1 ± 1.84	-54.4 ± 1.31	-52.9 ± 1.12	-38.8 ± 1.25	-36.6 ± 1.25

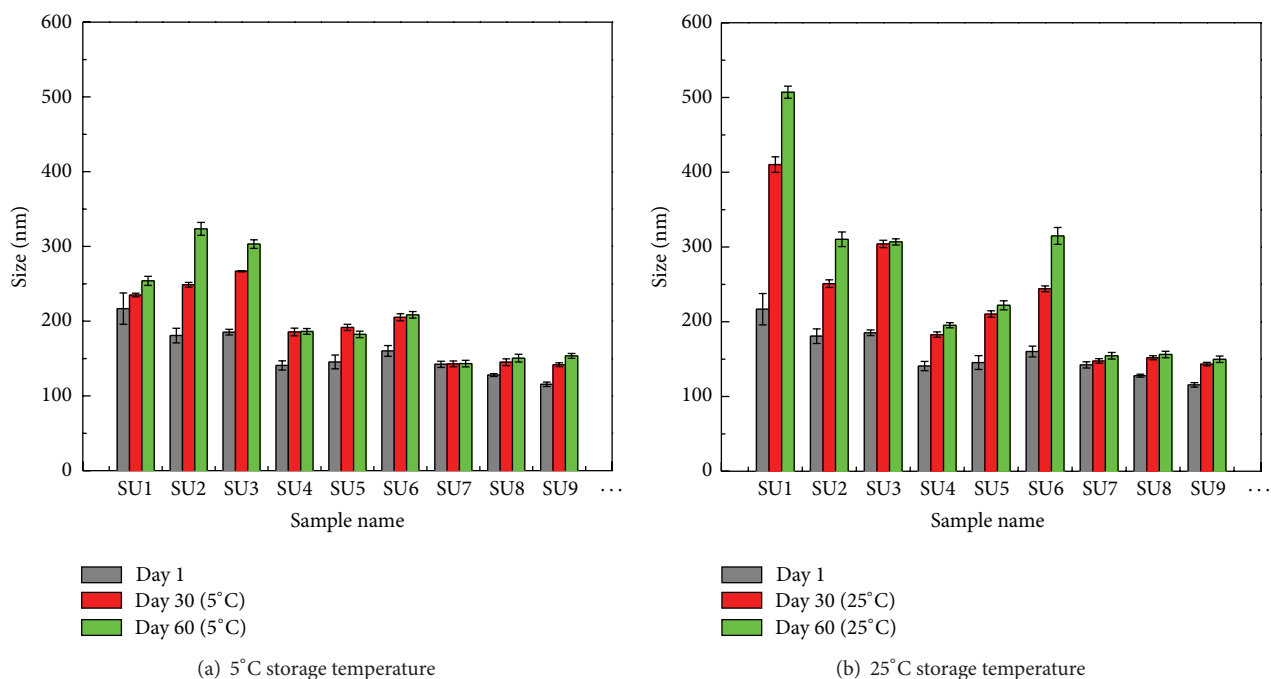


FIGURE 2: Particle size variations of different materials and storage at different temperatures.

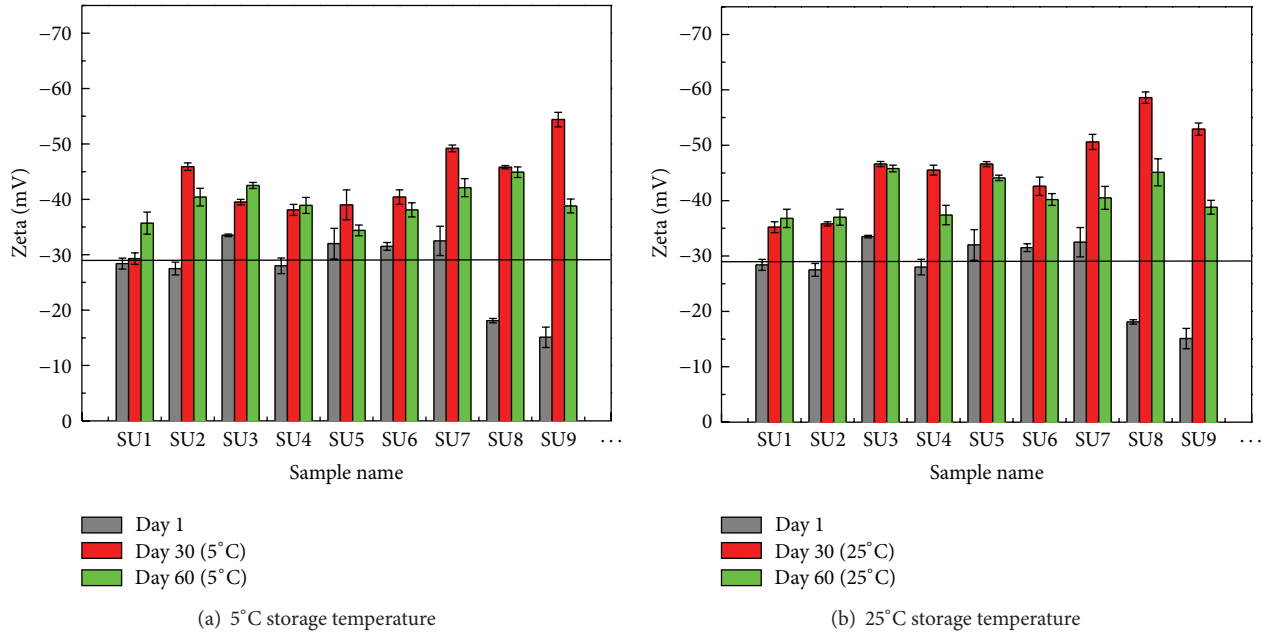


FIGURE 3: Zeta-potential variations of different materials and storage at different temperatures.

TABLE 6: Comparison of NLC crystallinity under different conditions.

Sample	MP (°C)	ΔH (J/g)	CI (%)
SU1	76.60	21.23	52.86
SU2	77.80	29.31	72.98
SU3	76.51	24.31	60.56
SU4	62.08	13.09	13.57
SU5	61.02	21.52	22.30
SU6	59.82	14.69	15.22
SU7	67.10	6.43	82.54
SU8	67.45	3.71	47.63
SU9	67.33	3.80	48.78

wax or Compritol 888 ATO after storage. In addition, the systems obtained herein were more stable as compared with SLN systems, with a zeta-potential range of (−37.9 mV)–(−18.8 mV) for the three oils [5]. This also demonstrated that NLC had more stability than SLN.

3.4. Crystallinity Index (CI) of NLC-Sunscreen Formulations.

The structure of a material varies with heating. This study used DSC to measure the variation of samples under heating with a heating rate at 5°C/min for each run after preparation, as shown in Figure 4 for SU1. The variation of the enthalpy and melting point (MP) of the samples was obtained from the heat change, and then the crystallinity index of the samples was determined using enthalpy. The MP and enthalpy for SU1 determined herein were 76.6°C and 21.23 J/g, respectively. All data obtained in this work are listed in Table 6. The data on the variations were quite different, depending on the formulations. As for the three kinds of solid lipid used in this

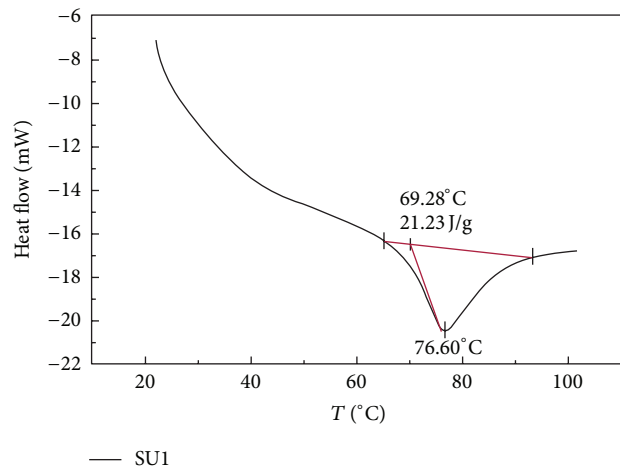


FIGURE 4: Determination of MP and enthalpy of NLC by using DSC analysis.

study, the melting point of carnauba wax was 85.56°C and that of the enthalpy was 40.16 J/g. The melting point of Compritol 888 ATO was 74.76°C and that of the enthalpy was 96.49 J/g. The melting point of beeswax was 81.17°C and that of the enthalpy was 7.79 J/g. If the crystallinity index of solid lipid material was 100%, the crystallinity index of other samples could be deduced. The CI is defined as follows [18]:

$$CI (\%) = \left(\frac{\Delta H_{NLC}}{\Delta H_{lipid}} \right) \times 100\%, \quad (1)$$

where ΔH_{NLC} represents the enthalpy of the prepared sample and ΔH_{lipid} represents the enthalpy of pure wax. As shown in Table 6, the different compositions had different crystallinity

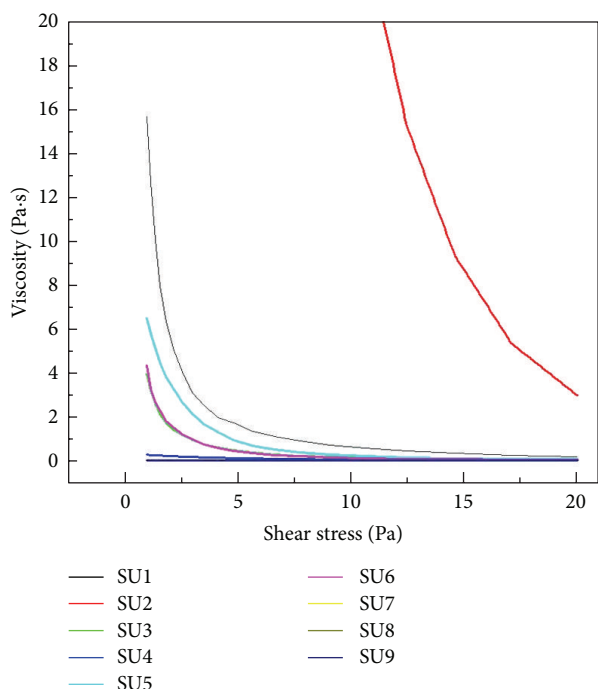


FIGURE 5: Viscosity change is shear thinning.

because different wax types make the crystal arrangement present an incomplete form. A larger crystallinity index improved the UV-blocking effect, as shown in Figure 1, which was similar to that reported in the literature [4, 23]. In the present study, the beeswax NLC was found to be the most efficient.

3.5. Rheological Behavior of NLC-Sunscreen Formulations.

Using a rheology meter (Gemini2 Rotonetic™ Drive2) with a cone-and-plate device, the rheological behavior of the sunscreen formulation could be determined. As shown in Figure 5, the viscosity of the prepared sample decreased as the shear rate increased. This viscosity change can be called shear thinning, as with oil paint. A similar report in the literature showed the shear thinning phenomena for seven sun-blocking formulations [21]. If this sample was applied to sunscreen formulations, it could be smeared on the skin uniformly. Whether the sample is colloid or liquid can be known by measuring its viscosity and elasticity, with the elastic modulus (G') and viscous modulus (G'') obtained by using oscillation frequency to apply interference. When $G' > G''$, it is colloid if $G''' > G'$, it is liquid. The NLC prepared in this experiment was $G' > G''$, as shown in Figure 6, so it was in a colloid state. Figure 6 shows the changes in the viscous modulus and elastic modulus at different temperatures. The viscous modulus increased with the oscillation frequency at low temperature; thus, the colloid behavior at low temperature was more obvious than that at room temperature. The colloid applied to sunscreen formulations could enhance the adhesion of actives to the skin and thus enhance the uniformity of smearing. This is important

TABLE 7: Effects of the CI S/N ratio factor.

Level	A-wax	B-oil
1	35.79	31.82
2	24.42	32.60
3	35.22	31.02
Delta	11.37	1.58
Rank	1	2

for cosmetic products because these products need to create a “nice application feeling” when applied by the customer [4].

3.6. Analysis of Parameter Importance. After the sunscreen formulations were prepared, the particle size, zeta potential, crystallinity, and ultraviolet absorption intensity were tested and then analyzed by Taguchi software. The S/N ratio factors that affect particle size, zeta potential, crystallinity, and ultraviolet absorbance could be obtained from the larger-the-better and the smaller-the-better by the software. First, using CI as an example, the Taguchi analysis results are shown in Figure 7 and Table 7. The parameters affecting the CI in order of importance were carnauba wax > beeswax > Compritol 888 ATO and blackcurrant oil > echium lycopsis oil > CPG oil. Therefore, the optimum combination was SU2, with the ingredients of carnauba wax and blackcurrant oil. The effect of the oil on the recrystallization to stable lipid modifications was found in the literature [4].

Second, the parameters affecting the particle size in order of importance were beeswax > Compritol 888 ATO > carnauba wax and blackcurrant oil > CPG oil > echium lycopsis oil. Therefore, the optimum combination was SU8 for the ingredients of beeswax and blackcurrant oil. Third, the parameters affecting the zeta potential in order of importance were Compritol 888 ATO > carnauba wax > beeswax and echium lycopsis oil > blackcurrant oil > CPG oil. Therefore, the optimum combination was SU4 for the ingredients of Compritol 888 ATO and echium lycopsis oil. Fourth, the parameters affecting the UV absorption value in order of importance were beeswax > carnauba wax > Compritol 888 ATO and CPG oil > echium lycopsis oil > blackcurrant oil. Therefore, the optimum combination was SU9 for the ingredients of beeswax and CPG oil.

Table 8 shows the four dimensions obtained from this study. The optimal composition was obtained from the Taguchi analysis. The basic differences in particle size and zeta potential were small. In terms of sunscreen formulations, crystallinity is the basis of coating UV-blocking material, and UV light absorption is the effect of the sunscreen formulations. Therefore, the sunscreen formulations prepared in this subject focused on crystallinity and UV absorption.

3.7. Determinations of SPF and PFA Values. Herein, SU9 was used for the measurements of SPF for UVB and PFA for UVA, respectively. Optometrics SPF-290S Analyzer according to a US FDA measurement standard, the scan spectrum and monochromatic protection factors (MPF) are shown in Figure 8(a) for twelve time scans. The results showed that SPF

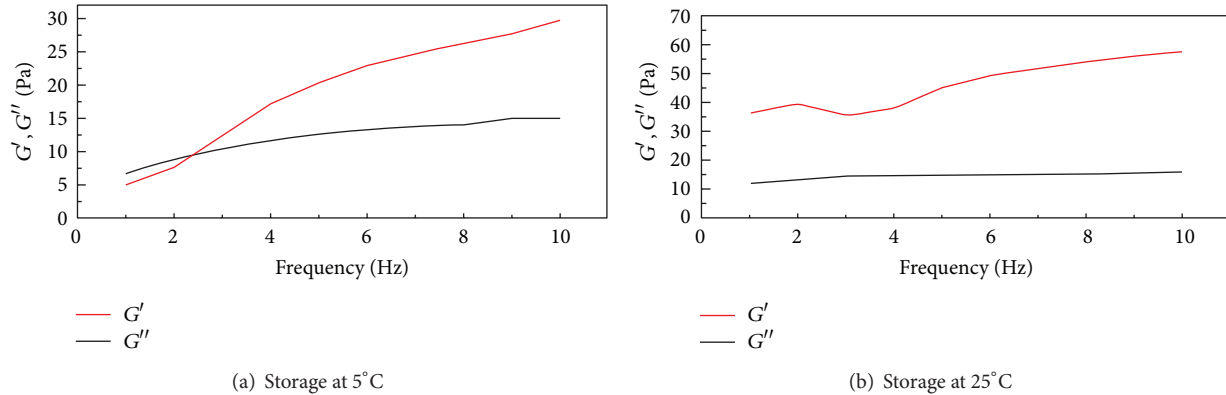
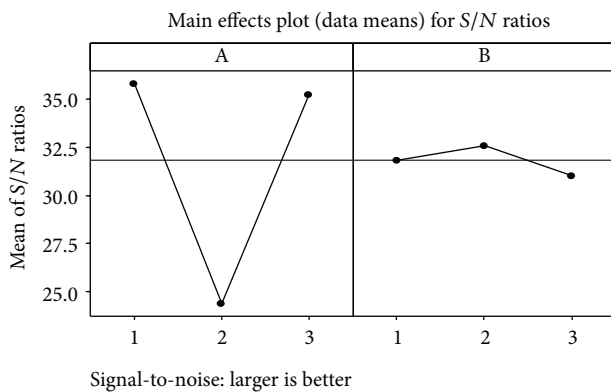


FIGURE 6: Viscoelasticity at different storage temperatures (SU3).

TABLE 8: Optimum combinations obtained from various analyses.

	Particle size	Zeta potential	Crystallinity	UV absorption
Optimum combination	SU8	SU4	SU2	SU9
Wax and oil ingredients	Beeswax Blackcurrant	Compritol 888ATO Echium lycopsis oil	Carnauba wax Blackcurrant	Beeswax CPG oil

FIGURE 7: Effects of the crystallinity S/N ratio factor.

was 51.5 and PFA was three stars, indicating high UVA and UVB protection for the SU9 formulation. In order to prepare a sun protection product for market, we take 30% of SU9 formulation mixed with cream for a modified prescription. The measured SPF and PFA were 25.22, as in the scan spectrum shown in Figure 8(b), for two stars, respectively, indicating moderate UV protection ability. However, the occlusion factors were 98% and 96% for SPFs of 51.5 and 25.22, respectively. The particulate character also acts as a UV blocker. Incorporation of molecular sunscreens into a matrix of particles leads to a synergistic effect of both molecular sunscreen and UV scattering by the particles [4, 20]. SPF investigations were reported by Nesseem [21], who studied seven sunscreen formulations by adjusting the mixture of organic and inorganic UV blockers for an SPF range of 19.97–56.17. However, the results obtained herein demonstrated that

the chemical sunscreen mixture of S1, S2, and S3 in NLC presented a new option for UV blocking in the future.

3.8. Structure of NLC-Sunscreen Formulation. Figure 9(a) shows the TEM photograph of SU9. It was found that the solid lipid matrix contained tiny liquid oil nanocompartments, as compared with Figure 9(b), the multiple type, that is, an oil-in-solid lipid- (fat-) in-water (O/F/W) dispersion system [23]. Therefore, increasing the oil concentration, the solubility of oil molecules in the solid lipid was exceeded, and the oil precipitates in the form of fine droplets were incorporated into the solid lipid matrix, resulting in phase separation and the formation of oil nanocompartments [4]. The phenomena could be found during the cooling process after production of NLC by the hot homogenization process. In this manner, the oil nanocompartments were incorporated into the solid matrix; they contained a higher amount of active compounds, but their release was still controlled by the surrounding solid lipid barrier.

4. Conclusions

This study successfully obtained sunscreen formulations from a combination of three kinds of wax and three kinds of oil by using a hot high-pressure homogenization process. The particle size of the prepared NLC sunscreen formulations was 100–300 nm; low-temperature (5°C) storage was better than room-temperature (25°C) storage. The PDI was about 0.2 of a moderate polydisperse system. Using Taguchi analysis with an S/N ratio for particle size, zeta potential, CI, and VU absorption wave, the optimum formulations were found. The obtained optimum combinations were SU8, SU4, SU2, and SU9 for particle size, zeta potential, CI, and VU absorption wave, respectively. As the particle size and zeta potential

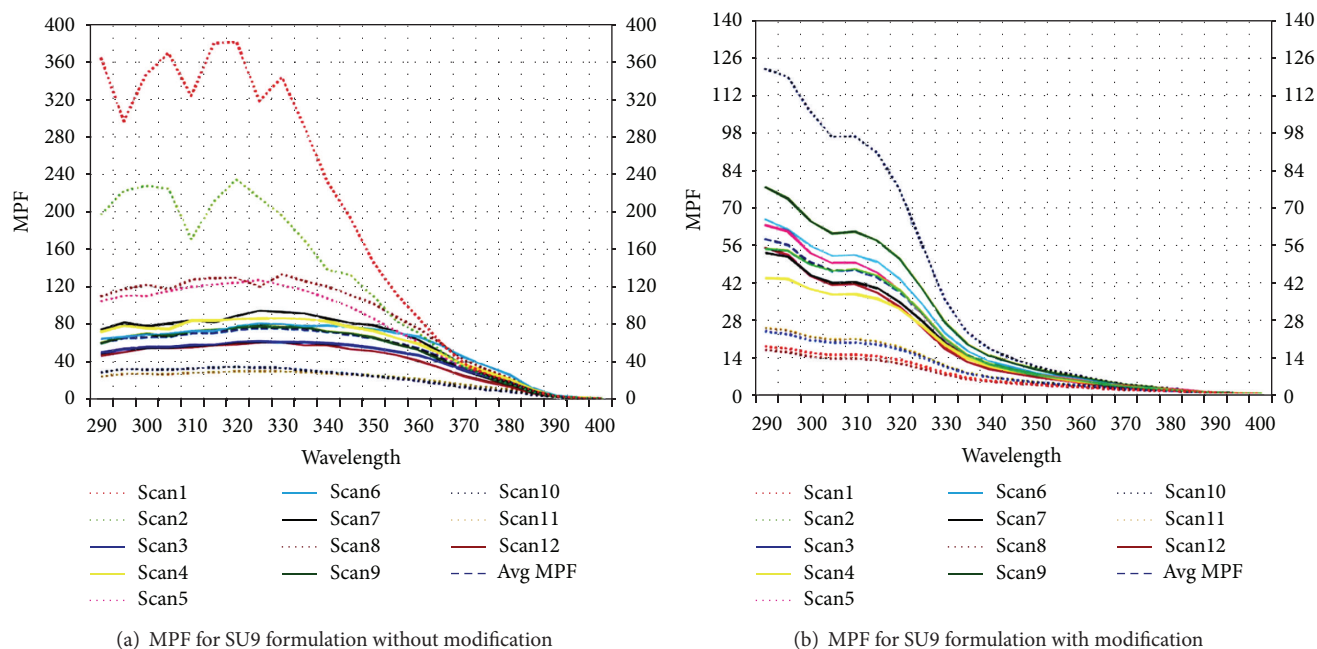
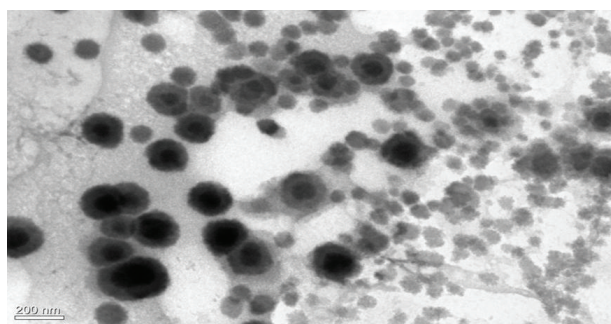
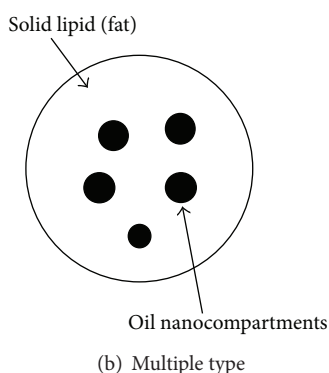


FIGURE 8: Monochromatic protection factors (MPF) for sun protection analysis (SU9) with and without modification.



(a) TEM photograph of SU9



(b) Multiple type

FIGURE 9: TEM photograph of SU9 formulation and multiple type structure of NLC.

presented a stable system, this study took crystallinity and UV light absorption as the basis for the preparation of sunscreen formulations. According to sun protection products on the market, CI and VU-blocking are considered to be better for

sunscreen formulations. The measured SPF and PFA data for SU9 effectively exhibited UV-blocking ability. In addition, the structure of the NLC-sunscreen formulations obtained in this work was that of an O/F/W dispersion system.

Acknowledgments

The authors thank the financial support from Lunghwa University of Science and Technology and Taiwan AC Scientific Inc.

References

- [1] R. H. Müller, R. D. Petersen, A. Hommoss, and J. Pardeike, "Nanostructured lipid carriers (NLC) in cosmetic dermal products," *Advanced Drug Delivery Reviews*, vol. 59, no. 6, pp. 522–530, 2007.
- [2] E. B. Souto and R. H. Müller, "Cosmetic features and applications of lipid nanoparticles (SLN, NLC)," *International Journal of Cosmetic Science*, vol. 30, no. 3, pp. 157–165, 2008.
- [3] J. W. Wiechers, *Science and Applications of Skin Delivery Systems*, chapter 15, Allured Publishing Corporation, 2008.
- [4] R. H. Müller, M. Radtke, and S. A. Wissing, "Solid lipid nanoparticles (SLN) and nanostructured lipid carriers (NLC) in cosmetic and dermatological preparations," *Advanced Drug Delivery Reviews*, vol. 54, 1, pp. S131–S155, 2002.
- [5] K.-C. Kang, N.-H. Jeong, C.-I. Lee, and H.-B. Pyo, "Preparation and characterization of SLNs (W/O/W type) contained lipoic acid PEG ester by variation lipid," *Journal of Industrial and Engineering Chemistry*, vol. 15, no. 4, pp. 529–536, 2009.
- [6] J.-Y. Fang, C.-L. Fang, C.-H. Liu, and Y.-H. Su, "Lipid nanoparticles as vehicles for topical psoralen delivery: solid lipid nanoparticles (SLN) versus nanostructured lipid carriers (NLC)," *European Journal of Pharmaceutics and Biopharmaceutics*, vol. 70, no. 2, pp. 633–640, 2008.

- [7] R. H. Müller, W. Mehnert, J.-S. Lucks et al., "Solid lipid nanoparticles (SLN): an alternative colloidal carrier system for controlled drug delivery," *European Journal of Pharmaceutics and Biopharmaceutics*, vol. 41, no. 1, pp. 62–69, 1995.
- [8] R. H. Müller, K. Mäder, and S. Gohla, "Solid lipid nanoparticles (SLN) for controlled drug delivery: a review of the state of the art," *European Journal of Pharmaceutics and Biopharmaceutics*, vol. 50, no. 1, pp. 161–177, 2000.
- [9] S. Kuchler, M. Abdel-Mottaleb, A. Lamprecht, M. R. Radowski, R. Haag, and M. Schäfer-Korting, "Influence of nanocarrier type and size on skin delivery of hydrophilic agents," *International Journal of Pharmaceutics*, vol. 377, no. 1-2, pp. 169–172, 2009.
- [10] N. Dayan, "Skin barrier: chemistry of skin delivery systems," in *Pathways For Skin Penetration*, J. W. Wiechers, Ed., chapter 3, Allured Publishing Corporation, 2008.
- [11] L. Priano, D. Esposti, R. Esposti et al., "Solid lipid nanoparticles incorporating melatonin as new model for sustained oral and transdermal delivery systems," *Journal of Nanoscience and Nanotechnology*, vol. 7, no. 10, pp. 3596–3601, 2007.
- [12] C. Freitas and R. H. Müller, "Correlation between long-term stability of solid lipid nanoparticles (SLN(TM)) and crystallinity of the lipid phase," *European Journal of Pharmaceutics and Biopharmaceutics*, vol. 47, no. 2, pp. 125–132, 1999.
- [13] R. H. Müller, M. Radtke, and S. A. Wissing, "Nanostructured lipid matrices for improved microencapsulation of drugs," *International Journal of Pharmaceutics*, vol. 242, no. 1-2, pp. 121–128, 2002.
- [14] C. Puglia, P. Blasi, L. Rizza et al., "Lipid nanoparticles for prolonged topical delivery: an in vitro and in vivo investigation," *International Journal of Pharmaceutics*, vol. 357, no. 1-2, pp. 295–304, 2008.
- [15] A. Saupe, S. A. Wissing, A. Lenk, C. Schmidt, and R. H. Müller, "Solid Lipid Nanoparticles (SLN) and Nanostructured Lipid Carriers (NLC): structural investigations on two different carrier systems," *Bio-Medical Materials and Engineering*, vol. 15, no. 5, pp. 393–402, 2005.
- [16] V. Teeranachaideekul, R. H. Müller, and V. B. Junyaprasert, "Encapsulation of ascorbyl palmitate in nanostructured lipid carriers (NLC)-Effects of formulation parameters on physicochemical stability," *International Journal of Pharmaceutics*, vol. 340, no. 1-2, pp. 198–206, 2007.
- [17] M. Üner, S. A. Wissing, G. Yener, and R. H. Müller, "Solid lipid nanoparticles (SLN) and nanostructured lipid carriers (NLC) for application of ascorbyl palmitate," *Pharmazie*, vol. 60, no. 8, pp. 577–582, 2005.
- [18] F. Han, S. Li, R. Yin, H. Liu, and L. Xu, "Effect of surfactants on the formation and characterization of a new type of colloidal drug delivery system: nanostructured lipid carriers," *Colloids and Surfaces A*, vol. 315, no. 1–3, pp. 210–216, 2008.
- [19] E. B. Souto, S. A. Wissing, C. M. Barbosa, and R. H. Müller, "Evaluation of the physical stability of SLN and NLC before and after incorporation into hydrogel formulations," *European Journal of Pharmaceutics and Biopharmaceutics*, vol. 58, no. 1, pp. 83–90, 2004.
- [20] Q. Xia, A. Saupe, R. H. Müller, and E. B. Souto, "Nanostructured lipid carriers as novel carrier for sunscreen formulations," *International Journal of Cosmetic Science*, vol. 29, no. 6, pp. 473–482, 2007.
- [21] D. Nesseem, "Formulation of sunscreens with enhancement sun protection factor response based on solid lipid nanoparticles," *International Journal of Cosmetic Science*, vol. 33, no. 1, pp. 70–79, 2011.
- [22] C. M. Ng, P. C. Chen, and S. Manickam, "Green high-gravitational synthesis of silver nanoparticles using a rotating packed bed reactor (RPBR)," *Industrial and Engineering Chemistry Research*, vol. 51, no. 15, pp. 5375–5381, 2012.
- [23] R. H. Müller, M. Radtke, and S. A. Wissing, "Nanostructured lipid matrices for improved microencapsulation of drugs," *International Journal of Pharmaceutics*, vol. 242, no. 1-2, pp. 121–128, 2002.

Research Article

Hierarchical Structures and Shaped Particles of Bioactive Glass and Its *In Vitro* Bioactivity

U. Boonyang,¹ F. Li,² and A. Stein²

¹ Molecular Technology Research Unit, School of Science, Walailak University, Nakhon Si Thammarat 80161, Thailand

² Department of Chemistry, University of Minnesota, MN 55455, USA

Correspondence should be addressed to U. Boonyang; upsorn.bo@wu.ac.th

Received 12 April 2013; Revised 3 June 2013; Accepted 22 July 2013

Academic Editor: Jie Huang

Copyright © 2013 U. Boonyang et al. This is an open access article distributed under the Creative Commons Attribution License, which permits unrestricted use, distribution, and reproduction in any medium, provided the original work is properly cited.

In this study, bioactive glass particles with controllable structure and porosity were prepared using dual-templating methods. Block copolymers used as one template component produced mesopores in the calcined samples. Polymer colloidal crystals as the other template component yielded either three-dimensionally ordered macroporous (3DOM) products or shaped bioactive glass nanoparticles. The *in vitro* bioactivity of these bioactive glasses was studied by soaking the samples in simulated body fluid (SBF) at body temperature (37°C) for varying lengths of time and monitoring the formation of bone-like apatite on the surface of the bioactive glass. A considerable bioactivity was found that all of bioactive glass samples have the ability to induce the formation of an apatite layer on its surface when in contact with SBF. The development of bone-like apatite is faster for 3DOM bioactive glasses than for nanoparticles.

1. Introduction

During the last decade, the use of mesoporous materials, which have pores ranging in size from 2 to 50 nm, was proposed in tissue engineering because their large surface area and pore volume may enhance their bioactive behavior and allow them to be loaded with the osteogenic agents used to promote new bone formation [1–4]. Mesoporous bioactive glasses (MBGs) have attracted much attention in many potential applications, such as catalysis, adsorption/separation, synthesis of nanomaterials [5–9], and, recently, also in the field of biomaterial science as bone scaffolds [10, 11], bone filler [12], and drug delivery systems [11, 13–15].

Although all of the reported MBGs show favorable bioactivity, they are difficult to use as scaffolds for the regeneration of bone tissues at this stage because their mesosized pores are too small to promote cell growth. To overcome this pore size limitation, our group successfully prepared hierarchically structured three-dimensionally ordered macroporous (3DOM) by the sol-gel method using a block-copolymer and polymer colloidal crystals as dual templates, which can generate either three-dimensionally ordered macroporous structures or shaped bioactive glass nanoparticles.

2. Experimental

2.1. General. Calcium nitrate tetrahydrate ($\text{Ca}(\text{NO}_3)_2 \cdot 4\text{H}_2\text{O}$), tetraethyl orthosilicate (TEOS), triethyl phosphate (TEP), the surfactant Brij 56 ($\text{C}_{16}\text{H}_{33}(\text{OCH}_2\text{CH}_2)_n\text{OH}$, $n \sim 10$), and polymethylmethacrylate (PMMA) colloidal crystals with 400 nm size were prepared by a published method [17].

2.2. Preparation of Bioactive Glasses. MBGs were synthesized by a sol-gel method. In a typical synthesis of bioactive glass nanoparticles M58S (M58SP), Brij 56 was used as a structure-directing agent for the mesostructure [18] and tetraethyl orthosilicate (TEOS), triethyl phosphate (TEP), and $\text{Ca}(\text{NO}_3)_2 \cdot 4\text{H}_2\text{O}$ were the sources of Si, P, and Ca, respectively (Si/Ca/P = 60:36:4, molar ratio). Amounts of 0.850 g of $\text{Ca}(\text{NO}_3)_2 \cdot 4\text{H}_2\text{O}$ and 0.096 g of citric acid were dissolved in 2 mL of 1M HNO_3 , and 0.073 g of TEP was added into the solution while stirring at room temperature. A solution containing 1.250 g of TEOS and 0.340 g of Brij 56 was then added to this mixture. The combined mixture was stirred at room temperature for 30 min or until the solution became clear. A monolithic piece of the PMMA colloidal

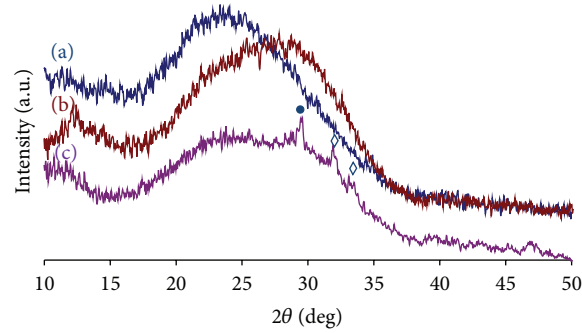


FIGURE 1: Wide angle XRD patterns of (a) M80S, (b) M70S, and (c) M58S (symbol ● calcium phosphate and ◇ calcium phosphate silicate).

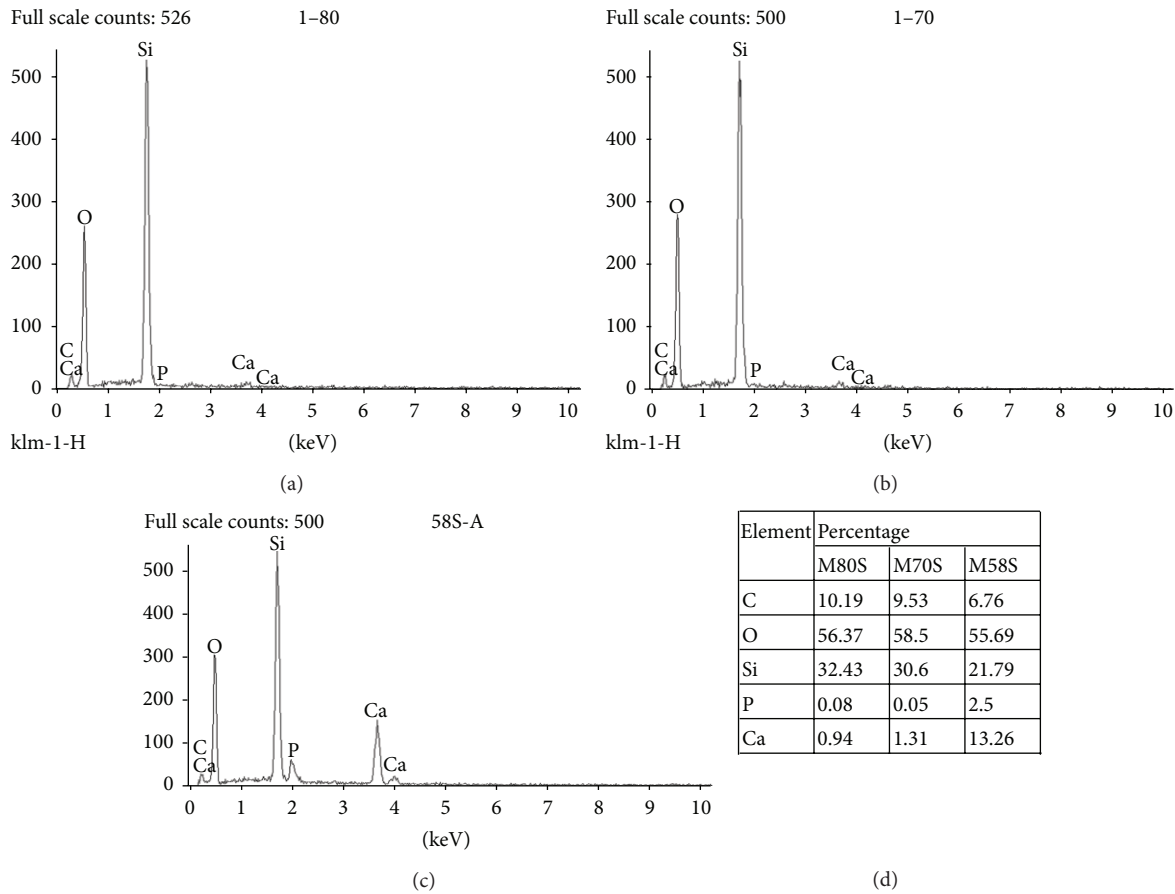


FIGURE 2: EDS spectrum and the element ratio of (a) M80S, (b) M70S, and (c) M58S and (d) the percentage of element of MBGs.

crystal template was immersed into this clear solution. After complete infiltration, the samples were aged at 45°C for 48 h and dried at 45°C for 24 h in air. The as-synthesized samples were calcined at 600°C in air for 6 h in order to remove the template completely. The heating rate for the calcination was fixed at 2°C/min. In the case of M80S, M70S, and M58S, bioactive glass materials were synthesized by the same method, without ageing at 45°C. The nominal compositions of the MBGs under study are listed in Table 1. The structure of the bioactive glasses was analyzed in detail

by X-ray diffraction (XRD), energy dispersive spectroscopy (EDS), scanning electron microscopy (SEM), transmission electron microscopy (TEM), and Fourier transform infrared spectroscopy (FTIR).

2.3. Study of Bioactivity. The *in vitro* bioactivity study was performed by soaking the MBGs in simulated body fluid (SBF) prepared by the method of Kokubo et al. [19] at 37°C for 3, 6, 12, 24, and 48 h, and the surface of the samples was characterized by FTIR, SEM, and XRD.

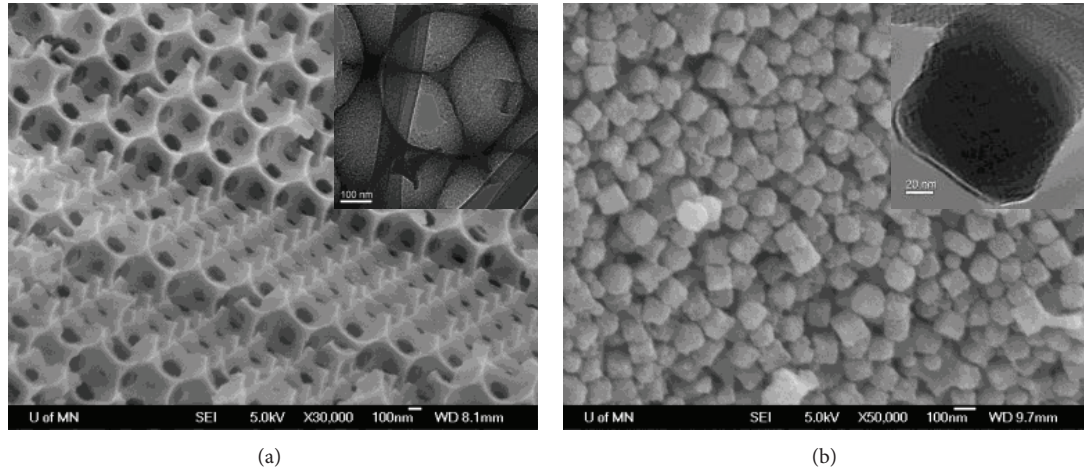


FIGURE 3: SEM and TEM images of (a) M58S and (b) M58SP.

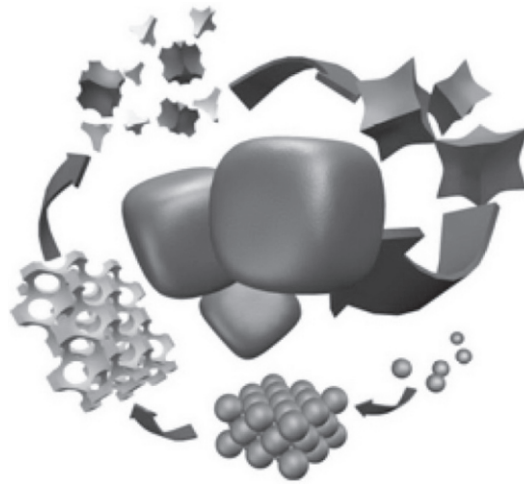


FIGURE 4: Schematic of the formation of nanoparticles through the disassembly of 3DOM structure. Copyright 2007, Wiley-VCH [16].

TABLE 1: Chemical compositions of MBGs (mol%).

Samples	SiO ₂	CaO	P ₂ O ₅
M80S	80	20	—
M70S	70	30	—
M58S, M58SP	60	36	4

3. Results and Discussion

3.1. Sample Characterization. Figure 1 shows the XRD patterns of MBGs after calcination at 600°C with a ramp rate 2°C/min in air. All samples show a broad peak in the 2θ range 15–35°, which suggests that all MBGs with different chemical compositions exist as amorphous phases. The pattern of the M58S sample contained additional reflections assigned to calcium phosphate silicate and calcium phosphate (JCPDS-00-050-0905 and 00-044-0752). The EDS spectra of all MBGs showed peaks of carbon, oxygen, silicon, phosphate, and calcium with relative amounts indicated in Figure 2.

Figure 3 shows the representative SEM images of (a) M58S and (b) M58S. Bioactive glass with hierarchical porosity was first formed through the PMMA and Brij 56 dual-templating system. Without of aging step at 45°C, no structure transformation occurred and the 3DOM structure was produced (Figure 3(a)) due to no shrinkage process between the ageing step [16, 20]. After a sufficient time of aging (at least 48 h), no 3DOM structure remained and, nanocube with ~100 nm edge lengths were obtained (Figure 3(b)). Typically, an fcc array of spheres, octahedral (O_h), and tetrahedral (T_d) voids exist between the spheres. The bioactive glass precursor infiltrated these voids and formed an inverse replica of the template. So correspondingly, the 3DOM structure can be considered to be built up from these two basic units (O_h and T_d) which are interconnected through narrow necks. The disassembly occurs first by shrinkage in a polycondensation reaction during aging process until the silanol groups are no longer close enough to react with each other [16, 20]. Follow with the syneresis is defined as “spontaneous shrinkage of the gel and the resulting expulsion of liquid from the pores” [20].

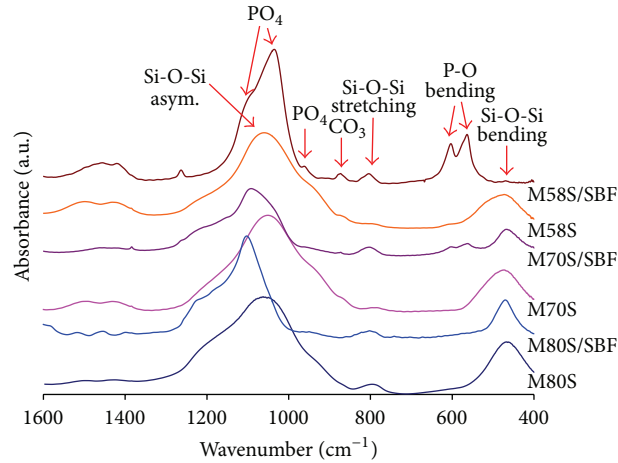


FIGURE 5: FTIR spectra of MBGs with different chemical compositions before and after soaking in SBF for 12 h.

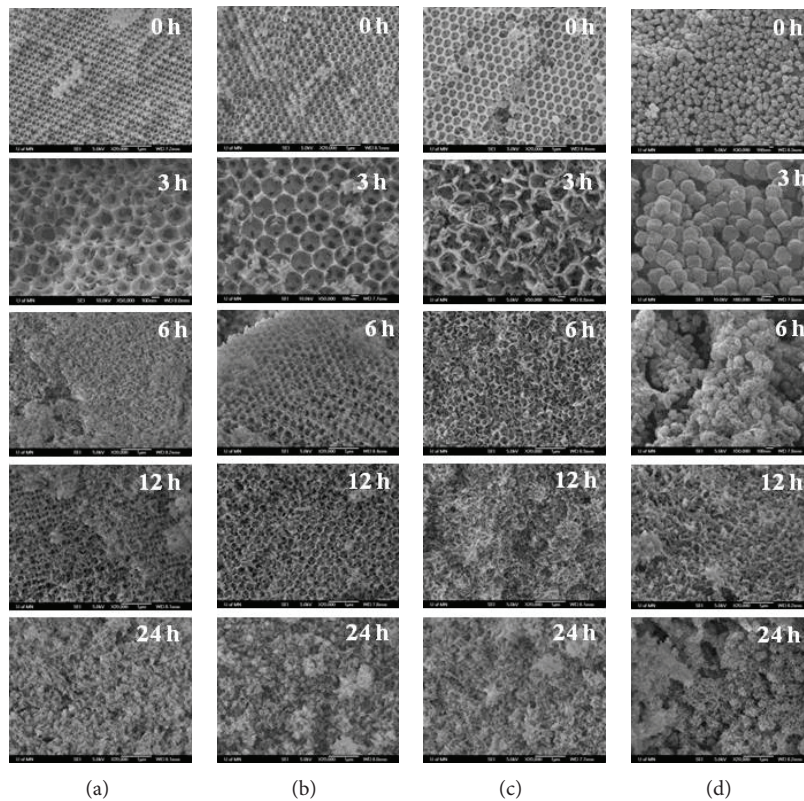


FIGURE 6: SEM images of (a) M80S, (b) M70S, (c) M58S, and (d) M58SP after soaking in SBF for different times (0, 3, 6, 12, and 24 h).

By complete disconnection of the skeleton at the narrowest connection points. Hence, the nanocubes produced from the octahedral holes. This formation mechanism is known as disassembly and occurs in order to stabilize the structure of the 3DOM material (Figure 4) [16].

3.2. Study of Bioactivity. Figure 5 shows the FTIR spectra of MBGs with different chemical compositions before and after soaking in SBF for 12 h. The FTIR spectra of series

M80S, M70S, and M58S before soaking in SBF, all spectra show the characteristic absorption bands of the Si-O-Si asymmetric stretching and symmetric bending mode at 1060 cm^{-1} , 800 cm^{-1} , and 478 cm^{-1} , respectively, [21, 22]. The shoulder around 950 cm^{-1} is related to the Si-O-Ca vibration mode [21]. Spectra of M70S, M58S, and M58SP, after samples were soaked in SBF for 12 h, a doublet at 568 cm^{-1} and 607 cm^{-1} is shown, which is associated with the P-O bending vibration and at 1040 cm^{-1} and 1090 cm^{-1} can be attributed to the stretching PO_4 vibration [21, 23].

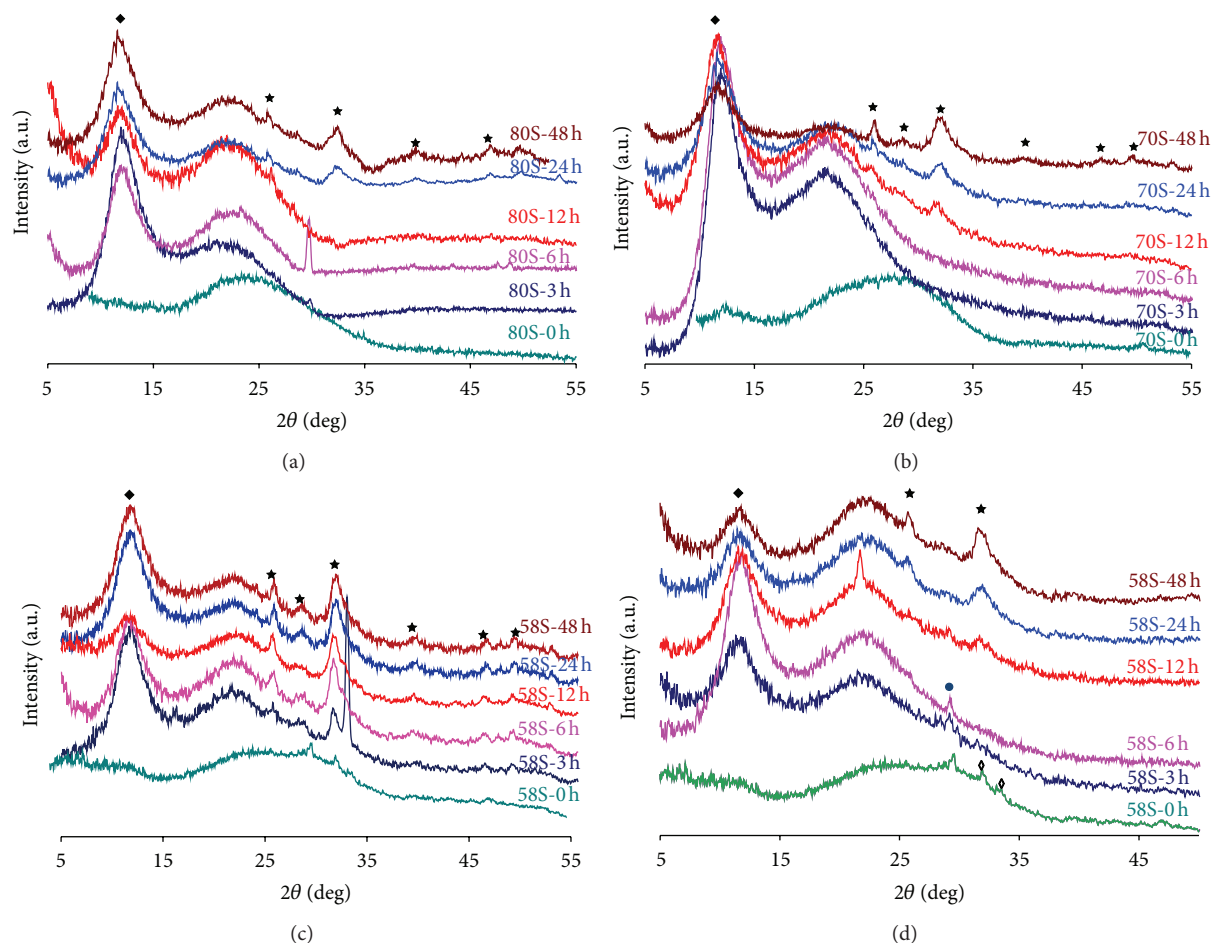


FIGURE 7: Wide angle XRD patterns of (a) M80S, (b) M70S, (c) M58S, and (d) 58SP before and after soaking in SBF with different times (symbol \blacklozenge brushite, \diamond calcium phosphate silicate, \bullet calcium phosphate, and black star hydroxyapatite).

Additionally, SEM micrographs of the sample surfaces before and after soaking in SBF for different times are shown in Figure 6. For M80S, M70S, and M58SP after 6 h of soaking, small needle-like crystal agglomerates were observed on the surface. In contrast, the surfaces of the M58S samples were needle-like after soaking in SBF within 3 h. All samples were completely covered by a needle-like crystal layer in 24 h. XRD patterns (Figure 7) confirmed that the needle-like crystal can be assigned to the bone-like apatite phase. Furthermore, the *in vitro* bioactivity of MBGs is dependent on the Si/Ca ratio in the network which, as a result of the higher calcium content exhibits the best *in vitro* bioactivity [2]. It is clear that M58S shows faster bioactivity than M70S and M80S, and the 3DOM structure of M58S shows higher bioactivity than M58SP.

4. Conclusion

The bioactive glass skeleton with hierarchical porosity was first formed via a surfactant and polymer sphere dual-templating system, and then the three-dimensionally ordered structure was disassembled to obtain bioactive nanocubes. In addition, the study of *in vitro* bioactivity found that all

of bioactive glass samples have the ability to induce the formation of a bone-like apatite layer on its surface when in contact with SBF within 6 h and the transformation to bone-like apatite was more efficient for M58S than for M80S and M70S. Furthermore, the 3DOM structure of M58S shows higher bioactivity than M58SP.

Acknowledgments

The authors would like to thank Walailak University Research and Development Institute, Walailak University, (Grant no. WU54203) and the National Science Foundation (DMR-0704312).

References

- [1] M. Vallet-Regí, L. Ruiz-González, I. Izquierdo-Barba, and J. M. González-Calbet, "Revisiting silica based ordered mesoporous materials: medical applications," *Journal of Materials Chemistry*, vol. 16, no. 1, pp. 26–31, 2006.
- [2] X. Yan, X. Huang, C. Yu et al., "The *in vitro* bioactivity of mesoporous bioactive glasses," *Biomaterials*, vol. 27, no. 18, pp. 3396–3403, 2006.

- [3] A. López-Noriega, D. Arcos, I. Izquierdo-Barba, Y. Sakamoto, O. Terasaki, and M. Vallet-Regí, "Ordered mesoporous bioactive glasses for bone tissue regeneration," *Chemistry of Materials*, vol. 18, no. 13, pp. 3137–3144, 2006.
- [4] X. Li, X. Wang, H. Chen, P. Jiang, X. Dong, and J. Shi, "Hierarchically porous bioactive glass scaffolds synthesized with a PUF and P123 coterminated approach," *Chemistry of Materials*, vol. 19, no. 17, pp. 4322–4326, 2007.
- [5] M. E. Davis, "Ordered porous materials for emerging applications," *Nature*, vol. 417, no. 6891, pp. 813–821, 2002.
- [6] C. W. Lee, D. H. Ahn, B. Wang, J. S. Hwang, and S. Park, "Hydroxylation of phenol over surface functionalized MCM-41 supported metal catalyst," *Microporous and Mesoporous Materials*, vol. 44–45, pp. 587–594, 2001.
- [7] W. H. Zhang, J. Lu, B. Han et al., "Direct synthesis and characterization of titanium-substituted mesoporous molecular sieve SBA-15," *Chemistry of Materials*, vol. 14, no. 8, pp. 3413–3421, 2002.
- [8] C. Yang, H. Sheu, and K. Chao, "Templated synthesis and structural study of densely packed metal nanostructures in MCM-41 and MCM-48," *Advanced Functional Materials*, vol. 12, no. 2, pp. 143–148, 2002.
- [9] L. Li, J. Shi, J. Yan, X. Zhao, and H. Chen, "Mesoporous SBA-15 material functionalized with ferrocene group and its use as heterogeneous catalyst for benzene hydroxylation," *Applied Catalysis A*, vol. 263, no. 2, pp. 213–217, 2004.
- [10] J. R. Jones and L. L. Hench, "Effect of surfactant concentration and composition on the structure and properties of sol-gel-derived bioactive glass foam scaffolds for tissue engineering," *Journal of Materials Science*, vol. 38, no. 18, pp. 3783–3790, 2003.
- [11] M. Vallet-Regí, "Ordered mesoporous materials in the context of drug delivery systems and bone tissue engineering," *Chemistry*, vol. 12, no. 23, pp. 5934–5943, 2006.
- [12] E. Pirhonen, L. Moimas, and J. Haapanen, "Porous bioactive 3-D glass fiber scaffolds for tissue engineering applications manufactured by sintering technique," *Key Engineering Materials*, vol. 240–242, pp. 237–240, 2003.
- [13] W. Xia and J. Chang, "Well-ordered mesoporous bioactive glasses (MBG): a promising bioactive drug delivery system," *Journal of Controlled Release*, vol. 110, no. 3, pp. 522–530, 2006.
- [14] M. Vallet-Regí, A. Rámila, R. P. Del Real, and J. Pérez-Pariente, "A new property of MCM-41: drug delivery system," *Chemistry of Materials*, vol. 13, no. 2, pp. 308–311, 2001.
- [15] W. Xia and J. Chang, "Preparation, *in vitro* bioactivity and drug release property of well-ordered mesoporous 58S bioactive glass," *Journal of Non-Crystalline Solids*, vol. 354, no. 12–13, pp. 1338–1341, 2008.
- [16] F. Li, Z. Wang, and A. Stein, "Shaping mesoporous silica nanoparticles by disassembly of hierarchically porous structures," *Angewandte Chemie*, vol. 46, no. 11, pp. 1885–1888, 2007.
- [17] H. Yan, C. F. Blanford, W. H. Smyrl, and A. Stein, "Preparation and structure of 3D ordered macroporous alloys by PMMA colloidal crystal templating," *Chemical Communications*, no. 16, pp. 1477–1478, 2000.
- [18] G. S. Attard, J. C. Glyde, and C. G. Göltner, "Liquid-crystalline phases as templates for the synthesis of mesoporous silica," *Nature*, vol. 378, no. 6555, pp. 366–368, 1995.
- [19] T. Kokubo, H. Kushitani, S. Sakka, T. Kitsugi, and T. Yamamuro, "Solutions able to reproduce *in vivo* surface-structure changes in bioactive glass-ceramic A-W3," *Journal of Biomedical Materials Research*, vol. 24, no. 6, pp. 721–734, 1990.
- [20] L. L. Hench and J. K. West, "The Sol-Gel process," *Chemical Reviews*, vol. 90, no. 1, pp. 33–72, 1990.
- [21] S. Padilla, J. Román, A. Carenas, and M. Vallet-Regí, "The influence of the phosphorus content on the bioactivity of sol-gel glass ceramics," *Biomaterials*, vol. 26, no. 5, pp. 475–483, 2005.
- [22] J. Serra, P. González, S. Liste et al., "FTIR and XPS studies of bioactive silica based glasses," *Journal of Non-Crystalline Solids*, vol. 332, no. 1–3, pp. 20–27, 2003.
- [23] Y. Zhu, C. Wu, Y. Ramaswamy et al., "Preparation, characterization and *in vitro* bioactivity of mesoporous bioactive glasses (MBGs) scaffolds for bone tissue engineering," *Microporous and Mesoporous Materials*, vol. 112, no. 1–3, pp. 494–503, 2008.

Research Article

β -Tricalcium Phosphate Micron Particles Enhance Calcification of Human Mesenchymal Stem Cells *In Vitro*

Yusuke Nakagawa,¹ Takeshi Muneta,¹ Kunikazu Tsuji,² Shizuko Ichinose,³
Yasuharu Hakamatsuka,⁴ Hideyuki Koga,¹ and Ichiro Sekiya⁵

¹ Department of Joint Surgery and Sports Medicine, Graduate School, Tokyo Medical and Dental University, 1-5-45 Yushima, Bunkyo-ku, Tokyo 113-8519, Japan

² Department of Cartilage Regeneration, Graduate School, Tokyo Medical and Dental University, 1-5-45 Yushima, Bunkyo-ku, Tokyo 113-8519, Japan

³ Research Center for Medical and Dental Sciences, Tokyo Medical and Dental University, 1-5-45 Yushima, Bunkyo-ku, Tokyo 113-8519, Japan

⁴ Medical Strategy Planning Department, Medical Technology R&D Division, Corporate R&D Center, Olympus Corporation, 2-3 Kuboyama-chou, Hachioji-shi, Tokyo 192-8512, Japan

⁵ Department of Applied Regenerative Medicine, Graduate School, Tokyo Medical and Dental University, 1-5-45 Yushima, Bunkyo-ku, Tokyo 113-8519, Japan

Correspondence should be addressed to Ichiro Sekiya; sekiya.orj@tmd.ac.jp

Received 5 April 2013; Accepted 13 June 2013

Academic Editor: Mamoru Aizawa

Copyright © 2013 Yusuke Nakagawa et al. This is an open access article distributed under the Creative Commons Attribution License, which permits unrestricted use, distribution, and reproduction in any medium, provided the original work is properly cited.

β -Tricalcium phosphate (β -TCP) micron particles whose diameters range from 1 μm to 10 μm have been recently developed, however, their biological effects remain unknown. We investigated the biological effects of β -TCP micron particles on proliferation, cytotoxicity, and calcification of human synovial mesenchymal stem cells (MSCs). MSCs were cultured without dexamethasone, β -glycerophosphate, or ascorbic acid. 1.0 mg/mL β -TCP micron particles inhibited proliferation of MSCs significantly and increased dead cells. In the contact condition, 0.1 mg/mL β -TCP micron particles promoted calcification of MSCs evaluated by alizarin red staining and enhanced mRNA expressions of runx2, osteopontin, and type I collagen. In the noncontact condition, these effects were not observed. 0.1 mg/mL β -TCP micron particles increased calcium concentration in the medium in the contact condition, while 1.0 mg/mL β -TCP micron particles decreased calcium and phosphorus concentrations in the medium in the noncontact condition. By transmission electron microscopy, β -TCP micron particles were localized in the phagosome of MSCs and were dissolved. In conclusion, β -TCP micron particles promoted calcification of MSCs and enhanced osteogenesis-related gene expressions *in vitro*.

1. Introduction

β -Tricalcium phosphate (β -TCP) blocks with suitable porous structure are an osteoconductive bone graft substitute [1–4]. β -TCP micron particles whose diameters range from 1 μm to 10 μm have been recently developed and have attracted attention because these particles are smaller than cells, and their biological effects seem to be different from those of larger particles [5]. However, the precise interaction between β -TCP micron particles and cells remains unknown.

Mesenchymal stem cells (MSCs) play important physiological roles in maintaining homeostasis and repairing damaged tissues including bone [6, 7]. When a bone is fractured, MSCs are mobilized to the site differentiate into osteoblasts, then the bone tissues heal completely [8, 9]. Modifications of MSCs have a possibility to improve the function of MSCs for bone formation [10, 11].

In this study, we investigated the biological effect of β -TCP micron particles on proliferation, toxicity, and calcification of MSCs when these particles were treated with MSCs.

We also performed morphological analysis on MSCs treated with β -TCP micron particles. Our results revealed for the first time the *in vitro* effect of β -TCP micron particles on MSCs.

2. Experimental Procedures

2.1. Preparation of β -TCP Micron Particles. To produce the micron particles, porous-type β -TCP block (Osferion, Olympus Terumo Biomaterials Corp, Tokyo, Japan), whose porosity was 75%, was crushed into granules by an alumina rod. The granules were filtered by stainless sieves for sorting into sizes less than 500 μm in diameter, and they were further filtered by air classifiers. The range of the particle sizes was measured by laser diffraction method using a laser particle sizer (Microtrac HRA, Nikkiso, Japan). The particles were dispersed in an ultrasonic bath for 1 minute. Triton X-100 and distilled water were used as dispersing agents. Morphological characteristics and chemical elements of the particles were observed and analyzed by scanning electron microscopy (S-4500, Hitachi, Hitachinaka, Japan), and energy-dispersive X-ray spectroscopy (EMAX-7000, Horiba Ltd., Kyoto, Japan). The crystal structure of the particles was examined by X-ray diffraction instrument (MiniFlex, Rigaku, Tokyo, Japan) using $\text{CuK}\beta$ radiation. The data were collected from 10° to 60° with a step size of 0.02° .

2.2. Isolation and Culture of Human Synovial MSCs. The study was approved by an institutional review board, and informed consents were obtained from all donors. Human synovium was harvested during knee operations. The synovium was minced into small pieces, digested with 3 mg/mL Collagenase D (Roche Diagnostics, Mannheim, Germany) for 3 hours, and cultured at a clonal density in complete culture medium (CCM: α MEM) (Invitrogen, Carlsbad, CA) containing 10% fetal bovine serum, 100 units/mL penicillin, 100 mg/mL streptomycin, and 250 ng/mL amphotericin B (Invitrogen) for 14 days. Passage 2 MSCs were mainly used for the following analyses. Three days after replating, CCM was replaced with CCM supplemented with β -TCP micron particles. Then, the medium was changed with CCM without any β -TCP micron particles two times per week.

2.3. Colony-Forming Assays. One thousand cells at passage 2 were plated and cultured for 14 days in 60 cm^2 dishes. The cells were subsequently fixed with 4% paraformaldehyde, stained with 0.5% crystal violet (Wako, Osaka, Japan) for 5 minutes.

2.4. In Vitro Differentiation Assay. For chondrogenesis, 250,000 cells were placed in a 15 mL polypropylene tube (BD Falcon, Bedford, MA) and pelleted by centrifugation at $450 \times g$ for 10 minutes. The pellets were cultured for 21 days in chondrogenic medium, which contained 1000 ng/mL bone morphogenetic protein 7 (BMP-7) (Stryker Biotech, Boston, MA), 10 ng/mL transforming growth factor- β 3 (TGF- β 3) (R&D Systems Inc., Minneapolis, MN), and 10^{-7} M dexamethasone (Sigma-Aldrich, St. Louis, MO). For histological analysis, the pellets were embedded in paraffin, cut into 5 μm

sections, and stained with 1% toluidine blue [12]. The sections were immunostained for type II collagen using a primary anti-rat monoclonal antibody against human type II collagen (1:200 dilution with PBS containing 1% BSA; Daiichi Fine Chemical, Toyama, Japan) as described previously [13].

For adipogenesis, the cells were cultured in the adipogenic medium that consisted of a CCM supplemented with 0.5 μM dexamethasone (Sigma-Aldrich), 0.5 mM isobutylmethylxanthine (Sigma-Aldrich), and 50 μM indomethacin (Wako). After 21 days, the adipogenic cultures were stained with 0.3% oil red-o solution.

For calcification, the cells were cultured in the calcification medium in the presence of 100 nM dexamethasone, 10 mM β -glycerophosphate, and 50 μM ascorbic acid. After 3 weeks, the dishes were washed with PBS twice and fixed in 10% formalin for 5 minutes and stained with 2% alizarin red solution (pH 4.1; Sigma-Aldrich) for 2 minutes. The staining was used to detect calcium deposition in the extracellular matrix. For alkaline phosphatase (ALP) activity, MSCs were plated at 5000 cells/ cm^2 in 6-well culture dishes and incubated in CCM and calcification medium. ALP activity was measured after 21 days of differentiation. The cells were harvested with lysis buffer (0.1 M Tris-HCl, 5 mM MgCl_2 , 2% Triton X-100, and 1 mM phenylmethylsulfonyl fluoride) and sonicated. Total protein concentrations of the supernatant were determined by the Bradford method (Bio-Rad, Hercules, CA). An aliquot (10 μL) of supernatant was added to 100 μL 50 mM p-nitrophenylphosphatase hexahydrate containing 1 mM MgCl_2 , and the mixture was incubated at 37°C for 30 minutes. Absorption at 405 nm was measured with a spectrophotometer. The ALP activity per total protein represented millimoles of p-nitrophenol release after 30 minutes of incubation at 37°C .

2.5. Epitope Profile. Synovial MSCs at passage 2 were harvested 7 days after plating. One hundred thousand cells were suspended in 1000 μL FACS buffer (0.2% BSA and 0.09% sodium azide with PBS) containing 400 ng/mL phycoerythrin- (PE-) coupled antibodies against CD34 and CD90 (BD Bioscience, CA), APC-H7 coupled antibodies against CD44 (BD), PE-Cy7 coupled antibodies against CD45 (BD), and PerCP-Cy 5.5 against CD73 and CD105 (BD). As an isotype control, APC-H7, PE-Cy7, PerCP-Cy5.5, or PE-coupled nonspecific mouse IgG (BD) was substituted for the primary antibody. After incubation for one hour at 4°C , the cells were washed with PBS and resuspended in 1 mL FACS buffer for analysis. Cell fluorescence was evaluated by flow cytometry in a FACSVerser instrument (BD); data were analyzed by using FACSite software (BD).

2.6. Cell Proliferation. The proliferation of cells was evaluated by an MTT (3-(4,5-dimethylthiazol-2yl)-2,5-disphenyl-2H-tetrazolium-bromide) assay kit (Roche Diagnostics). MSCs were plated at 5000 cells/ cm^2 in 96-well plates (Nalgen Nunc International, NY) with CCM supplemented with β -TCP micron particles at a concentration of 0, 0.01, 0.1, and 1.0 mg/mL. A 10 μL MTT solution was added into each well and incubated at 37°C in a 5% CO_2 humidified incubator.

After 4 hours, 100 μL dimethylsulfoxide was added to dissolve purple crystals. The next day, absorbance was determined at 560 nm by a microplate spectrophotometer (LS-PLATE Manager 2004, Wako).

2.7. Cell Viability. In the contact condition, MSCs were plated at 5000 cells/cm² in 6-well plates (BD) with CCM supplemented with β -TCP micron particles at a concentration of 0, 0.01, 0.1, and 1.0 mg/mL. In the noncontact condition, transwell inserts (Corning Incorporated Life Sciences, MA) consisting of 0.4 μm pores were used, and CCM supplemented with β -TCP micron particles was added in the inserts so that the MSCs and β -TCP micron particles became separated in the same culture medium. Two days after incubation, a working solution containing 2 μM Calcein AM and 4 μM ethidium homodimer-1 (EthD-1) (Live/Dead Viability/Cytotoxicity Kit for mammalian cells, Invitrogen) was added to each well. After incubation for 20 minutes at 37°C with 5% humidified CO₂, the labeled MSCs were observed by confocal microscopy (Olympus IX71, Olympus Corporation, Tokyo, Japan). Calcein AM-positive cells which refer to living cells and EthD-1-positive cells which refer to dead cells were counted in five high-power fields (at 200 times magnification), whose area was 500 \times 700 μm .

2.8. Calcification. MSCs were plated at 5000 cells/cm² in 12-well plates with CCM supplemented with β -TCP micron particles at a concentration of 0, 0.01, and 0.1 mg/mL in both the contact and the noncontact condition. MSCs were also plated at 5000 cells/cm² in 12-well plates with CCM and calcification medium. Twenty-one days after incubation, cell cultures were stained with 2% alizarin red solution (pH 4.1; Sigma-Aldrich) for 2 minutes. Incubation with calcification medium was performed as a positive control. Pictures of these plates stained by alizarin red were taken by stereoscopic microscope (Olympus MVX10, Olympus Corporation) and light microscopy (Olympus IX71). The area of alizarin red positive staining was measured by Image J software (National Institutes of Health, Bethesda, MD). In the contact condition, the area of alizarin red positive staining was calculated by subtracting the area of alizarin red positive staining at 3 days from those of at 21 days in order to exclude staining of the β -TCP micron particles themselves.

2.9. Real-Time PCR Analysis. MSCs were plated at 5000 cells/cm² in 12-well plates (BD) with CCM supplemented with β -TCP micron particles at a concentration of 0, 0.01, and 0.1 mg/mL in both contact and noncontact condition. MSCs were plated at 5000 cells/cm² in 12-well plates with CCM and calcification medium. Twenty-one days after incubation, total RNA was isolated from cells with the RNeasy Total RNA Mini Kit (Qiagen, CA). cDNA was synthesized with oligo-dT primers from total RNA using the Transcriptor High Fidelity cDNA Synthesis Kit (Roche Diagnostics) according to the manufacturer's protocol. Reverse transcription (RT) was performed by 30 minutes of incubation at 55°C, followed by 5 minutes of incubation at 85°C. Real-time PCR was performed in a LightCycler 480 instrument

(Roche Diagnostics) using FastStart TaqMan Probe Master and TaqMan probes for runx2 (no. 87), osteopontin (no. 61), type I collagen (no. 60), osteocalcin (no. 81), and β -Actin (no. 11) (Roche Diagnostics). After an initial denaturation step (95°C for 10 minutes), amplification was performed for 45 cycles (95°C for 15 seconds, 60°C for 60 seconds). Relative amounts of mRNA were calculated as previously described [14].

The primers were as follows:

runx2 (forward): 5'-gtgcctaggcgcatttca-3'
 runx2 (backward): 3'-cacctgcctggctcttcta-5'
 osteopontin (forward): 5'-cgcagacctgacatccagt-3'
 osteopontin (backward): 3'-ggctgtcccaatcagaagg-5'
 type I collagen (forward): 5'-aggtcccctggaagaa-3'
 type I collagen (backward): 3'-aatctcgagcacctga-5'
 osteocalcin (forward): 5'-tgtgaaggcgtctcaaacag-3'
 osteocalcin (backward): 3'-ctcacacacctcctctg-5'
 β -actin (forward): 5'-attggcaatgagcggttc-3'
 β -actin (backward): 3'-tgaaggtagttctggtatgc-5'

2.10. Measurement of Calcium and Phosphorus Concentrations. MSCs were plated at 5000 cells/cm² in 12-well plates with CCM supplemented with β -TCP micron particles at a concentration of 0, 0.01, 0.1, and 1.0 mg/mL in both contact and noncontact condition. Culture medium was taken at 2, 7, 14, and 21 days, centrifuged to remove the particles, and the supernatant was measured for calcium and phosphorus concentration by using an automatically analytical instrument of LABOSPECT008K (Hitachi High-Technologies, Tokyo, Japan). For measurement of calcium concentration, a Clinimate CA test kit (Sekisui Medical, Tokyo, Japan) was used, and for phosphorus concentration, a Clinimate IP-2 (Sekisui Medical) was used.

2.11. Light Microscopy. MSCs were plated at 5000 cells/cm² in 6-well plates (BD Bioscience, CA) with CCM supplemented with β -TCP micron particles at a concentration of 0.1 mg/mL. During the culture period, the cell morphologies and β -TCP micron particles were observed by light microscopy (Olympus IX71).

2.12. Transmission Electron Microscopy. Ultrathin sections at 90 nm were collected on copper grids, double-stained with uranyl acetate and lead citrate, and then examined by transmission electron microscopy (H-7100, Hitachi). The specimens 7 days after incubation with CCM supplemented with β -TCP micron particles at a concentration of 0.1 mg/mL were analyzed.

2.13. Statistical Analysis. The StatView 5.0 program (SAS Institute, Cary, NC) was used for statistical analyses, and *P* values less than 0.05 were considered to be statistically significant. Comparisons between two groups were analyzed using the Paired *t*-test. Comparisons between multigroups

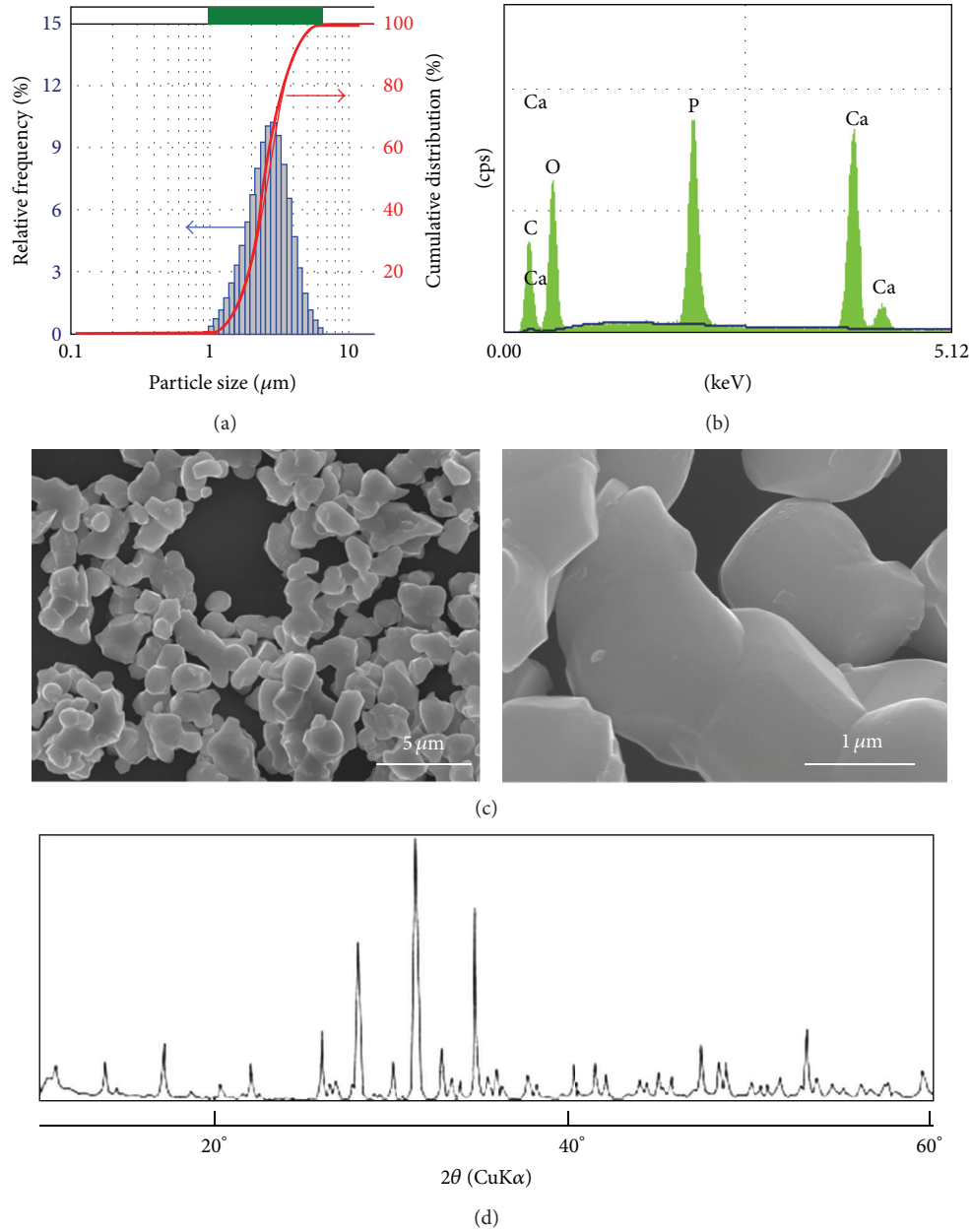


FIGURE 1: Structural properties of β -TCP micron particles. (a) Distribution of particle size (bar) and cumulative particle size (red line) by laser diffraction method. (b) Energy dispersive X-ray analysis. (c) Images of scanning electron microscopy. (d) X-ray diffraction analysis.

were analyzed using the Kruskal-Wallis test and the Scheffe test.

3. Results

3.1. Structural Properties of β -TCP Micron Particles. Particle sizes of β -TCP micron particles ranged from 1.06 μm to 6.54 μm in diameter, and the most frequent size was 3.00 μm with a percentage of 10% (Figure 1(a)). Fifty percent of the particles were smaller than 2.67 μm , which indicates $D_{50} = 2.67 \mu\text{m}$. Standard deviation (SD) was 0.93 μm , and D_{50}/SD was 0.35. EDX analysis confirmed that phosphorus

and calcium were present in the particles (Figure 1(b)). Scanning electron microscope showed connected particles which had smooth surfaces and whose diameter per unit was approximately 1 μm (Figure 1(c)). X-ray diffraction analysis of β -TCP micron particles showed that diffraction peaks matched with those of the standard β -TCP (JCPDS09-169) (Figure 1(d)).

3.2. Characteristics of Synovial Cells as MSCs. Cells derived from human synovium formed colonies (Figure 2(a)). These cells differentiated into chondrocytes (Figure 2(b)), adipocytes (Figure 2(c)) and were calcified (Figure 2(d)).

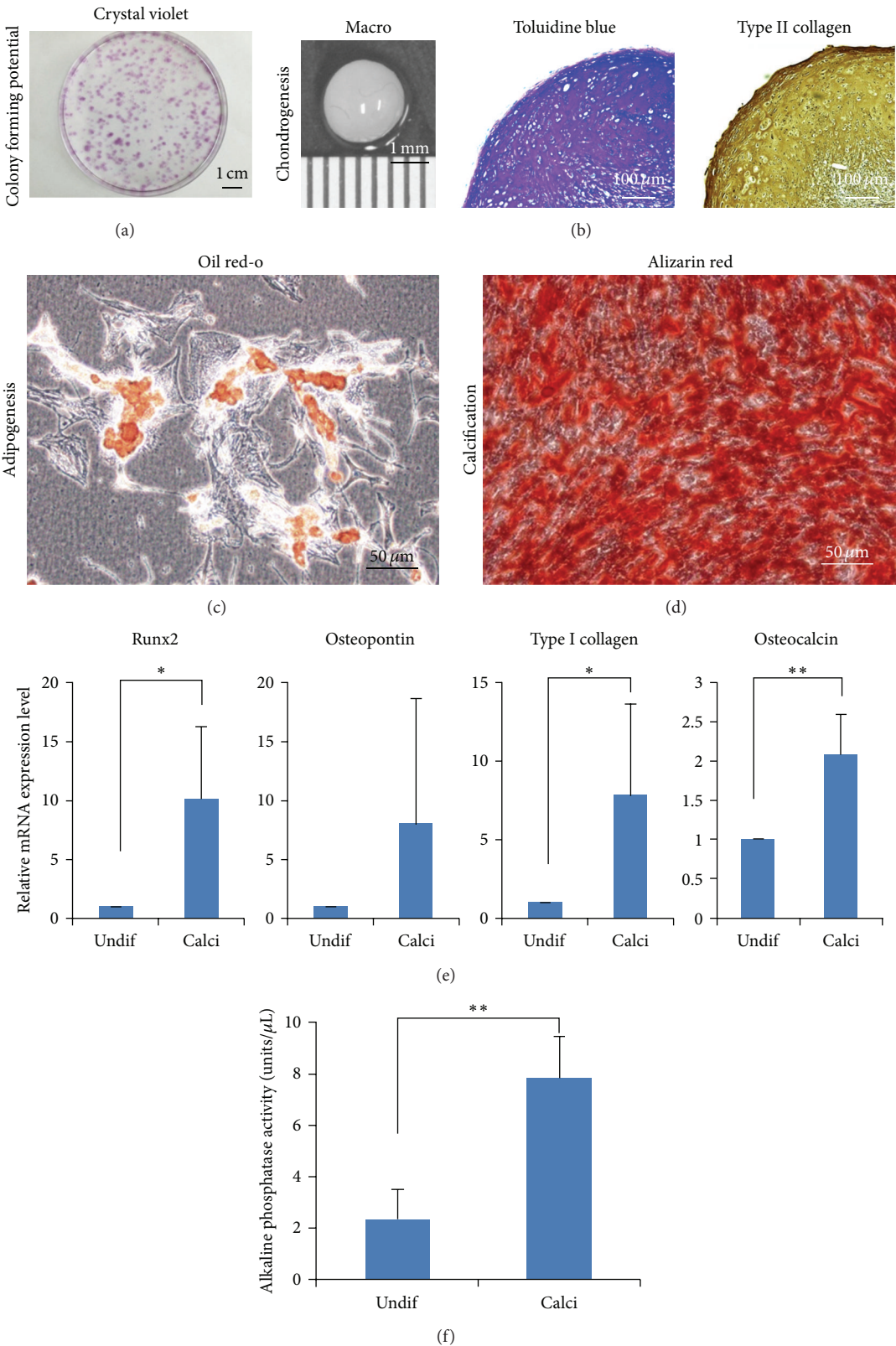


FIGURE 2: Continued.

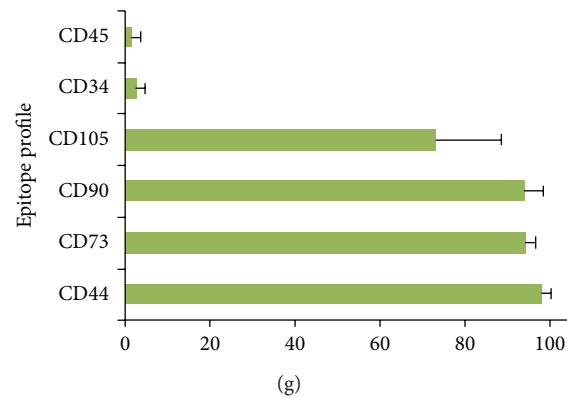


FIGURE 2: Characteristics of synovial MSCs. (a) Colony forming potential. (b) Chondrogenesis. (c) Adipogenesis. (d) Calcification. (e) Osteogenesis-related gene expressions by real-time PCR analysis. Averaged relative mRNA expression level with standard deviation is shown ($n = 6$, $*P < 0.05$, $**P < 0.01$ by the paired t -test). Synovial MSCs cultured in calcification medium were compared with undifferentiated MSCs. (f) Averaged alkaline phosphatase activity with standard deviation ($n = 7$, $**P < 0.01$ by the paired t -test). (g) Epitope profile of synovial MSCs. Positive expression rates (%) with standard deviation are shown ($n = 4$).

Expressions of osteogenesis-related genes, *runx2*, type I collagen, osteocalcin, and activity of alkaline phosphatase increased significantly when cultured in calcification medium (Figures 2(e) and 2(f)). Flow cytometric analysis demonstrated that the cells expressed CD44, CD73, CD90, and CD105 at a high level and CD34 and CD45 at a low level (Figure 2(g)). These results indicate that the cells derived from human synovium had characteristics of MSCs [15] and a potential for osteogenesis.

3.3. β -TCP Micron Particles Inhibit Proliferation of MSCs. MSCs were cultured with β -TCP micron particles in the contact or noncontact condition (Figure 3(a)). β -TCP micron particles at 1.0 mg/mL significantly inhibited proliferation of MSCs at 2, 7, and 14 days (Figure 3(b)). 1.0 mg/mL β -TCP micron particles increased the ratio of dead cells at 2 days in the contact condition (Figures 3(c) and 3(d)). A similar result was obtained in the noncontact condition (Figures 3(c) and 3(d)).

3.4. β -TCP Micron Particles Promote Calcification of MSCs. In the noncontact culture condition, β -TCP micron particles did not affect stainability with alizarin red (Figure 4(a)). In the contact condition, 0.1 mg/mL β -TCP micron particles already increased stainability with alizarin red at 3 days, and β -TCP micron particles stained red were observed both inside and outside of MSCs (Figure 4(b)). In the contact condition, 0.1 mg/mL β -TCP micron particles further increased the positively stained area with alizarin red at 21 days (Figures 4(a)–4(c)). 0.1 mg/mL β -TCP micron particles increased expression levels of *runx2*, osteopontin, and type I collagen significantly in the contact condition but not in the noncontact condition (Figure 4(d)).

3.5. β -TCP Micron Particles Affect Calcium and Phosphorus Concentrations in Culture Medium. In the contact condition, 0.1 mg/mL β -TCP micron particles increased calcium concentration in medium at 7, 14, and 21 days (Figure 5). In

the noncontact condition, 1.0 mg/mL β -TCP micron particles decreased calcium and phosphorus concentrations in culture medium at 2, 7, 14, and 21 days.

3.6. β -TCP Micron Particles Are [Phagocytosed] by MSCs. Microscopic analyses showed that β -TCP micron particles were still located in extracellular spaces at 30 minutes (Figure 6(a)). Many particles were contained in intracellular spaces, but some particles were still observed in extracellular spaces at 3 days. Most particles were contained in MSCs at 7 days, and MSCs containing particles formed multilayered at 21 days.

Transmission electron microscopic analyses revealed that β -TCP micron particles were located in the cytoplasm of MSCs at 7 days (Figure 6(b)). A magnified image showed no cytotoxic findings such as disruptions of the cell membrane, nuclear envelope, or cell organelle. A further magnified image demonstrated that the particles were contained in membrane which was called phagosome (open arrow). The phagosome was adjacent to lysosome (black arrow head) and lamellar body (white arrow head). The border of the particles was blurred (arrow).

4. Discussion

The effects of dosages and particle sizes of calcium phosphate have been reported in the past studies. Huang et al. reported macrophage released lactate dehydrogenase (LDH) when in contact with high concentrations of nanosized hydroxyapatite [16]. Contrary, Lange et al. reported that the release of LDH or TNF- α from macrophages was not altered among four different amounts of particles. They also reported that smaller particles, whose sizes were between 1 and 3 μm , did not increase release of LDH and TNF- α compared to those of larger ones [5]. All of these studies mentioned the effect of calcium phosphate particles from the standpoint of immunogenic responses and cytotoxicity through macrophages.

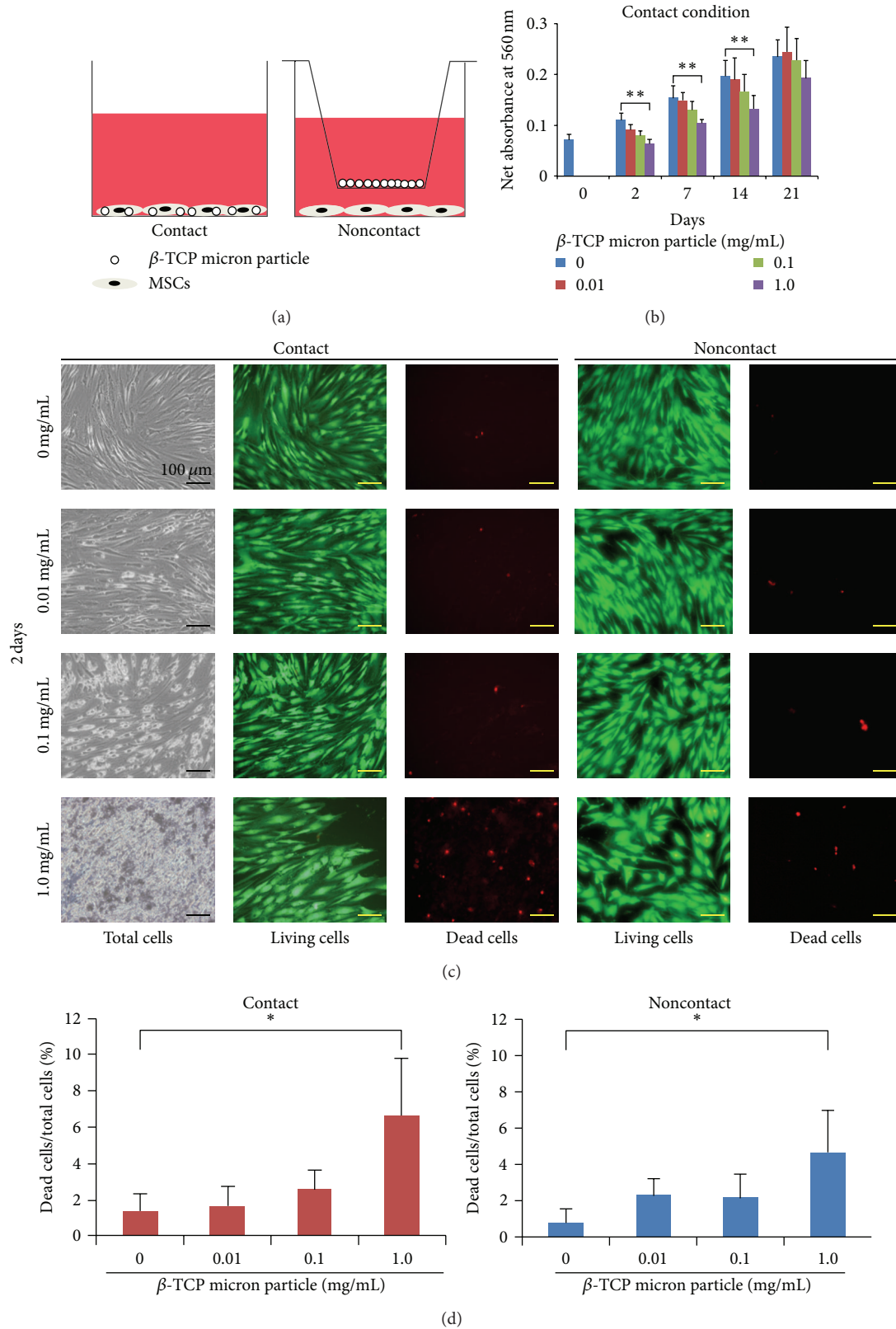


FIGURE 3: Effect of β -TCP micron particles on proliferation and cytotoxicity of MSCs. (a) Scheme for assays in the contact condition and the noncontact condition. (b) Proliferation. MSCs were cultured with complete culture medium (CCM) supplemented with various concentrations of β -TCP micron particles in the contact condition. Total cell number was measured by MTT assay. Averaged net absorbance with standard deviation is shown ($n = 7$, $**P < 0.01$ by the Kruskal-Wallis test). (c) Morphology of total, living, and dead cells in the contact and noncontact condition. (d) The ratio of dead cells to total cells (%) with standard deviation ($*P < 0.05$ by the Kruskal-Wallis test).

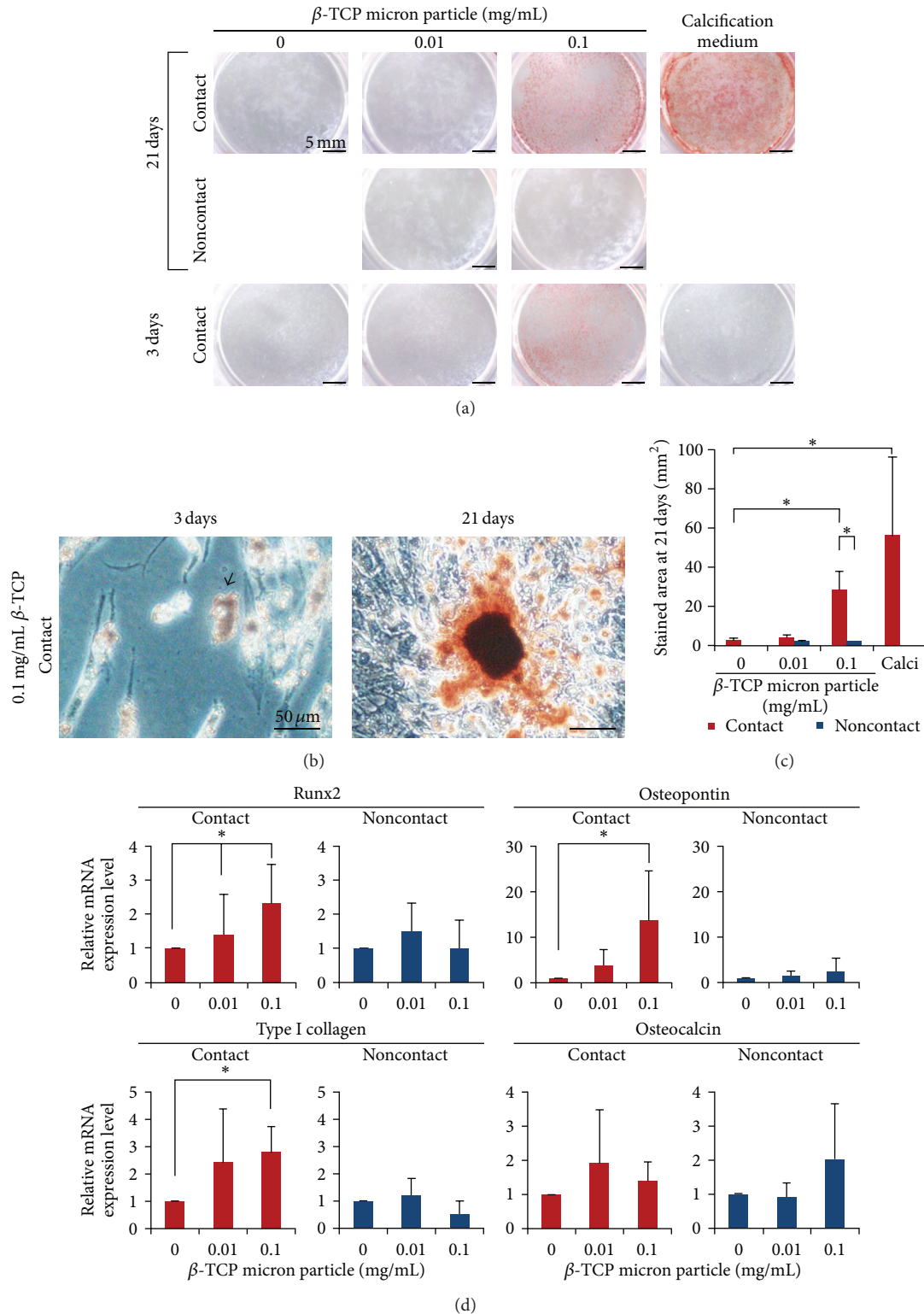


FIGURE 4: Effect of β -TCP micron particles on calcification of MSCs. (a) Alizarin red staining. MSCs were cultured without or with β -TCP micron particles in the contact or the noncontact condition for 21 days and in the contact condition for 3 days. As a positive control, MSCs were cultured in calcification medium. (b) High magnified pictures for MSCs stained with alizarin red. Black arrow indicates β -TCP micron particles stained with alizarin red located outside of MSCs. (c) Stained area at 21 days with alizarin red, which was calculated by subtracting stained area at 3 days in the contact condition. Averaged area with standard deviation is shown ($n = 6$, $*P < 0.05$ by the Kruskal-Wallis test). (d) Osteogenesis-related gene expressions by real-time PCR analysis. Averaged relative mRNA expression level with standard deviation is shown ($n = 6$, $*P < 0.05$ by the Kruskal-Wallis test).

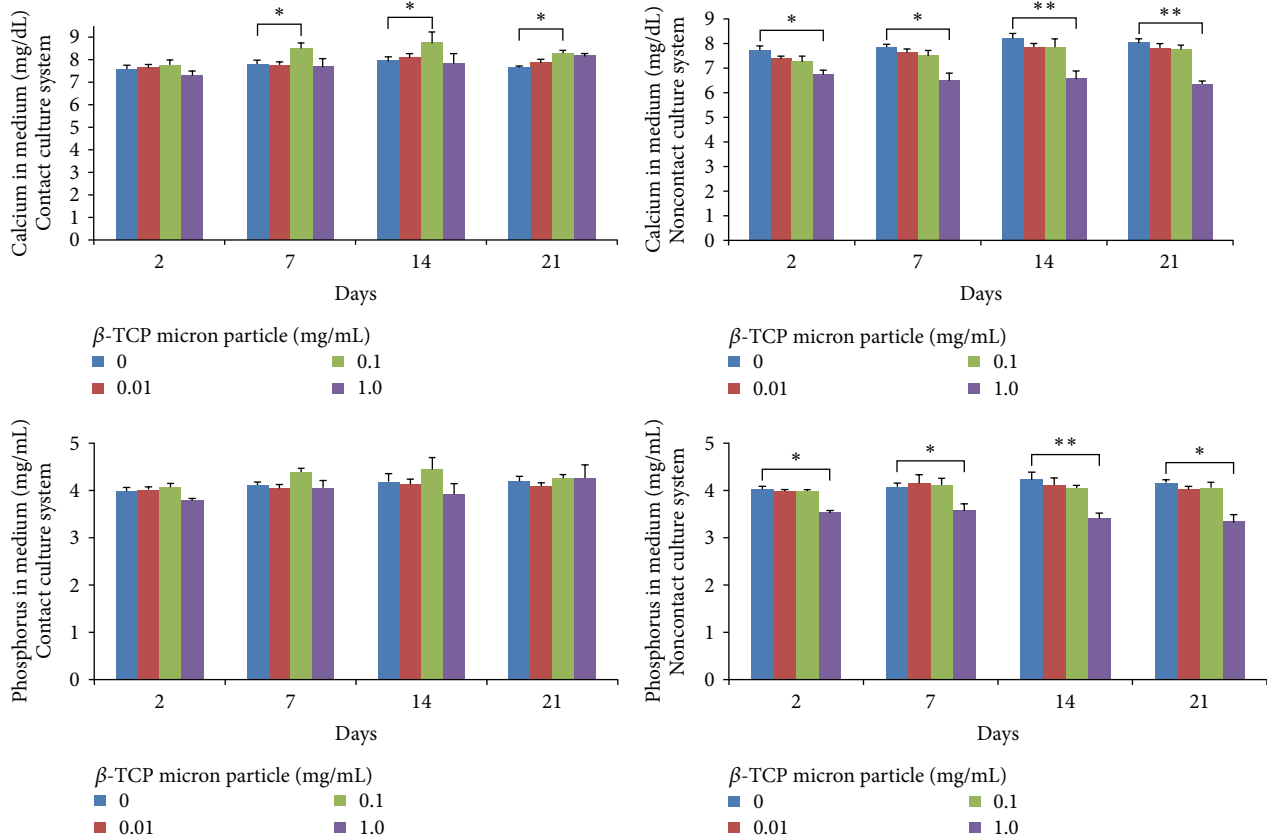


FIGURE 5: Calcium and phosphorus concentrations in medium treated with β -TCP micron particles. Averaged concentrations with standard deviation are shown ($n = 7$, * $P < 0.05$, ** $P < 0.01$ by the Kruskal-Wallis test).

In this study, we used MSCs in order to examine the effect of β -TCP micron particles. MSCs have much greater expansive potential than osteoblasts [17] and multilineage differentiation potential including osteogenesis. Moreover, the risk of tumorigenesis is extremely low [7]. MSCs are one of the promising cell sources for bone regeneration [18]. A combination of cytokines and scaffolds improves the function of MSCs for bone formation [10, 11]. Several papers have reported that the use of β -TCP scaffold enhances bone formation of MSCs [19]. Therefore, we focused on MSCs in this study.

MSCs could be isolated from various tissues such as synovium [20], adipose tissue [21], and skeletal muscle [22], in addition to bone marrow [6]. In this study, we used MSCs derived from synovium, and we confirmed that synovial MSCs had an osteogenic potential by alizarin red staining, RT-PCR analysis, and measuring ALP activity. According to our previous studies, synovial MSCs had a similar osteogenic potential to bone marrow MSCs [23, 24], and synovial MSCs had a higher proliferative capacity than that of bone marrow MSCs when cultured with autologous human serum [25]. To examine whether the effect of β -TCP micron particles on MSCs depends on their original tissues would be an interesting future study.

1.0 mg/mL β -TCP micron particles inhibited proliferation and increased dead cells of MSCs in the contact condition. To account for these results, three possible reasons could be proposed. Firstly, low concentrations of calcium and phosphorus in medium might have affected proliferation and viability of MSCs. 1.0 mg/mL β -TCP micron particles significantly decreased calcium and phosphorus concentrations and increased the ratio of dead cells at 2 days in the noncontact condition. These results correspond to those of a previous study in which nanoparticles of hydroxyapatite were examined by Liu et al. A high concentration of nanosized hydroxyapatite particles reduced calcium and phosphorus concentrations in culture medium, resulting in inhibited proliferation of bone marrow MSCs [26]. Secondly, an excessive amount of β -TCP taken up by MSCs might have been toxic because the inhibitory effect of β -TCP micron particles on proliferation of MSCs appeared to be dose-dependent at 2, 7, and 14 days without significant changes of calcium and phosphorus concentrations in medium in the contact condition. Thirdly, the transition of the MSCs from the proliferative phase into the differential phase might have resulted in inhibition of proliferation. MSCs are a heterogeneous population and only MSCs in the osteogenic lineage survive and others die in calcification medium.

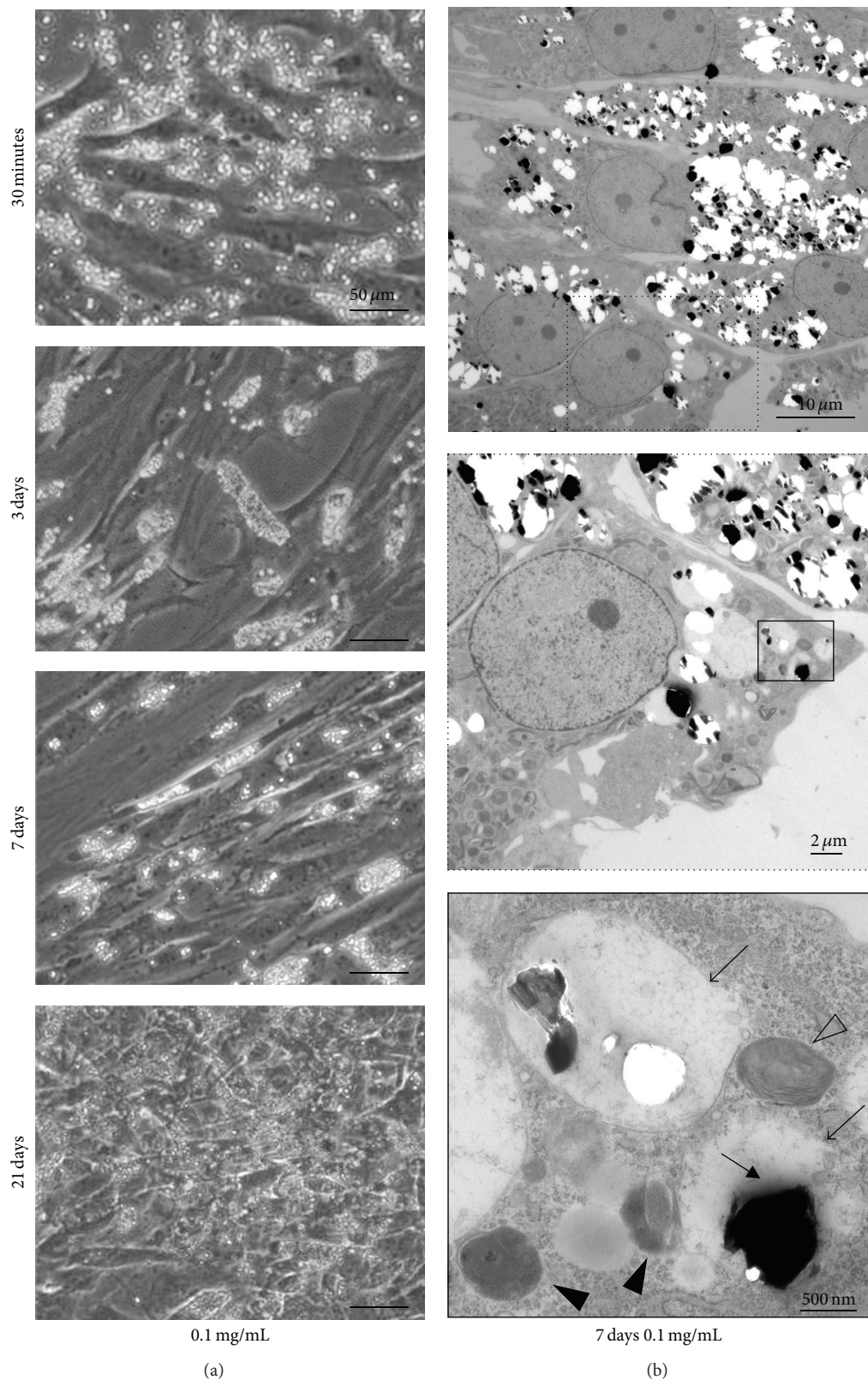


FIGURE 6: Morphology of MSCs cultured with β -TCP micron particles. (a) Light microscopic images. MSCs were cultured with 0.1 mg/mL in the contact condition. (b) Transmission electron microscopic images for MSCs at 7 days. Each area indicated by a square is magnified. β -TCP micron particles are indicated with arrow, phagosome with open arrow, lysosome with black arrow head, and lamellar body with white arrow head.

We evaluated the pH value in medium by litmus paper, and it was maintained between 7.4 and 7.6 after treatment of β -TCP micron particles in both contact and noncontact condition (data not shown). This indicates that pH was not affected by β -TCP micron particles.

As mentioned above, β -TCP micron particles affected calcium and phosphorus concentrations in medium. Interestingly, 1.0 mg/mL β -TCP micron particles decreased calcium and phosphorus concentrations only in the noncontact condition. In addition, we evaluated calcium and phosphorus concentrations in medium without any cells and found that their concentrations decreased dose dependently (data not shown). One possible reason for this could be that the β -TCP micron particles absorbed calcium and phosphorus in medium. This finding corresponds to the one observed in the previous study in which nanosized hydroxyapatite particles were used [26]. Contrarily, in the contact condition, 0.1 mg/mL β -TCP micron particles significantly increased calcium concentration at 7 days and thereafter, instead of decreasing it. β -TCP micron particles were already taken up by MSCs at 3 days and they appeared to be dissolved in phagosomes at 7 days. These findings suggest that MSCs dissolved β -TCP micron particles and supplied calcium in medium in the contact condition.

Treatment of 0.1 mg/mL β -TCP micron particles for MSCs in the contact condition increased stainability with alizarin red at 21 days and also enhanced expressions of runx2, osteopontin, and type I collagen, markers for osteogenic differentiation [27, 28]. However, expression of osteocalcin, a late marker for osteogenesis, was not significantly increased. These findings indicate that MSCs did not fully differentiate into mature osteoblasts.

For evaluation of calcification by alizarin red staining, the influence of β -TCP micron particles themselves should be taken into account. In the contact condition, apparently, 0.1 mg/mL β -TCP micron particles already increased stainability with alizarin red at 3 days, but β -TCP micron particles stained red were observed outside of MSCs in addition to inside. Osteogenesis-related gene expressions were not increased at 3 days (data not shown). The difference calculated by subtracting the positively stained area with alizarin red at 3 days from that at 21 days would be the actual positively stained area produced by MSCs, as we demonstrated in Figure 4(c).

0.1 mg/mL β -TCP micron particles in the contact condition promoted calcification of MSCs. On the other hand, in the noncontact condition, β -TCP did not alter alizarin red staining and osteogenesis-related gene expressions, showing that the indirect effect of β -TCP micron particles did not affect osteogenic differentiation of MSCs. Two possible mechanisms could be proposed to account how β -TCP micron particles promoted calcification of MSCs. The first mechanism is due to increase of calcium concentration inside and outside of MSCs. Previous studies reported that an elevated concentration of calcium was crucial for *in vitro* mineralization of osteoblast-like cells [29, 30]. The second mechanism is due to increase of bone matrix adhering to

MSCs induced by β -TCP micron particles. Weißenböck et al. reported that bone substitute easily bound to osteogenic proteins due to its high affinity, and it supplied bone matrix proteins to MSCs and promoted osteogenic differentiation [31]. Huang et al. reported that MSCs adhering to bone substitute led to change of cytoskeletal organization of osteoblast-like cells [16]. It would be an interesting future study to distinguish the mechanisms of enhancing mineralization of MSCs between β -TCP micron particles used in this study and larger ones which cannot be taken up by MSCs.

β -TCP micron particles were localized in phagosome and not in lysosome. This may have been due to the diameter of the β -TCP micron particles. The diameter of the β -TCP micron particles we used was 1 to 10 μ m, larger than that of lysosome whose size ranged from 0.5 to 1.0 μ m in diameter. Some lysosomes made contact with the phagosome which included the particles (Figure 6(b)). Thus, we supposed that the phagosome might have become phagolysosome by connecting with the lysosome and that the particles were dissolved in it. van Buul et al. demonstrated that MSCs had a potential to phagocyte inorganic substances [32]; however, there have been no reports showing an ability of MSCs to phagocyte bone graft substitute.

In conclusion, 0.1 mg/mL β -TCP promoted calcification of MSCs evaluated by alizarin red staining and enhanced osteogenesis-related gene expressions. 0.1 mg/mL β -TCP also increased calcium concentration in medium. Transmission electron microscopy demonstrated that β -TCP micron particles were localized in the phagosome of MSCs, thus dissolving the particles.

Conflict of Interests

Y. Hakamatsuka is an employee of the manufacturers of β -TCP micron particles. He did not interfere with the conduct of the study, and the authors take full responsibility for the study. None of the authors has any direct financial relation with the commercial identities mentioned in this paper that might lead to a conflict of interests.

Acknowledgments

This study was supported by grants from the Japanese Ministry of Education Global Center of Excellence Program, the International Research Center for Molecular Science in Tooth and Bone Diseases to T. Muneta, and a Health and Labor Sciences Research Grant, Research on Regenerative Medicine for Clinical Application to I. Sekiya. β -TCP micron particles were provided by Olympus Corporation. The authors thank Miyoko Ojima for her expert help and Izumi Nakagawa for management of their laboratory.

References

- [1] A. Ogose, T. Hotta, H. Kawashima et al., "Comparison of hydroxyapatite and beta tricalcium phosphate as bone substitutes after excision of bone tumors," *Journal of Biomedical Materials Research B*, vol. 72, no. 1, pp. 94–101, 2005.

- [2] P. Kasten, I. Beyen, P. Niemeyer, R. Luginbühl, M. Bohner, and W. Richter, "Porosity and pore size of β -tricalcium phosphate scaffold can influence protein production and osteogenic differentiation of human mesenchymal stem cells: an in vitro and in vivo study," *Acta Biomaterialia*, vol. 4, no. 6, pp. 1904–1915, 2008.
- [3] L. Galois, D. Mainard, and J. P. Delagoutte, "Beta-tricalcium phosphate ceramic as a bone substitute in orthopaedic surgery," *International Orthopaedics*, vol. 26, no. 2, pp. 109–115, 2002.
- [4] J. Dong, T. Uemura, Y. Shirasaki, and T. Tateishi, "Promotion of bone formation using highly pure porous β -TCP combined with bone marrow-derived osteoprogenitor cells," *Biomaterials*, vol. 23, no. 23, pp. 4493–4502, 2002.
- [5] T. Lange, A. F. Schilling, F. Peters, J. Mujas, D. Wicklein, and M. Amling, "Size dependent induction of proinflammatory cytokines and cytotoxicity of particulate beta-tricalciumphosphate in vitro," *Biomaterials*, vol. 32, no. 17, pp. 4067–4075, 2012.
- [6] D. J. Prockop, "Marrow stromal cells as stem cells for non-hematopoietic tissues," *Science*, vol. 276, no. 5309, pp. 71–74, 1997.
- [7] M. F. Pittenger, A. M. Mackay, S. C. Beck et al., "Multilineage potential of adult human mesenchymal stem cells," *Science*, vol. 284, no. 5411, pp. 143–147, 1999.
- [8] R. Bielby, E. Jones, and D. McGonagle, "The role of mesenchymal stem cells in maintenance and repair of bone," *Injury*, vol. 38, supplement 1, pp. S26–S32, 2007.
- [9] S. P. Bruder, D. J. Fink, and A. I. Caplan, "Mesenchymal stem cells in bone development, bone repair, and skeletal regeneration therapy," *Journal of Cellular Biochemistry*, vol. 56, no. 3, pp. 283–294, 1994.
- [10] J. C. Reichert, A. Cipitria, D. R. Epari et al., "A tissue engineering solution for segmental defect regeneration in load-bearing long bones," *Science Translational Medicine*, vol. 4, no. 141, Article ID 141ra193.
- [11] C. Seebach, D. Henrich, C. Kähling et al., "Endothelial progenitor cells and mesenchymal stem cells seeded onto β -tcp granules enhance early vascularization and bone healing in a critical-sized bone defect in rats," *Tissue Engineering A*, vol. 16, no. 6, pp. 1961–1970, 2010.
- [12] M. Shimaya, T. Muneta, S. Ichinose, K. Tsuji, and I. Sekiya, "Magnesium enhances adherence and cartilage formation of synovial mesenchymal stem cells through integrins," *Osteoarthritis and Cartilage*, vol. 18, no. 10, pp. 1300–1309, 2010.
- [13] M. Horie, I. Sekiya, T. Muneta et al., "Intra-articular injected synovial stem cells differentiate into meniscal cells directly and promote meniscal regeneration without mobilization to distant organs in rat massive meniscal defect," *Stem Cells*, vol. 27, no. 4, pp. 878–887, 2009.
- [14] T. Niikura, D. J. Hak, and A. H. Reddi, "Global gene profiling reveals a downregulation of BMP gene expression in experimental atrophic nonunions compared to standard healing fractures," *Journal of Orthopaedic Research*, vol. 24, no. 7, pp. 1463–1471, 2006.
- [15] M. Dominici, K. Le Blanc, I. Mueller et al., "Minimal criteria for defining multipotent mesenchymal stromal cells. The International Society for Cellular Therapy position statement," *Cytotherapy*, vol. 8, no. 4, pp. 315–317, 2006.
- [16] J. Huang, S. M. Best, W. Bonfield et al., "In vitro assessment of the biological response to nano-sized hydroxyapatite," *Journal of Materials Science*, vol. 15, no. 4, pp. 441–445, 2004.
- [17] A. J. Salgado, O. P. Coutinho, and R. L. Reis, "Bone tissue engineering: State of the art and future trends," *Macromolecular Bioscience*, vol. 4, no. 8, pp. 743–765, 2004.
- [18] J. Wagner, T. Kean, R. Young, J. E. Dennis, and A. I. Caplan, "Optimizing mesenchymal stem cell-based therapeutics," *Current Opinion in Biotechnology*, vol. 20, no. 5, pp. 531–536, 2009.
- [19] N. Kotobuki, D. Kawagoe, D. Nomura et al., "Observation and quantitative analysis of rat bone marrow stromal cells cultured in vitro on newly formed transparent β -tricalcium phosphate," *Journal of Materials Science*, vol. 17, no. 1, pp. 33–41, 2006.
- [20] C. de Bari, F. dell'Accio, P. Tylzanowski, and F. P. Luyten, "Multipotent mesenchymal stem cells from adult human synovial membrane," *Arthritis & Rheumatism*, vol. 44, no. 8, pp. 1928–1942, 2001.
- [21] P. A. Zuk, M. Zhu, P. Ashjian et al., "Human adipose tissue is a source of multipotent stem cells," *Molecular Biology of the Cell*, vol. 13, no. 12, pp. 4279–4295, 2002.
- [22] B. Cao, B. Zheng, R. J. Jankowski et al., "Muscle stem cells differentiate into haematopoietic lineages but retain myogenic potential," *Nature Cell Biology*, vol. 5, no. 7, pp. 640–646, 2003.
- [23] Y. Sakaguchi, I. Sekiya, K. Yagishita, and T. Muneta, "Comparison of human stem cells derived from various mesenchymal tissues: superiority of synovium as a cell source," *Arthritis & Rheumatism*, vol. 52, no. 8, pp. 2521–2529, 2005.
- [24] H. Yoshimura, T. Muneta, A. Nimura, A. Yokoyama, H. Koga, and I. Sekiya, "Comparison of rat mesenchymal stem cells derived from bone marrow, synovium, periosteum, adipose tissue, and muscle," *Cell and Tissue Research*, vol. 327, no. 3, pp. 449–462, 2007.
- [25] A. Nimura, T. Muneta, H. Koga et al., "Increased proliferation of human synovial mesenchymal stem cells with autologous human serum: comparisons with bone marrow mesenchymal stem cells and with fetal bovine serum," *Arthritis & Rheumatism*, vol. 58, no. 2, pp. 501–510, 2008.
- [26] Y. Liu, G. Wang, Y. Cai et al., "In vitro effects of nanophase hydroxyapatite particles on proliferation and osteogenic differentiation of bone marrow-derived mesenchymal stem cells," *Journal of Biomedical Materials Research A*, vol. 90, no. 4, pp. 1083–1091, 2009.
- [27] H. Lu, N. Kawazoe, T. Tateishi, G. Chen, X. Jin, and J. Chang, "In vitro proliferation and osteogenic differentiation of human bone marrow-derived mesenchymal stem cells cultured with hardystonite ($\text{Ca}_2\text{ZnSi}_2\text{O}_7$) and β -TCP ceramics," *Journal of Biomaterials Applications*, vol. 25, no. 1, pp. 39–56, 2010.
- [28] Y. Takahashi, M. Yamamoto, and Y. Tabata, "Osteogenic differentiation of mesenchymal stem cells in biodegradable sponges composed of gelatin and β -tricalcium phosphate," *Biomaterials*, vol. 26, no. 17, pp. 3587–3596, 2005.
- [29] Y. L. Chang, C. M. Stanford, and J. C. Keller, "Calcium and phosphate supplementation promotes bone cell mineralization: implications for hydroxyapatite (HA)-enhanced bone formation," *Journal of Biomedical Materials Research*, vol. 52, no. 2, pp. 270–278, 2000.
- [30] H. Matsuoka, H. Akiyama, Y. Okada et al., "In vitro analysis of the stimulation of bone formation by highly bioactive apatite- and wollastonite-containing glass-ceramic: released calcium ions promote osteogenic differentiation in osteoblastic ROS17/2. 8 cells," *Journal of Biomedical Materials Research*, vol. 47, no. 2, pp. 176–188, 1999.
- [31] M. Weißenböck, E. Stein, G. Undt, R. Ewers, G. Lauer, and D. Turhani, "Particle size of hydroxyapatite granules calcified from

red algae affects the osteogenic potential of human mesenchymal stem cells in vitro,” *Cells Tissues Organs*, vol. 182, no. 2, pp. 79–88, 2006.

- [32] G. M. van Buul, G. Kotek, P. A. Wielopolski et al., “Clinically translatable cell tracking and quantification by MRI in cartilage repair using superparamagnetic iron oxides,” *PLoS ONE*, vol. 6, no. 2, Article ID e17001, 2011.

Research Article

Polymer-Assisted Hydrothermal Synthesis of Hierarchically Arranged Hydroxyapatite Nanoceramic

A. Joseph Nathanael, Sung Soo Han, and Tae Hwan Oh

Department of Nano, Medical and Polymer Materials, College of Engineering, Yeungnam University, Gyeongsan 712749, Republic of Korea

Correspondence should be addressed to Tae Hwan Oh; taehwanoh@ynu.ac.kr

Received 3 May 2013; Accepted 18 June 2013

Academic Editor: Eng San Thian

Copyright © 2013 A. Joseph Nathanael et al. This is an open access article distributed under the Creative Commons Attribution License, which permits unrestricted use, distribution, and reproduction in any medium, provided the original work is properly cited.

Flower-like hydroxyapatite (HA) nanostructures were synthesized by a polymer-assisted hydrothermal method. The thickness of the petals/plates decreased from 200 nm to 40 nm as the polymer concentration increased. The thickness also decreased as the hydrothermal treatment time increased from 6 to 12 hr. The HRTEM and SAED patterns suggest that the floral-like HA nanostructures are single crystalline in nature. Structural analysis based on XRD and Raman experiments implied that the produced nanostructure is a pure form of HA without any other impurities. The possible formation mechanism was discussed for the formation of flower-like HA nanostructures during polymer-assisted hydrothermal synthesis. Finally, *in vitro* cellular analysis revealed that the hierarchically arranged HA nanoceramic had improved cell viability relative to other structures. The cells were actively proliferated over these nanostructures due to lower cytotoxicity. Overall, the size and the crystallinity of the nanostructures played a role in improving the cell proliferation.

1. Introduction

The functional properties of inorganic compounds or inorganic/organic hybrids are related to their shape, size, and dimension [1–4]. Three-dimensional (3D) nano/microstructures have recently received a great deal of attention in material science research [5–8]. Substantial developments have been made in the fabrication of three-dimensional nanomaterials and they are now applied in optoelectronic devices [9], drug delivery systems [10], sensors [11], super capacitors [12, 13], and as catalysts [2]. Formations of uniform hierarchical superstructures using nanoparticles such as nanorods, nanoplates, and nanospheres with diameters ranging from nano- to microscale dimensions are especially desirable due to their interesting functional properties.

Tunable functional properties of inorganic materials have been achieved by the self-assembly of their nanoparticles into nanostructures [14]. These functional properties of the nanostructures are dependent on the design and control of the size, shape, and orientation of the building blocks. Investigations of the self-assembly of two-dimensional (2D) and

three-dimensional (3D) nanoparticles have expanded rapidly [15, 16] because of their fascinating functional properties and potential applications in various fields [17].

In the human body, the structure of bone displays a hierarchical arrangement, but it differs significantly at different locations. Nevertheless, mineralized collagen consisting of the basic nanoscale structure of bone remains the same [18, 19]. It has been reported that nanorods such as crystals of hydroxyapatite (HA) are deposited parallel with the *c*-axis aligned with the long axis in calcified tissues [20, 21]. Additionally, experiments have shown that the biocompatibility and bioactivity of bone cells on HA are enhanced by the oriented structure of HA [22]. Hence, this structure encourages the design and fabrication of biomaterials.

Hydroxyapatite (HA, $\text{Ca}_{10}(\text{PO}_4)_6(\text{OH})_2$) has been widely used in biomedicine as filler [20], for bone repair and bone tissue regeneration [23], and as a drug delivery carrier owing to its good biocompatibility and bioactivity and its high osteoconductive and/or osteoinductive properties [20, 22]. HA is the most stable calcium phosphate phase under physiological conditions and exists all over the human body as

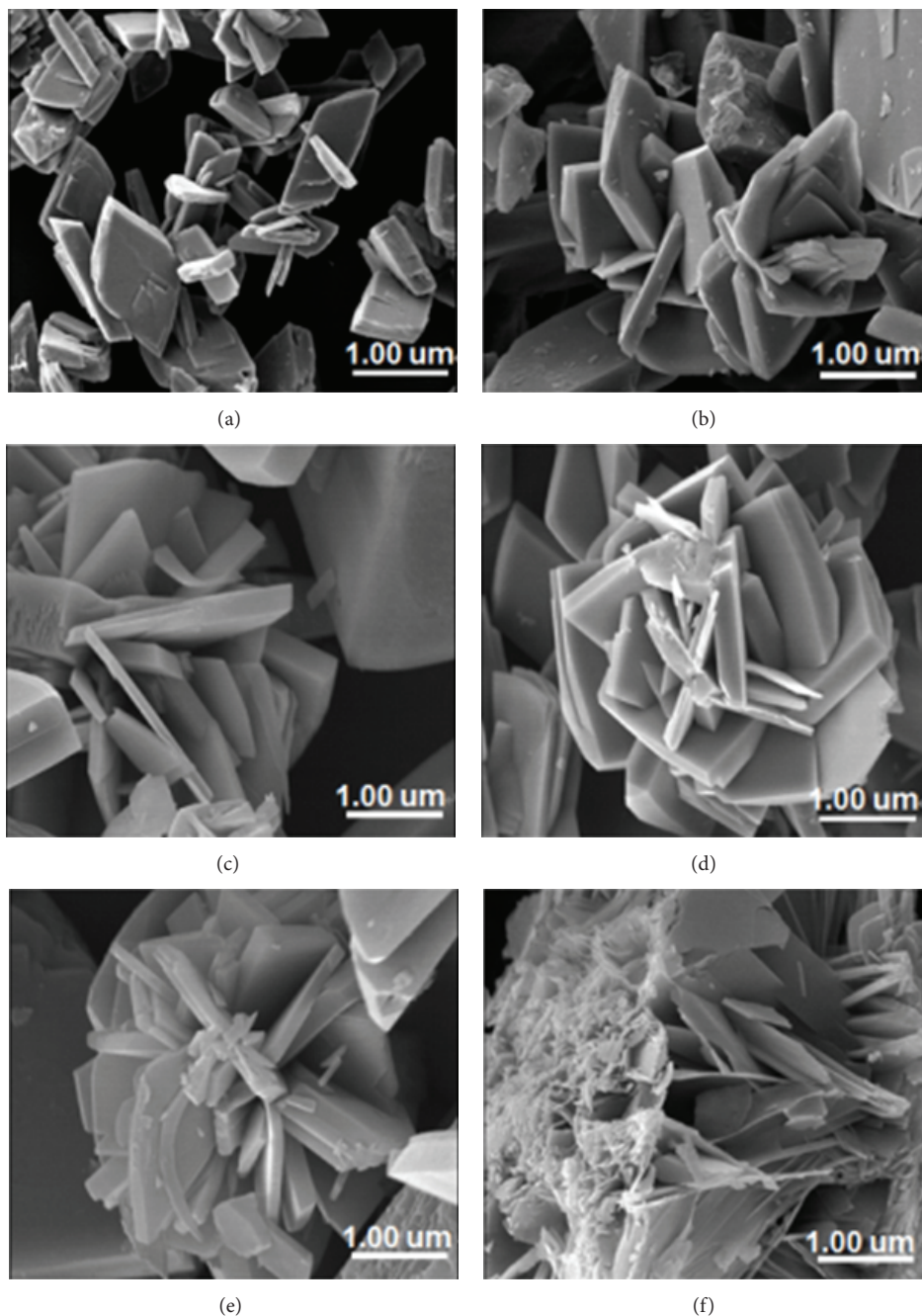


FIGURE 1: FESEM images of polymer-assisted HA nanostructures with PAM concentrations of 2, 3, and 4 g/L (a, c, and e) and hydrothermal reaction times of 6 hr and (b, d, and f) 12 hr.

the main inorganic constituent of bone and teeth [24]. HA also has many important industrial and biomedical applications in catalysis, ion exchange, sensors, and bioceramics [2, 10, 11]. HA is a polar hexagonal and highly anisotropic crystal that naturally grows into a 1D nanostructure [17]. Nanostructured HA possesses higher specific surface areas that enhance the adhesion of cells, proteins, and drugs. Hence, the miniaturization of size and tuning of the morphology are an important factor for current biomedical research [23].

Many previous reports have shown that polymers such as PEG (poly(ethylene glycol)) [25–28], PVP (polyvinyl pyrrolidone) [29, 30], and PAM (polyacrylamide) [31] are useful components in the formation of one- and zero-dimension nanosized materials. Some studies have investigated the preparation of nanomaterials such as ZnO [25, 29, 31], MoO₂ whiskers [26], and Al₂O₃-TiO₂ composite nanoparticles [27] using polymer-assisted synthesis. PEG-assisted HA nanoparticle synthesis was reported by Tseng et al. [28], while metal

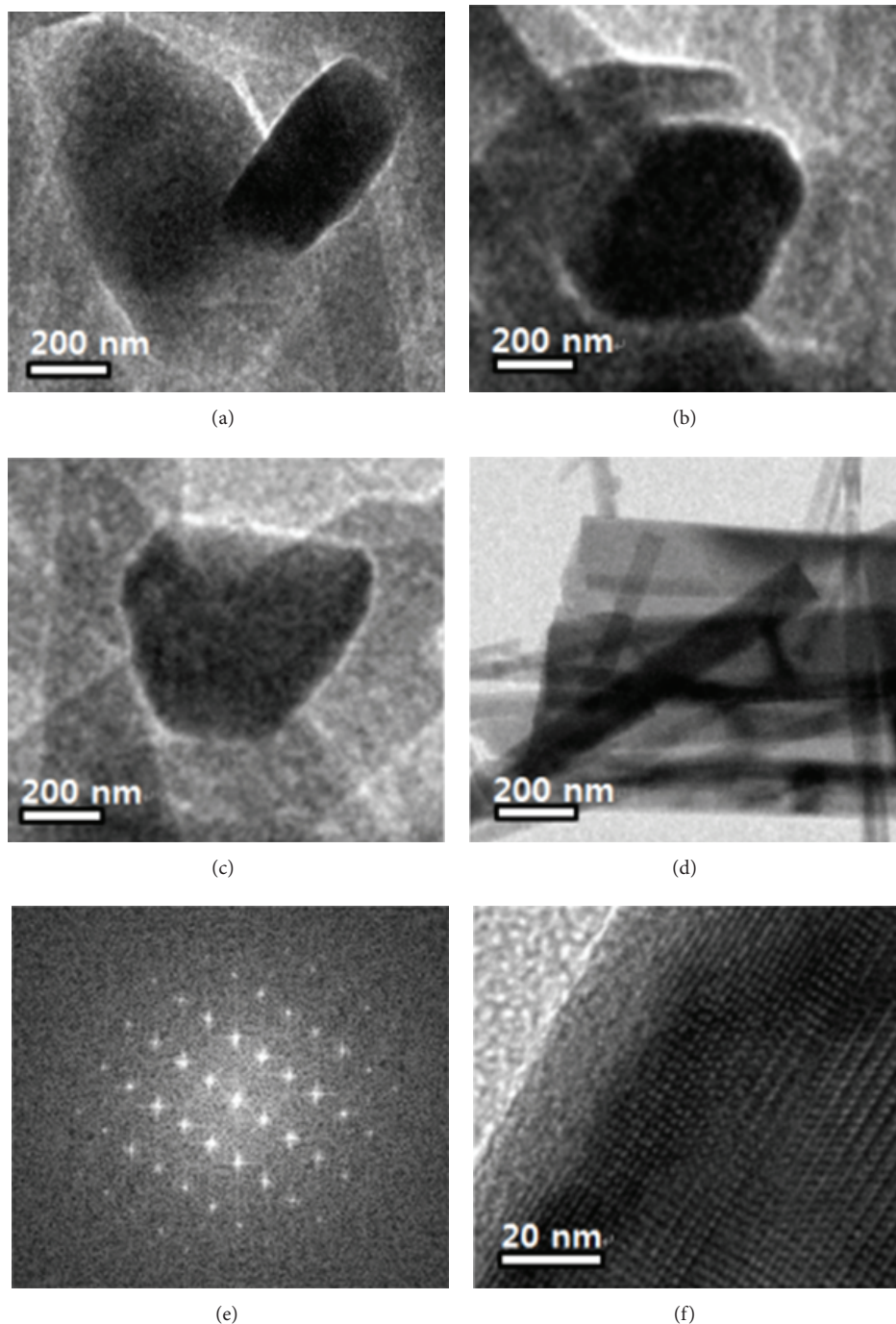


FIGURE 2: TEM images of polymer-assisted HA nanostructures with PAM concentrations of 2 and 4 g/L (a, b) and hydrothermal reaction times of 6 hr and (c, d) 12 hr. (e, f) FFT pattern and HRTEM image of (d).

nanoparticle synthesis in the presence of polymer was reported by Jeon et al. [30]. In the present study, we reported the PAM-assisted hydrothermal synthesis of hierarchically arranged flower-like HA nanostructures and proposed the formation mechanism. We also conducted *in vitro* cellular analysis to evaluate the use of these nanostructures as a possible material for biomedical applications.

2. Experimental Details

2.1. Materials and Methods. All chemicals were of analytical grade and were used without further purification. Calcium nitrate ($\text{Ca}(\text{NO}_3)_2 \cdot 4\text{H}_2\text{O}$) and diammonium phosphate ($(\text{NH}_4)_2\text{HPO}_4$) were used as calcium and phosphate sources. $\text{Ca}(\text{NO}_3)_2 \cdot 4\text{H}_2\text{O}$ and $(\text{NH}_4)_2\text{HPO}_4$ were separately dissolved

in double distilled water. The Ca to P ratio was taken to be the stoichiometric ratio of HA (1.67). After stirring for 1 hr, different amounts (2, 3, and 4 g/L) of polymer (polyacrylamide, PAM, Mw 10, 000) were added to the calcium precursor solution. Next, $(\text{NH}_4)_2\text{HPO}_4$ solution was added to the $\text{Ca}(\text{NO}_3)_2 \cdot 4\text{H}_2\text{O}$ /polymer solution, after which the obtained suspension was transferred into a 50 mL Teflon-lined stainless steel autoclave and heated at 180°C for 6 and 12 hrs. The suspension was then allowed to cool to room temperature, after which the obtained precipitate was washed several times with ethanol and distilled water. Finally, the powder was dried at 100°C before further characterization.

2.2. Characterization. All samples were analyzed in detail using different methods. Structural analysis was carried out using X-ray diffraction analysis (XRD, Rigaku, D/MAX 2500H). Field emission scanning electron microscopy (FESEM, Helios 600) analysis was conducted to identify morphological variations due to different processing conditions. Further in-depth analysis was carried out by transmission electron microscopy (FE-TEM, Tecnai F30 S-Twin). Raman analysis was conducted using a laser Raman spectrometer (Renishaw inVia, Raman Microscope) at an output power of 10 mW of a 514 nm Ar^+ laser. Spectra were corrected using the LO-phonon mode of Si (100) substrates observed at 520.5 eV.

Human osteosarcoma cells (MG-63 cells) were cultured to determine the cell viability of polymer-assisted microstructures. Briefly, cells were cultured at 37°C in a humidified atmosphere of 5% CO_2 in air containing cell culture medium (DMEM media (phenol red free) Welgene), 10% fetal bovine serum (FBS, Welgene), 2 mM L-glutamine, 1% penicillin, and streptomycin mixture (Antibiotic, Gibco). The cells were then seeded in 96-well microassay plates at a concentration of 1×10^4 cells/well and cultured for 24 h. Sterilized HA nanoparticle samples were then added into the wells at a concentration of $100 \mu\text{g}/\text{mL}^{-1}$ and cocultured for 1, 2, or 3 days. The cell proliferation or viability of cells was then determined using a CCK-8 kit (Dojindo, CK-04-13). Five samples were tested for each culture time period and the mean value was reported.

3. Results and Discussion

3.1. Surface Morphology Analysis. Figure 1 shows the surface morphology based on FESEM analysis of the polymer-assisted HA microstructures. During short-term hydrothermal treatment (6 hr) with a lower polymer concentration, a microstructure with a thickness of 250 ± 30 nm, and a length of more than a micrometer was generated. As the PAM concentration and reaction temperature increased, bunch-like structures were formed at the cost of a single nanostructure. In addition, the reaction time and the PAM concentration also influenced the thickness of the particle. By increasing these two parameters, the thickness was considerably reduced and a flower bunch-like structure was formed. The thickness of the plate-like structure decreased from 250 nm to 40 nm as the hydrothermal reaction time

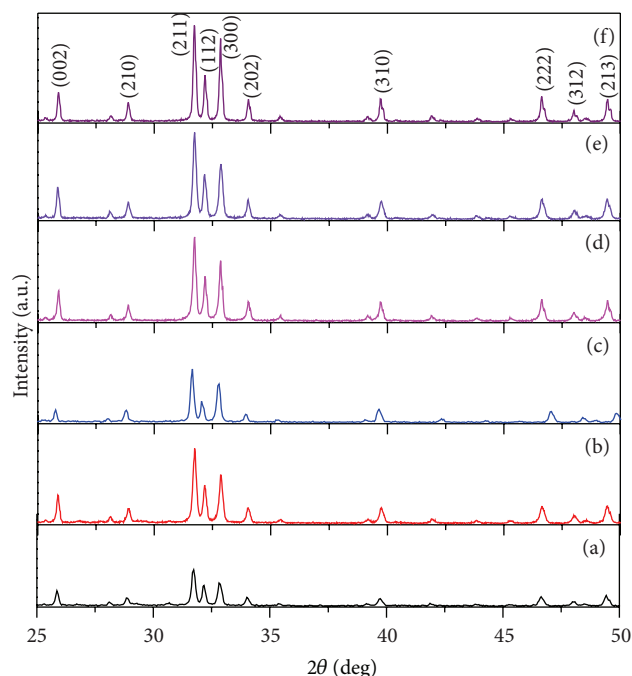


FIGURE 3: XRD pattern of polymer-assisted HA nanostructures with PAM concentrations of 2, 3, and 4 g/L (a, c, and e) and hydrothermal reaction times of 6 hr and (b, d, and f) 12 hr.

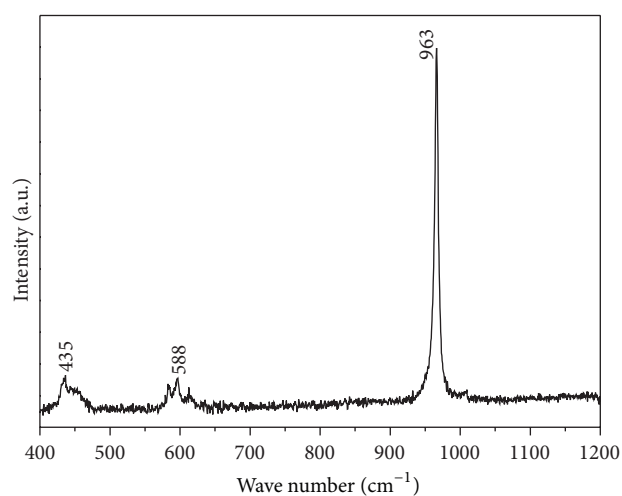


FIGURE 4: Raman spectrum of polymer-assisted HA nanostructures with PAM concentrations of 4 g/L and hydrothermal reaction times of 12 hr.

and the polymer concentration increased. Further increases in polymer concentration ruined the plate-like structure.

Further insight into the nanostructure was obtained by the TEM analysis as shown in Figure 2. Individual nanosheets/plates were observed upon TEM analysis. The spots in the FFT pattern (Figure 2(e)) indicated that the nanostructure is highly crystalline in nature. Figure 2 confirms the decrease in the thickness of the sheet structure as observed upon SEM analysis. The TEM image confirmed the reduction in thickness with increased polymer concentration.

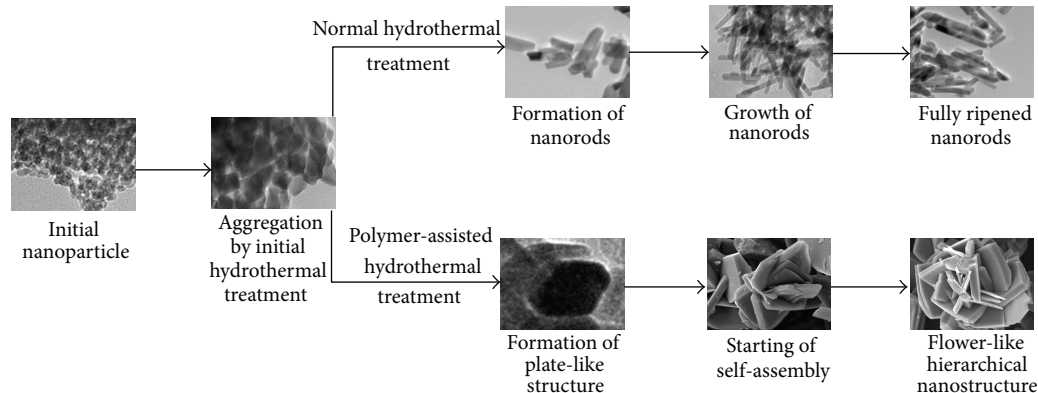


FIGURE 5: Schematic illustration of the formation mechanism of polymer-assisted HA nanostructures compared with pure HA nanorods.

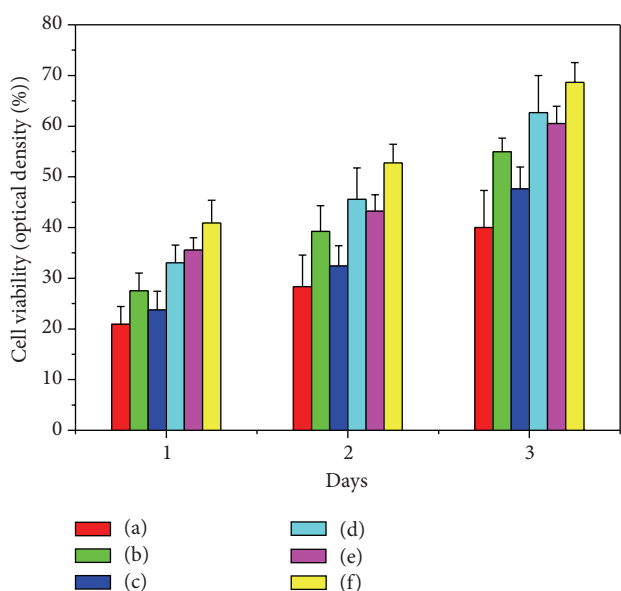


FIGURE 6: Cell viability on different days on polymer-assisted HA nanostructures with PAM concentration of 2, 3, and 4 g/L and hydrothermal reaction times of 6 hr (a, c, and e) and 12 hr (b, d, and f).

Increased polymer concentration also induced formation of the floral structure, but it was not clearly observed upon TEM because it was ultrasonically agitated for TEM analysis.

3.2. Structural Analysis. Structural analysis of the polymer-assisted HA nanoparticle was conducted using XRD. Figure 3 shows the XRD patterns of samples prepared under different conditions, which consisted of a well-crystalline phase with a hexagonal-structured HA (space group: P63/m (176)) [20]. No peaks corresponding to other secondary phases were observed in the samples. The reaction time in the hydrothermal method significantly influences the crystallinity of the material, thereby changing the intensity of the XRD peak. An initial reaction time of 6 hrs produced less peak intensity, while the intensity of the peak increased when the reaction time increased to 12 hrs.

The peaks present in the XRD patterns were readily indexed with the HA planes (002) at about 25.75° and (211), (112), (300), and (202) in the range 31° – 35° , with the lattice parameters of $a = 9.418 \text{ \AA}$ and $c = 6.884 \text{ \AA}$ (JCPDS card no. 09-0432). Lattice parameters were calculated for all samples. Both 9.41 – 9.42 \AA for the a -axis and 6.88 – 6.89 \AA for the c -axis showed that there were no significant changes with polymer-assisted hydrothermal treatment and that these values were very close to the reported value for bulk HA ($a = 9.418 \text{ \AA}$ and $c = 6.884 \text{ \AA}$) [23]. The average crystallite sizes, L , of the samples were calculated in this study using the following Debye-Scherrer formula [32]:

$$L = \frac{k\lambda}{\beta \cos \theta}, \quad (1)$$

where $k = 0.94$ (shape factor), λ is the wavelength of the radiation used (1.54056 \AA), β is the full width at half maximum of the peak in radians, and θ is the Bragg angle. The calculations were carried out for the highly intense peaks in the XRD pattern (Figure 3). From the calculations, we observed that the crystallite size decreased from 22 ± 5 to $10 \pm 3 \text{ nm}$ as the polymer concentration increased.

3.3. Raman Analysis. There was no significant change in the Raman peaks for the polymer-controlled synthesis of HA floral nanostructures. The peak at 963 cm^{-1} is characteristic of HA [23], which has a very strong PO_4 group. Specifically, this peak reflects the symmetric stretching mode (ν_1) of the PO_4 group (P–O bond). The degree of crystallinity of HA was identified using the position of this peak. When the peak was found at 963 cm^{-1} , it was more ordered, highly crystalline noncarbonated apatite, while at $\sim 958 \text{ cm}^{-1}$ it was polycrystalline apatite [23]. Hence, based on the data shown in Figure 4, the polymer-assisted HA produces the crystalline HA nanostructure well, confirming the XRD results. Along with this peak, additional weak peaks were found at 435 cm^{-1} (double degenerate bending mode (ν_2) of the PO_4 group (O–P–O bond)) and 588 and 610 cm^{-1} (triply degenerate bending mode (ν_4) of the PO_4 group (O–P–O bond)), which is also associated with the HA system [23]. Hence, the results of this study confirm that the addition of polymers

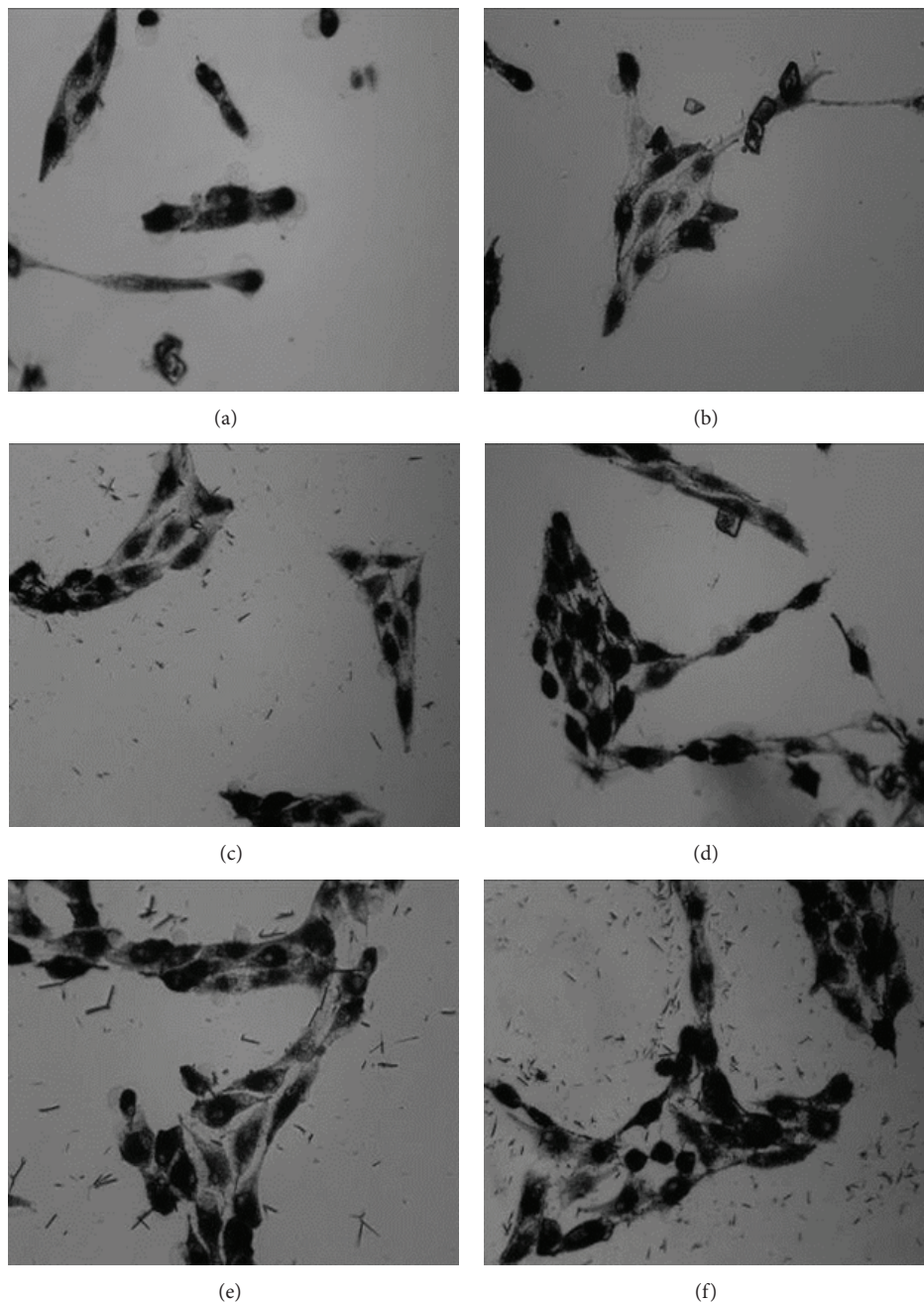


FIGURE 7: Optical images of cell spreading on polymer-assisted HA nanostructures with PAM concentrations of 2, 3, and 4 g/L and hydrothermal reaction times of 6 hr (a, c, and e) and 12 hr (b, d, and f).

in the preparation method does not affect the purity of the HA structure. Conversely, it provides better crystallinity and structural integrity.

3.4. Formation Mechanism. Based on the above experimental results, polymer-assisted self-assembly could be a formation mechanism for the nanostructured HA consisting of a nanosheet floral structure. In this mechanism, fine nanoparticles will be formed and grow as nanorods during initial nucleation in the hydrothermal treatment. The individual

nanorods will then be aggregated into a sheet-like structure induced by the well-known Ostwald ripening mechanism [23], after which the nanosheets self-assemble into the hierarchically arranged flower-like nanostructure. Normally, HA will grow preferentially along the 001 direction or c -axis. It is likely that the use of PAM restricts growth along the 001 direction; therefore, we obtained the sheet structure. It has been reported that in PAM, the side chain contains a large number of amide ligands that are able to coordinate with inorganic ions (likely Ca^{2+}) (the weakly exposed (001) face), leading to

a lower surface energy and restriction of growth along the 001 direction [31]. For nanostructures, this polymer adsorption can only occur on one face; otherwise electroneutrality would be violated [31]. This may explain why we obtained the sheet-like structure instead of rod-like morphology. The schematic representation of the formation mechanism of floral-like HA was given in Figure 5 in comparison with the formation of nanorods to enable better understanding.

The degree of the assembly increased, whereas the thickness of the sheet decreased with increasing PAM concentration and reaction time. Finally, nanostructured HA with a flower-like morphology assembled from nanosheets was fabricated.

It is clear that the polymer plays an important role in the formation of these flower-like bunch nanostructures. It should be noted that the experiments that did not include PAM in the solution did not produce flower-like nanostructures, but elongated microparticles instead. When a smaller quantity of PAM (2 g/L) was added, compact HA plates with a thickness of 200 nm were obtained (Figure 1) upon initiation of the floral structure. As the PAM concentration increased, the thickness rapidly decreased. These results suggest that PAM molecules slow down the crystal growth along the 001 orientation; therefore, this method provided a simple approach to controlling the thickness of the HA plates. The polymer molecules were selectively adsorbed on the basal plane, after which crystal growth along the 001 direction was suppressed under these conditions, but the crystals were still able to grow sideways.

3.5. In Vitro Cellular Analysis. The cell proliferation of the MG-63 human osteosarcoma cell on polymer assisted HA nanocrystals as a function of days is shown in Figure 6. Cell viability varied with changes in the morphology of HA crystals. The cell proliferation rate revealed that there was inappreciable cytotoxicity on the prepared HA micro/nanoparticles on MG-63 cells. The cells were evenly proliferated around the flower-like structure. The particle size/thickness of the floral-like structure plays a role in cell attachment of the nanoparticle. At the same time, the crystallinity of the sample due to heat treatment by the hydrothermal route also played a crucial role in cell proliferation. Figure 7 shows the optical images of cell proliferation on the floral-shaped HA nanoparticles. Cell spreading was higher for highly crystalline and nanostructured samples. Further investigation and control of this specific nanostructure will lead to future drug loading and delivery applications. Since HA is highly biocompatible, it will be a promising material for drug delivery application, especially for orthopedic and dental applications.

4. Conclusion

We synthesized a polymer-assisted hydrothermal method for the preparation of hierarchical flower-like hydroxyapatite nanostructures. The hierarchical morphology of HA is dependent on the polymer concentration and hydrothermal treatment time. Initially, when there was a lower polymer concentration and short reaction time, a sheet-like structure

with a thickness of more than 200 nm was generated and formation of a floral structure was initiated. The experimental results revealed that the hydroxyapatite flower-like structure possessed preferable biocompatible characteristics. The *in vitro* cell viability further revealed that the proliferation rate was higher for the hierarchically arranged HA nanostructure, confirming that size, uniformity, and crystallinity are important for tuning of the functional property. Thus, by controlling the preparation conditions and parameters, we can tune the functional property of the materials. Hence, the present HA nanostructure is a promising material for biomedical applications. Further, deciding parameters are under investigation, and possible use of this structure for drug loading and delivery is under consideration.

Conflict of Interests

The authors have no conflict of interests to declare.

Acknowledgment

This research was supported by Yeungnam University Research Grants in 2012.

References

- [1] H. T. Ng, J. Li, M. K. Smith et al., "Growth of epitaxial nanowires at the junctions of nanowalls," *Science*, vol. 300, no. 5623, p. 1249, 2003.
- [2] C. Burda, X. Chen, R. Narayanan, and M. A. El-Sayed, "Chemistry and properties of nanocrystals of different shapes," *Chemical Reviews*, vol. 105, no. 4, pp. 1025–1102, 2005.
- [3] J. Yang, C. Li, X. Zhang et al., "Self-assembled 3D architectures of $\text{LuBO}_3:\text{Eu}^{3+}$: phase-selective synthesis, growth mechanism, and tunable luminescent properties," *Chemistry: A European Journal*, vol. 14, no. 14, pp. 4336–4345, 2008.
- [4] A. Chen, X. Peng, K. Koczur, and B. Miller, "Super-hydrophobic tin oxide nanoflowers," *Chemical Communications*, vol. 10, no. 17, pp. 1964–1965, 2004.
- [5] C. Zhang, Z. Cheng, P. Yang et al., "Architectures of strontium hydroxyapatite microspheres: solvothermal synthesis and luminescence properties," *Langmuir*, vol. 25, no. 23, pp. 13591–13598, 2009.
- [6] L.-S. Zhong, J.-S. Hu, H.-P. Liang, A.-M. Cao, W.-G. Song, and L.-J. Wan, "Self-assembled 3D flowerlike iron oxide nanostructures and their application in water treatment," *Advanced Materials*, vol. 18, no. 18, pp. 2426–2431, 2006.
- [7] J. Liu, Q. Wu, and Y. Ding, "Self-assembly and fluorescent modification of hydroxyapatite nanoribbon spherulites," *European Journal of Inorganic Chemistry*, no. 20, pp. 4145–4149, 2005.
- [8] I.-S. Cho, D. W. Kim, S. Lee et al., "Synthesis of $\text{Cu}_2\text{PO}_4\text{OH}$ hierarchical superstructures with photocatalytic activity in visible light," *Advanced Functional Materials*, vol. 18, no. 15, pp. 2154–2162, 2008.
- [9] X. Duan, Y. Huang, Y. Cui, J. Wang, and C. M. Lieber, "Indium phosphide nanowires as building blocks for nanoscale electronic and optoelectronic devices," *Nature*, vol. 409, no. 6816, pp. 66–69, 2001.

- [10] Y. Cai, H. Pan, R. Xu, Q. Hu, N. Li, and R. Tang, "Ultrasonic controlled morphology transformation of hollow calcium phosphate nanospheres: a smart and biocompatible drug release system," *Chemistry of Materials*, vol. 19, no. 13, pp. 3081–3083, 2007.
- [11] F. Favier, E. C. Walter, M. P. Zach, T. Benter, and R. M. Penner, "Hydrogen sensors and switches from electrodeposited palladium mesowire arrays," *Science*, vol. 293, no. 5538, pp. 2227–2231, 2001.
- [12] S. Ghosh and O. Inganäs, "Conducting polymer hydrogels as 3D electrodes: applications for supercapacitors," *Advanced Materials*, vol. 11, no. 14, pp. 1214–1218, 1999.
- [13] D. R. Rolison and B. Dunn, "Electrically conductive oxide aerogels: new materials in electrochemistry," *Journal of Materials Chemistry*, vol. 11, no. 4, pp. 963–980, 2001.
- [14] A. N. Shipway, E. Katz, and I. Willner, "Nanoparticle arrays on surfaces for electronic, optical, and sensor applications," *ChemPhysChem*, vol. 1, no. 1, pp. 18–52, 2000.
- [15] T. Yonezawa, S. Onoue, and N. Kimizuka, "Self-organized superstructures of fluorocarbon-stabilized silver nanoparticles," *Advanced Materials*, vol. 13, no. 2, pp. 140–142, 2001.
- [16] R. Maoz, E. Frydman, S. R. Cohen, and J. Sagiv, "Constructive nanolithography: site-defined silver self-assembly on nanoelectrochemically patterned monolayer templates," *Advanced Materials*, vol. 12, no. 6, pp. 424–429, 2000.
- [17] J. Liu, K. Li, H. Wang, M. Zhu, H. Xu, and H. Yan, "Self-assembly of hydroxyapatite nanostructures by microwave irradiation," *Nanotechnology*, vol. 16, no. 1, pp. 82–87, 2005.
- [18] L. C. Palmer, C. J. Newcomb, S. R. Kaltz, E. D. Spoerke, and S. I. Stupp, "Biomimetic systems for hydroxyapatite mineralization inspired by bone and enamel," *Chemical Reviews*, vol. 108, no. 11, pp. 4754–4783, 2008.
- [19] F. Chen, Y.-J. Zhu, K.-W. Wang, and K.-L. Zhao, "Surfactant-free solvothermal synthesis of hydroxyapatite nanowire/nanotube ordered arrays with biomimetic structures," *CrystEngComm*, vol. 13, no. 6, pp. 1858–1863, 2011.
- [20] A. J. Nathanael, D. Mangalaraj, P. Chi Chen, and N. Ponpandian, "Enhanced mechanical strength of hydroxyapatite nanorods reinforced with polyethylene," *Journal of Nanoparticle Research*, vol. 13, no. 5, pp. 1841–1853, 2011.
- [21] S. V. Dorozhkin, "Calcium orthophosphates in nature, biology and medicine," *Materials*, vol. 2, no. 2, pp. 399–498, 2009.
- [22] A. J. Nathanael, S. I. Hong, D. Mangalaraj, N. Ponpandian, and P. C. Chen, "Template free growth of novel hydroxyapatite nanorings: formation mechanism and their enhanced functional properties," *Crystal Growth & Design*, vol. 12, no. 7, pp. 3565–3574, 2012.
- [23] L. M. Rodríguez-Lorenzo and M. Vallet-Regí, "Controlled crystallization of calcium phosphate apatites," *Chemistry of Materials*, vol. 12, no. 8, pp. 2460–2465, 2000.
- [24] X. Y. Zhao, Y. J. Zhu, F. Chen, B. Q. Lu, and J. Wu, "Nanosheet-assembled hierarchical nanostructures of hydroxyapatite: surfactant-free microwave hydrothermal rapid synthesis, protein/DNA adsorption and pH-controlled release," *Crystal Engineering Communications*, vol. 15, no. 1, pp. 206–212, 2013.
- [25] Z. Li, Y. Xiong, and Y. Xie, "Selected-control synthesis of ZnO nanowires and nanorods via a PEG-assisted route," *Inorganic Chemistry*, vol. 42, no. 24, pp. 8105–8109, 2003.
- [26] C. V. Krishnan, J. Chen, C. Burger, and B. Chu, "Polymer-assisted growth of molybdenum oxide whiskers via a sonochemical process," *Journal of Physical Chemistry B*, vol. 110, no. 41, pp. 20182–20188, 2006.
- [27] G. Xiong, X. Wang, L. Lu, X. Yang, and Y. Xu, "Preparation and characterization of Al₂O₃-TiO₂ composite oxide nanocrystals," *Journal of Solid State Chemistry*, vol. 141, no. 1, pp. 70–77, 1998.
- [28] Y.-H. Tseng, C.-S. Kuo, Y.-Y. Li, and C.-P. Huang, "Polymer-assisted synthesis of hydroxyapatite nanoparticle," *Materials Science and Engineering C*, vol. 29, no. 3, pp. 819–822, 2009.
- [29] J. Zhang, H. Liu, Z. Wang, N. Ming, Z. Li, and A. S. Biris, "Polyvinylpyrrolidone-directed crystallization of ZnO with tunable morphology and bandgap," *Advanced Functional Materials*, vol. 17, no. 18, pp. 3897–3905, 2007.
- [30] S.-H. Jeon, P. Xu, B. Zhang et al., "Polymer-assisted preparation of metal nanoparticles with controlled size and morphology," *Journal of Materials Chemistry*, vol. 21, no. 8, pp. 2550–2554, 2011.
- [31] Y. Peng, A.-W. Xu, B. Deng, M. Antonietti, and H. Cölfen, "Polymer-controlled crystallization of zinc oxide hexagonal nanorings and disks," *Journal of Physical Chemistry B*, vol. 110, no. 7, pp. 2988–2993, 2006.
- [32] A. J. Nathanael, D. Mangalaraj, Y. Masuda, and N. Ponpandian, "Influence of fluorine substitution on the morphology and structure of hydroxyapatite nanocrystals prepared by hydrothermal method," *Materials Chemistry and Physics*, vol. 137, no. 3, pp. 967–976, 2013.

Research Article

Preparation of CaO-SiO₂ Glass-Ceramic Spheres by Electro spraying Combined with Sol-Gel Method

Hiroataka Maeda,¹ Yuki Nakano,² and Toshihiro Kasuga²

¹ Center for Fostering Young and Innovative Researchers, Nagoya Institute of Technology, Gokiso-cho, Showa-ku, Nagoya 466-8555, Japan

² Department of Frontier Materials, Nagoya Institute of Technology, Gokiso-cho, Showa-ku, Nagoya 466-8555, Japan

Correspondence should be addressed to Hiroataka Maeda; maeda.hiroataka@nitech.ac.jp

Received 12 April 2013; Revised 4 June 2013; Accepted 11 June 2013

Academic Editor: Eng San Thian

Copyright © 2013 Hiroataka Maeda et al. This is an open access article distributed under the Creative Commons Attribution License, which permits unrestricted use, distribution, and reproduction in any medium, provided the original work is properly cited.

CaO-SiO₂ glass-ceramic spheres were prepared by an electro spray method using hydrolyzed silicon alkoxide containing calcium nitrate. Crystalline calcium silicates, such as Ca₂SiO₄ and β-CaSiO₃, formed around the surface of the spheres after heat treatment. The dissolution of the crystal phase of the spheres caused the release of Ca²⁺ and Si⁴⁺ ions during the initial stage of soaking in Tris-buffer solution, leading to the formation of nanosized pores at the sphere surface. The incorporation of Ca²⁺ ions into the glassy phase of the spheres suppressed the rapid pH increase during the initial stage of soaking in Tris-buffer solution.

1. Introduction

Recently, interest has arisen in the biomaterials field in a new approach that considers the biological interaction between synthetic materials and cells [1–3]. Silicate and calcium ions released from Bioglass were reported to stimulate bone formation on the material via gene activation [4]. One important strategy for rapid regeneration of bone is to deliver and release these ions into bone defects. Calcium silicates are thought to be potential carriers for these ions. In general, crystalline calcium silicates, such as wollastonite (CaSiO₃), show high degradability [5]. However, they also show a tendency to increase in alkalinity due to their dissolution, resulting in the induction of an inflammatory reaction at an early stage after implantation. Therefore, the dissolution behavior of crystalline calcium silicates must be controlled. To improve their chemical instability, the substitution of other elements, such as strontium and zinc, into their structure has been proposed in combination with calcium phosphates such as hydroxyapatite and tricalcium phosphate, which exhibit slower degradability [6–8].

Bioactive glasses based on CaO-SiO₂ systems have a great potential as materials for bone regeneration because they bond to bone and are osteoinductive [9]. Sol-gel-derived

bioactive glasses have been reported to improve bioactivity, as compared to melt-derived glasses with the same composition [10, 11]. For chemical instability of calcium silicates, our material design is to prepare CaO-SiO₂ glass-ceramics, which contain crystalline calcium silicate ceramics as an ion-releasing component in a glass phase with a silica-based network as a matrix. In the case of CaO-SiO₂ glass derived from sol-gel method, calcination at 700°C has been reported to lead to the stabilization of the silica network [12]. The heat treatment at a high temperature plays an important role in the improvement of its chemical stability for the matrix.

We believe that CaO-SiO₂ glass-ceramic particles are applicable as fillers in injectable bone substitutes for releasing silicate and calcium ions and inducing bioactivity. The fillers should show a narrow distribution of diameter size and should simultaneously be highly dispersed within the materials. That is, monodisperse sphere shapes are needed for use as fillers. It is well known that the electro spray method can be used to synthesize polymer spheres with monodispersity [13, 14]. Polymer solution dissolved in an organic solvent is pressed using a syringe under a high voltage, resulting in the formation of spheres with diameters in the range of nanometers to micrometers owing to the intertwining of polymer chains. We have previously succeeded in preparing

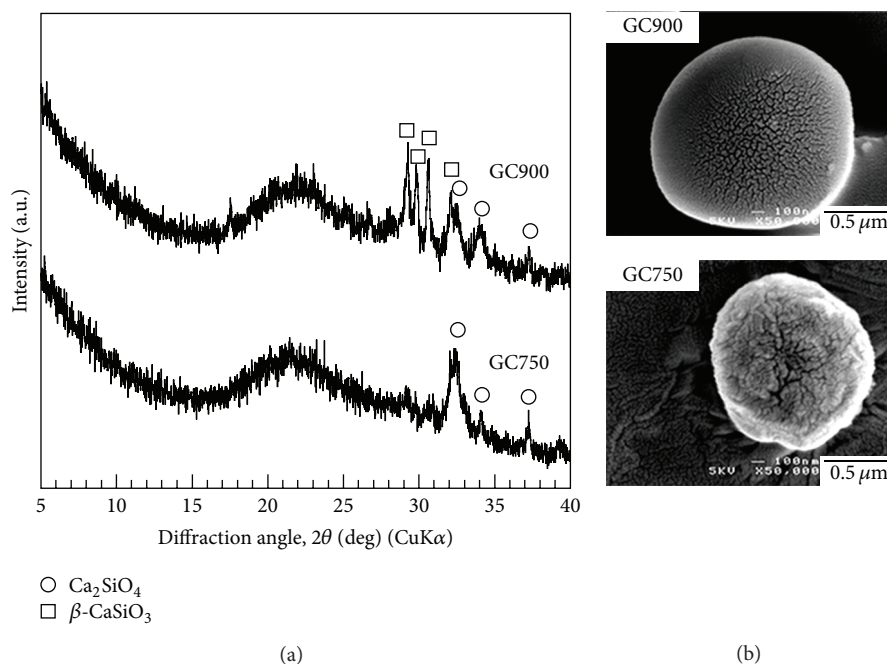


FIGURE 1: XRD patterns (a) and SEM micrographs (b) for GC750 and GC900 spheres.

porous spheres containing a large amount of CaSiO_3 with monodispersity using electrospraying combined with the sol-gel method [15].

In the present work, sol-gel-derived glass spheres (80 mol% SiO_2 and 20 mol% CaO as a starting chemical composition) were prepared by electrospray method using a hydrolyzed alkoxide. In general, the sintering temperature of the ceramic precursor with a CaO-SiO_2 system derived from the sol-gel method leads to the formation of a separate crystalline phase [16]. CaO-SiO_2 gel spheres were heat treated at different temperatures to investigate release of inorganic ions with biological effects and suppression for the rapid pH increase during the initial stage of soaking in Tris-buffer solution.

2. Materials and Methods

Tetraethylorthosilicate (TEOS), ethanol, and distilled water (DW) were used as starting materials. Nitric acid acted as an acid catalyst. The molar ratio of TEOS/ethanol/DW/nitric acid was 1:2:4:0.05. Calcium nitrate tetrahydrate was used as a calcium source. The molar ratio of Ca/Si was 1:4. After aging for 12 h at 35°C , the precursor solution of hydrolyzed TEOS containing calcium ions was electrosprayed to prepare gel spheres. The electrospraying system was constructed using a substrate holder, a stainless steel capillary tube (22 gauge), a precursor solution tank, and a high voltage source. The applied voltage was 20 kV. The distance between the substrate and the tip of the capillary tube was 150 mm. The resulting spheres were dried in air at 80°C for 24 h and subsequently stored in a desiccator. Calcination at $550\text{--}600^\circ\text{C}$ is necessary to remove nitrates [17]. The spheres were heated

at 750 or 900°C for 1 h for crystallization to control the crystal phase. We determined the heat temperature by an optimization process based on a trial-and-error approach to achieve satisfactory results in terms of precipitating different crystal phases in the spheres. The samples prepared at 750 and 900°C of heat treatment are denoted as GC750 and GC900, respectively. The samples were analyzed using X-ray diffractometry (XRD; PANalytical, X'pert-MPD) using $\text{CuK}\alpha$ radiation, operating at 45 kV, 40 mA. The samples were coated with amorphous osmium by plasma chemical vapor deposition and then observed by scanning electron microscopy (SEM; JEOL, JSM-6301F) with 5 kV of acceleration voltage. The sphere diameter was measured for at least 200 points by image-editing software: ImageJ, obtained from National Institutes of Health. The concentrations of ions released from the spheres while soaking in Tris-buffer solution containing 50 mmol/L $(\text{CH}_2\text{OH})_3\text{CNH}_2$ and 45 mmol/L HCl at pH 7.5 at 36.5°C in a polypropylene beaker were determined by inductively coupled plasma atomic emission spectroscopy (ICP-AES; Shimadzu, ICPS-7000). The dissolution test was performed using a spheres/Tris-buffer solution ratio of 1:1. At least three tests were evaluated for ion concentrations and pH in Tris-buffer solution after soaking of the samples. A statistical analysis was performed by *t*-test.

3. Results and Discussion

3.1. Crystal Phases and Morphologies of the CaO-SiO_2 Glass-Ceramic Spheres. Figure 1 shows the XRD patterns and SEM micrographs of GC750 and 900 spheres. The XRD pattern for GC750 spheres showed sharp peaks at around

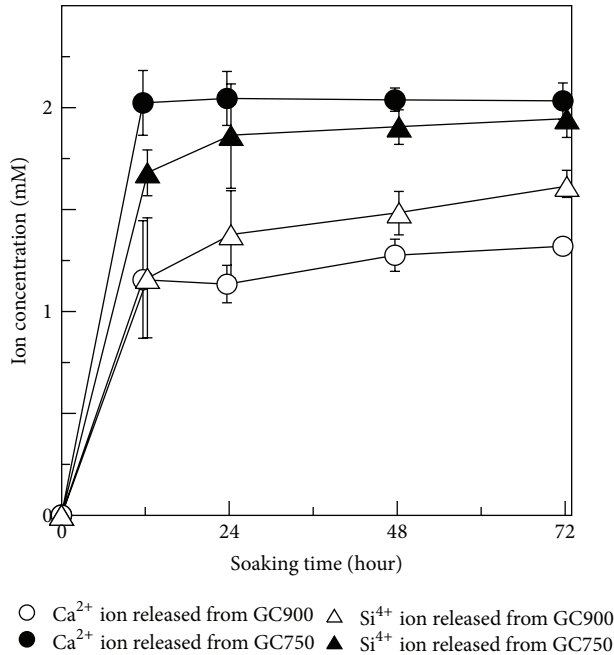


FIGURE 2: The concentrations of Ca^{2+} (circle) and Si^{4+} (triangle) ions released from GC750 (closed marks) and GC900 (open marks) spheres after soaking.

32, 34, and 37° corresponding to Ca_2SiO_4 (number 83-0461) and a halo peak at around 22° corresponding to an amorphous phase. In the XRD pattern for GC900 spheres, new peaks at around 27, 28, and 29° corresponding to $\beta\text{-CaSiO}_3$ (number 84-0655) were seen with peaks corresponding to Ca_2SiO_4 and an amorphous phase. It has been already reported that $\beta\text{-CaSiO}_3$ is synthesized by heat treatment of gel-derived materials at 1000°C using TEOS and hydrated calcium nitrate as starting materials in a solvent of diluted nitric acid or sodium hydroxide solution [18], which agrees with the results of the present work. It was clearly seen in both micrographs that bright and dark portions originate from crystalline and amorphous phases in these samples, respectively. The diameters of the GC750 and GC900 spheres were determined to be 0.6–1.2 μm (average $0.9 \pm 0.2 \mu\text{m}$) and 0.7–1.2 μm (average $0.9 \pm 0.1 \mu\text{m}$), respectively, in SEM micrographs, independent of the heating temperature.

3.2. Dissolution Tests of the CaO-SiO_2 Glass-Ceramic Spheres in Tris-Buffer Solution. Figure 2 shows the concentrations of Ca^{2+} and Si^{4+} ions released from the spheres after soaking in Tris-buffer solution for various time periods. After soaking of GC750, the concentration of Ca^{2+} ions increased dramatically during the first 12 h and then stabilized. In the case of GC900 spheres, the concentration of Ca^{2+} ions increased dramatically during the first 12 h and then kept increasing gradually. The concentration of Ca^{2+} ions released from GC750 spheres was higher than that from GC900 spheres.

By contrast, the amount of Si^{4+} ions released into the Tris-buffer solution increased rapidly during the first 12 h and then tended to increase gradually. The concentration of Si^{4+} ions released from GC750 spheres into Tris-buffer solution was lower than that from GC900 spheres.

Figure 3 shows the XRD patterns and SEM micrographs for GC750 and GC900 spheres after 72 h of soaking in Tris-buffer solution. In both XRD pattern for GC750 and GC900 spheres, no peaks corresponding to a crystalline phase were observed. Ions released from the samples should be composed predominantly of crystalline calcium silicates. The difference in crystalline phase between the samples depends on the ratio of $\text{Ca}^{2+}/\text{Si}^{4+}$ ions release. Pores that are several tens of nanometers in diameter can be seen at the surfaces of both samples as shown in Figure 3(b). The formation of pores is attributed to dissolution of the crystalline phase of the samples during soaking. This finding implies that surface crystallization at nanometer sizes occurred under these experimental conditions. The diameters of the GC750 and GC900 spheres after the soaking were determined to be 0.6–1.2 μm (average $0.9 \pm 0.2 \mu\text{m}$) and 0.7–1.2 μm (average $1.0 \pm 0.1 \mu\text{m}$), respectively, in SEM micrographs. There was no significant change in the diameter even after the soaking.

The ion-releasing ratios, which were calculated from the amounts of both ions in the Tris-buffer solution divided by the total amounts of both ions in the samples were estimated to be approximately 60% and 10 ~ 15% for Ca^{2+} and Si^{4+} , respectively. After calcination, some Ca^{2+} ions in the gel derived from the sol-gel process were reported to be incorporated into the disordered glassy structure comprising a silica-based network [19]. The remaining Ca^{2+} ions are proposed to be released gradually with the dissolution of the silica network over a long period.

Figure 4 shows the change in pH of the Tris-buffer solution after soaking of GC750 or GC900 spheres. The pH behavior showed a similar trend for both samples. The pH increased slightly to 7.6 during the first 24 h of soaking and subsequently showed almost constant value without statistical difference. Ca^{2+} ions released from the samples led to an increase in pH of the Tris-buffer solution. The incorporation of Ca^{2+} ions into the amorphous phase of the CaO-SiO_2 -based glass-ceramics plays an important role in suppressing the pH increase during the initial stage. We propose that CaO-SiO_2 glass-ceramic spheres are preferred for use as filler materials in injectable bone substitutes for releasing silicate and calcium ions over time.

4. Conclusion

Silica-based glass-ceramic spheres containing crystalline calcium silicates were prepared by electrospraying combined with the sol-gel method. The calcium silicates formed selectivity at the surface. Ca^{2+} and Si^{4+} ions were released predominantly from the crystal phase of the spheres. The existence of a glassy phase and incorporation of Ca^{2+} ions into the glassy phase suppressed the rapid pH increase during soaking of the spheres in solution. Investigation on the biological effects of the spheres is now in progress.

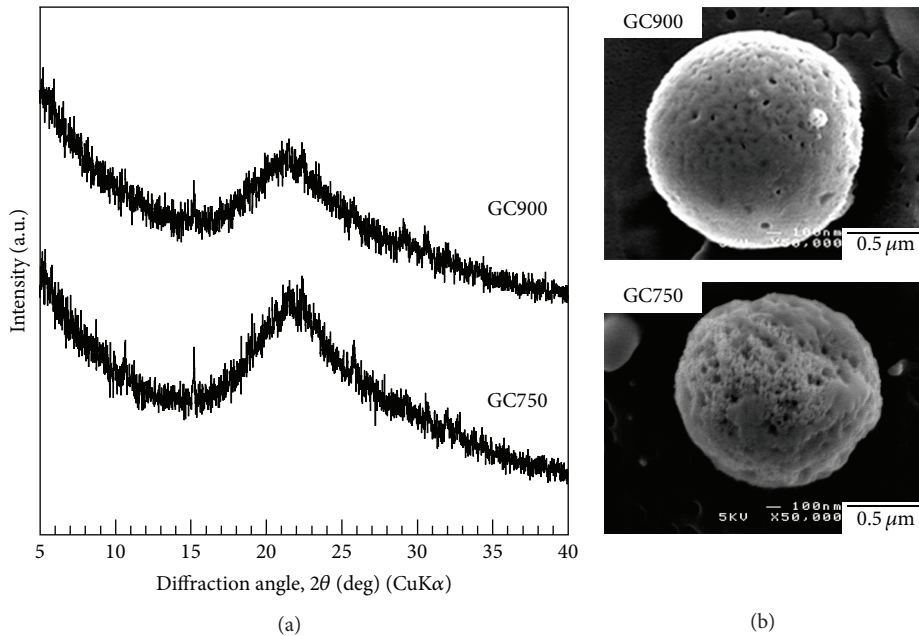


FIGURE 3: XRD patterns (a) and SEM micrographs (b) for GC750 and GC900 spheres after 72 h of soaking.

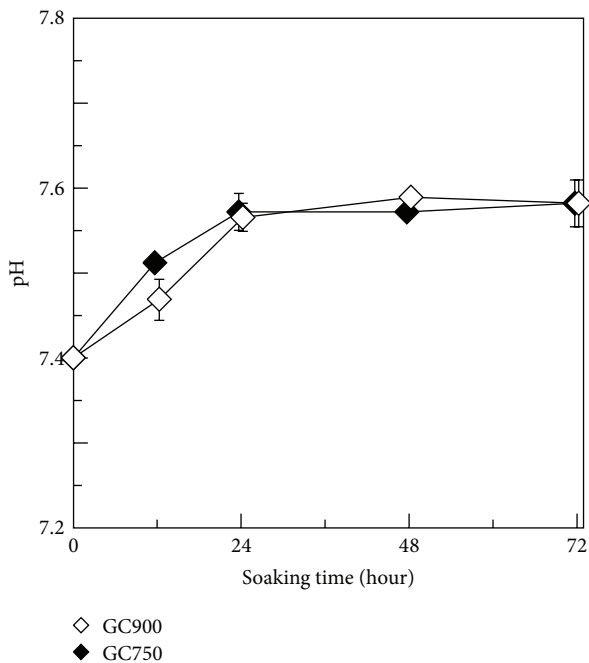


FIGURE 4: pH change in Tris-buffer solution after soaking of GC750 and GC900 spheres.

Conflict of Interests

The authors certify that there is no conflict of interests with any financial organization regarding the material disused in the paper.

Acknowledgments

This work was partially supported by a Grant-in-Aid for Scientific Research on Innovative Areas (no. 24120005) and the Institute of Ceramics Research and Education (ICRE), Nagoya Institute of Technology.

References

- [1] A. Hoppe, N. S. Gldal, and A. R. Boccaccini, "A review of the biological response to ionic dissolution products from bioactive glasses and glass-ceramics," *Biomaterials*, vol. 32, no. 11, pp. 2757–2774, 2011.
- [2] J. R. Jones, O. Tsigkou, E. E. Coates, M. M. Stevens, J. M. Polak, and L. L. Hench, "Extracellular matrix formation and mineralization on a phosphate-free porous bioactive glass scaffold using primary human osteoblast (HOB) cells," *Biomaterials*, vol. 28, no. 9, pp. 1653–1663, 2007.
- [3] M.-Y. Shie, S.-J. Ding, and H.-C. Chang, "The role of silicon in osteoblast-like cell proliferation and apoptosis," *Acta Biomaterialia*, vol. 7, no. 6, pp. 2604–2614, 2011.
- [4] I. D. Xynos, A. J. Edgar, L. D. K. Buttery, L. L. Hench, and J. M. Polak, "Ionic products of bioactive glass dissolution increase proliferation of human osteoblasts and induce insulin-like growth factor II mRNA expression and protein synthesis," *Biochemical and Biophysical Research Communications*, vol. 276, no. 2, pp. 461–465, 2000.
- [5] S. Ni, J. Chang, and L. Chou, "A novel bioactive porous CaSiO₃ scaffold for bone tissue engineering," *Journal of Biomedical Materials Research A*, vol. 76, no. 1, pp. 196–205, 2006.
- [6] H. Zreiqat, Y. Ramaswamy, C. Wu et al., "The incorporation of strontium and zinc into a calcium-silicon ceramic for bone

- tissue engineering,” *Biomaterials*, vol. 31, no. 12, pp. 3175–3184, 2010.
- [7] F. Zhang, J. Chang, K. Lin, and J. Lu, “Preparation, mechanical properties and in vitro degradability of wollastonite/tricalcium phosphate macroporous scaffolds from nanocomposite powders,” *Journal of Materials Science*, vol. 19, no. 1, pp. 167–173, 2008.
- [8] H. Du, Z. Wei, H. Wang, E. Zhang, L. Zuo, and L. Du, “Surface microstructure and cell compatibility of calcium silicate and calcium phosphate composite coatings on Mg-Zn-Mn-Ca alloys for biomedical application,” *Colloids and Surfaces B*, vol. 83, no. 1, pp. 96–102, 2011.
- [9] L. L. Hench, “Bioceramics,” *Journal of the American Ceramic Society*, vol. 81, no. 7, pp. 1705–1727, 1998.
- [10] P. Sepulveda, J. R. Jones, and L. L. Hench, “Characterization of melt-derived 45S5 and sol-gel-derived 58S bioactive glasses,” *Journal of Biomedical Materials Research*, vol. 58, no. 6, pp. 734–740, 2001.
- [11] H. Maeda, T. Okuyama, E. H. Ishida, and T. Kasuga, “Preparation of porous spheres containing wollastonite by an electro-spray method,” *Materials Letters*, vol. 95, pp. 107–109, 2013.
- [12] S. Lin, C. Ionescu, K. J. Pike, M. E. Smith, and J. R. Jones, “Nanostructure evolution and calcium distribution in sol-gel derived bioactive glass,” *Journal of Materials Chemistry*, vol. 19, no. 9, pp. 1276–1282, 2009.
- [13] D. Fantini, M. Zanetti, and L. Costa, “Polystyrene microspheres and nanospheres produced by electrospray,” *Macromolecular Rapid Communications*, vol. 27, no. 23, pp. 2038–2042, 2006.
- [14] A. Gomez, D. Bingham, L. De Juan, and K. Tang, “Production of protein nanoparticles by electrospray drying,” *Journal of Aerosol Science*, vol. 29, no. 5-6, pp. 561–574, 1998.
- [15] S. Labbaf, O. Tsigkou, K. H. Müller, M. M. Stevens, A. E. Porter, and J. R. Jones, “Spherical bioactive glass particles and their interaction with human mesenchymal stem cells in vitro,” *Biomaterials*, vol. 32, no. 4, pp. 1010–1018, 2011.
- [16] M. A. de La Casa-Lillo, P. Velásquez, and P. N. De Aza, “Influence of thermal treatment on the “in vitro” bioactivity of wollastonite materials,” *Journal of Materials Science*, vol. 22, no. 4, pp. 907–915, 2011.
- [17] J. R. Jones, L. M. Ehrenfried, and L. L. Hench, “Optimising bioactive glass scaffolds for bone tissue engineering,” *Biomaterials*, vol. 27, no. 7, pp. 964–973, 2006.
- [18] P. Siriphannon, Y. Kameshima, A. Yasumori, K. Okada, and S. Hayashi, “Formation of hydroxyapatite on CaSiO₃ powders in simulated body fluid,” *Journal of the European Ceramic Society*, vol. 22, no. 4, pp. 511–520, 2002.
- [19] G. M. Luz and J. F. Mano, “Nanoengineering of bioactive glasses: hollow and dense nanospheres,” *Journal of Nanoparticle Research*, vol. 15, no. 1457, 11 pages, 2013.

Research Article

Preparation and *In Vitro* and *In Vivo* Performance of Magnesium Ion Substituted Biphasic Calcium Phosphate Spherical Microscaffolds as Human Adipose Tissue-Derived Mesenchymal Stem Cell Microcarriers

Dong-Hyun Kim,¹ Tae-Wan Kim,¹ Ju Dong Lee,² Keun-Koo Shin,³ Jin Sup Jung,³ Kyu-Hong Hwang,⁴ Jong Kook Lee,⁵ Hong-Chae Park,¹ and Seog-Young Yoon¹

¹ School of Materials Science and Engineering, Pusan National University, Busan 609-735, Republic of Korea

² Korea Institutes of Industrial Technology, Busan 618-230, Republic of Korea

³ Department of Physiology, School of Medicine, Pusan National University, Yangsan 626-770, Republic of Korea

⁴ School of Nano and Advanced Materials, Gyeongsang National University, Jinju 660-701, Republic of Korea

⁵ Department of Advanced Materials Engineering, Chosun University, Gwangju 501-759, Republic of Korea

Correspondence should be addressed to Seog-Young Yoon; syy3@pusan.ac.kr

Received 17 April 2013; Accepted 16 May 2013

Academic Editor: Eng San Thian

Copyright © 2013 Dong-Hyun Kim et al. This is an open access article distributed under the Creative Commons Attribution License, which permits unrestricted use, distribution, and reproduction in any medium, provided the original work is properly cited.

Magnesium ion substituted biphasic calcium phosphate (Mg-BCP) bioceramic microscaffolds with spherical and porous morphology were successfully prepared using *in situ* coprecipitation and rotary spray drying atomization process for application of tissue engineering combined with human adipose tissue-derived mesenchymal stem cells (hAT-MSCs). After 4 weeks of immersion in Hanks' balanced salt solution (HBSS), Mg-BCP micro-scaffolds showed the enhanced biodegradation and bioactivity due to the substituted Mg²⁺ ion present in the BCP structure. In this study, it was observed that hAT-MSCs have clearly attached on the surface of Mg-BCP micro-scaffolds. In addition, Mg-BCP micro-scaffolds exhibited the improved biocompatibility and osteoconductivity via *in vitro* and *in vivo* biological tests with hAT-MSCs. Therefore, these bioceramic micro-scaffolds had potential to be used as hAT-MSCs microcarriers for biomedical applications.

1. Introduction

Microsized calcium phosphate (CP) spherical bioceramic granules have gained great interest for use as bone grafting cement materials in non-load-bearing situation which means a better filling of an irregular defect and high packing into damaged bone tissues. The main reason is that the bioresorption rate of porous granules could be predicted to be faster than dense blocks made of the same material [1–3]. In addition, uniformly packed spheres with homogenous pore distribution have been reported to increase the rate of bone ingrowth [4]. Tamimi et al. reported that the application of monetite bioceramic granules showed faster resorption and increased bone neof ormation when compared with

commercial apatite granules from animal source [5]. Paul et al. reported hydroxyapatite ceramic microspheres for use as delivery of insulin [6]. Labbaf et al. reported the interaction between spherical bioactive glass particles and human mesenchymal stem cells [7]. For that reason, spherical CP microgranules can be used either as bone grafting materials, or as carriers for drugs or cells [8–10]. Recently, one of the CP materials in bone grafting bioceramics, biphasic calcium phosphates (BCPs, HAp/ β -TCP), has focused on studies for multiphase control and effects of ionic substitutions in order to optimize bioresorbability and bioactivity [11–14]. For example, Mg²⁺ ion-substituted CPs have been reported to enhance bioresorbability and bioactivity during the early stages of osteogenesis where they stimulate osteoblast

proliferation [15, 16]. According to our previous study, it was also shown that the appropriate substitutions of Mg^{2+} ions in BCP powder could accelerate the formation of biological new apatite than pure BCP [17].

Stem cells in bone tissue engineering are also one of the most promising alternatives for existing treatment modalities for bone defects because they could be osteogenic differentiated under *in vitro* and *in vivo* condition. However, they are not subject to supply limitations due to their self-renewal capacity [18]. In addition, the application of embryonic stem cells is strictly limited due to ethical and political issues. In order to solve such complex problems, there have been many recent reports on success of isolating stem cells and osteogenic differentiated from human, rat, rabbit, and mouse adipose tissue sources [19–22].

Most models of bone-tissue scaffold engineering are based on seeding mesenchymal stem cells (MSCs) onto biodegradable and biocompatible three-dimensional (3D) bulk scaffolds like biopolymers, ceramics, and composites. However, 3D scaffolds are very difficult to apply to combining and seeding MSCs inside pore spacing without control of large open pore size (100–500 μm) in bone-tissue engineering. Therefore, usability viewpoint of MSCs could bring out the scaffold application of new concept [23–25]. Here, we describe for the first time the successful formation of mineralized bone tissue by the combination of Mg^{2+} ion-substituted biphasic calcium phosphate (Mg-BCP) spherical microscaffolds and human adipose tissue-derived mesenchymal stem cells (hAT-MSCs). In addition, the purpose of this study is an approach of systematic bio-fusion method which means that human adipose tissue-derived mesenchymal stem cells (hAT-MSCs) could be cell-attached and osteogenic differentiated around Mg^{2+} ion-substituted biphasic calcium phosphate (Mg-BCP) micro-scaffold *in vitro*. Possibilities of hAT-MSC microcarrier and bone graft application for spherical Mg-BCP microscaffolds have also been investigated by an *in vivo* model.

2. Materials and Methods

2.1. Fabrication of Spherical Mg-BCP Microscaffolds. In order to prepare Mg-BCP microscaffolds, all processes were modified from our previous works [17]. Firstly, an appropriate amount (Mg/Ca molar ratio 0.01) of calcium nitrate tetrahydrate ($\text{Ca}(\text{NO}_3)_2 \cdot 4\text{H}_2\text{O}$) and magnesium nitrate hexahydrate ($\text{Mg}(\text{NO}_3)_2 \cdot 6\text{H}_2\text{O}$) was dissolved in distilled water by vigorously stirring at a rate of 1000 rpm. Diammonium hydrogen phosphate ($(\text{NH}_4)_2\text{-HPO}_4$) solution was slowly added to the mixed solution of the calcium nitrate tetrahydrate and magnesium nitrate hexahydrate in order to obtain a nominal composition in terms of (Ca + Mg)/P ratio 1.602. The pH of the mixed solution was maintained at 11 by the addition of ammonium hydroxide (NH_4OH) solution. The coprecipitated suspension was discharged from the reactor and allowed to settle for 24 h for the maturation of precipitate. After 24 h, the precipitates were separated through vacuum filtration technique and dried at 80°C for 24 h in a drying oven.

To obtain the slurries of Mg-BCP, binder, dispersants and defoamer were used as organic additives and Mg-BCP

precursor powders were slowly added into the organic additive solution via continuous attrition milling (400 RPM, 4 h). The as-prepared slurries were spray-dried with a rotary atomizer system. The spray-dried samples were placed in an alumina crucible and calcined at 1000°C for 24 h in air. The as-calcined Mg-BCP microscaffolds were sieved for the selection of appropriate sizes ranging from 45–75 μm (mesh nos. 200 and 325).

2.2. Characterization of Spherical Mg-BCP Microscaffolds. An X-ray diffractometer (XRD) at 40 kV and 40 mA with a scanning speed of 0.1°/min was adopted to identify the phases of Mg-BCP microscaffolds and compare them with pure BCPs. Microstructures and chemical compositions of samples were characterized using field emission scanning electron microscope (FE-SEM) and energy dispersive X-ray analyzer (SEM-EDX).

Hanks' balanced salt solution (HBSS), an extracellular solution with an ionic composition similar to human blood plasma, was used as the supporting solution for the Mg-BCP microscaffolds *in vitro* test. The simulated solution consisted of 8.00 g NaCl, 0.35 g NaHCO_3 , 0.40 g KCl, 0.06 g KH_2PO_4 , 0.10 g $\text{MgCl}_2 \cdot 6\text{H}_2\text{O}$, 0.14 g CaCl_2 , 0.06 g $\text{Na}_2\text{HPO}_4 \cdot 2\text{H}_2\text{O}$, 0.06 g $\text{MgSO}_4 \cdot 7\text{H}_2\text{O}$, and 1.00 g glucose in 1000 mL distilled H_2O and had an initial pH of 7.4. Mg-BCP scaffolds were immersed in 50 mL of HBSS without organic species (pH 7.4), at 37°C in Teflon sealed polystyrene bottle for 1, 2, and 4 weeks. After immersing the samples in Hank's solution for 1, 2, and 4 weeks, Mg^{2+} , Ca^{2+} , and PO_4^{3-} concentrations of HBSS were measured using inductively coupled plasma atomic emission spectrometer (ICP-AES). After immersion for 1, 2, and 4 weeks, the scaffolds were rinsed 3 times with double-distilled water to remove residual HBSS and then immediately dried in vacuum desiccators at 21°C. The surface morphologies of the scaffolds before and after immersion in HBSS were analyzed using FE-SEM.

2.3. In Vitro and In Vivo Test of hAT-MSCs with Mg-BCP Microscaffolds. All protocols involving human subjects were approved by the Institutional Review Board of Pusan National University. The human adipose tissue-derived mesenchymal stem cells (hAT-MSCs) were isolated according to the methods described in previous studies [19]. Isolated cells were cultured in α -modified Eagle's medium (α -MEM), containing 10% fetal bovine serum (FBS).

The cells were detached using Hank's balanced salt solution containing 0.05% trypsin and 0.02% ethylenediaminetetraacetic acid (EDTA) to determine the rate of proliferation. The cells were plated on a 6-well plate at a density of 5×10^3 cells/well. MTT assay for 2 mg Mg-BCP microscaffolds was carried out to measure and evaluate cell survival and proliferation of mesenchymal stem cells (MSCs). MTT (3-(4,5-dimethylthiazol-2-yl)-2,5-diphenyltetrazolium bromide) was reduced to purple formazan in living cells. The absorbance of this colored solution could be measured at 560 nm in an ELISA reader. In statistical analysis, all results were presented as the mean standard error of the mean. Comparisons of cell viability between 2 groups of collagen and Mg-BCP were analyzed via Student's *t*-tests. Multiple group comparisons

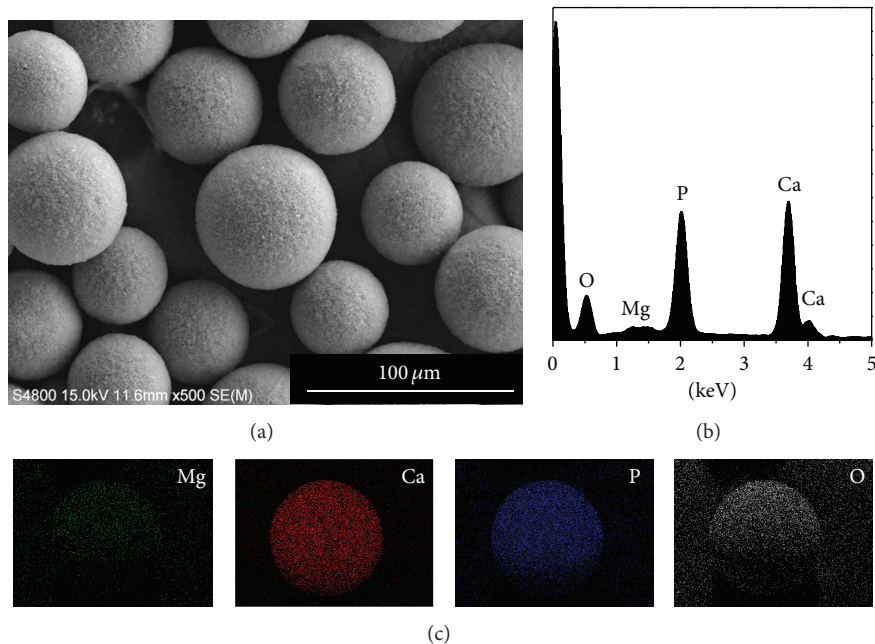


FIGURE 1: (a) FE-SEM micrographs, (b) SEM-EDX spectrum, and EDX mapping results of spherical Mg-BCP microscaffolds.

were conducted by lone-way analysis of variance with Tukey adjustments. P values <0.05 were considered statistically.

Osteogenic differentiation was induced through culturing of the cells for 14 days in osteogenic medium (10% FBS, 0.1 mM dexamethasone, 10 mM β -glycerophosphate, and 50 mM ascorbic acid in α -MEM), and extracellular matrix calcification was estimated using Alizarin Red S stain. Osteogenic differentiation was confirmed through the observation of the Alizarin Red stained area and density in 6-well dishes.

hAT-MSC-attached Mg-BCP scaffolds were evaluated qualitatively *in vivo* using critical-sized calvarial bone defects in adult (6 weeks old) severe combined immunodeficient (SCID) mice. The surgical procedures were performed in aseptic conditions under general anesthesia. Briefly, a linear incision (1 cm long) was made on the left side of the skull and the scalp was dissected to expose the calvaria. The periosteum was carefully peeled off and 2 lateral 4 mm wide calvarial bone defects were performed in each animal using a slow-speed dental drill with a 3 mm diameter trephine bur. To avoid tissue damage due to overheating, 0.9% saline was dripped onto the contact point between the bur and bone and great care was taken to avoid dura mater injury. hAT-MSC-attached Mg-BCP scaffolds were then implanted into one of the defect sites while the contralateral site was implanted with pure hAT-MSCs as a control. The animals were euthanized after 1 and 2 months by exposure to hyperbaric carbon dioxide. At each time point after 1 and 2 months, the skulls were harvested and fixed in 4% paraformaldehyde for 12 h. Calvaria were X-rayed using a volumetric computed tomography (CT) scanner at 50 kVp, 65 μ A, and 470 ms per frame and then decalcified overnight with decalcifying solution (10% EDTA). Samples were then trimmed, processed, and embedded in paraffin wax. A micro-CT image of the mouse calvaria was taken using the CT scanner without changing the position of

the animal's head. Paraffin-embedded samples were sectioned into 10 mm thick slices with a microtome. The surface morphologies of the as-implanted sample were analyzed using FE-SEM and SEM-EDX after *in vivo* test.

3. Results and Discussion

3.1. Mg-BCP Microscaffolds. Figure 1 shows FE-SEM image and SEM-EDX results of the spherical Mg-BCP microscaffolds. As shown in Figure 1(a), Mg-BCP microscaffolds had spherical morphologies after *in situ* coprecipitation, spray drying atomization, and calcination process. Result of SEM-EDX spectrum showed that Mg-BCP microscaffolds were mainly composed of Ca, P, O, and Mg atoms (Figure 1(b)). In addition, EDX mapping indicated that Mg atoms were uniformly spread out with the calcium phosphate elements (Figure 1(c)).

XRD patterns for as-synthesized spherical BCP and Mg-BCP microscaffolds are presented in Figure 2. As can be seen in Figure 2, all the obtained microscaffolds had both the β -TCP (JCPDS PDF no. 09-169) and HAp (JCPDS PDF no. 09-432) phase confirming the formation of biphasic mixtures. However, there is a difference in diffraction intensities of the peaks assigned to the β -TCP phase in Mg-BCPs compared to pure BCPs. These results could suggest that Mg^{2+} ions were preferentially incorporated into the β -TCP phase, replacing of Ca^{2+} ion (ionic radius ~ 0.99 Å) by Mg^{2+} ion (ionic radius ~ 0.65 Å), inducing a lattice contraction and respective displacement of the β -TCP reflections toward higher 2θ angles, as mentioned in the literature [26].

3.2. In Vitro Biodegradation and Bioactivity of Mg-BCP Microscaffolds in HBSS. Figure 3 shows the typical surface features of Mg-BCP microscaffolds after immersing in HBSS for 0,

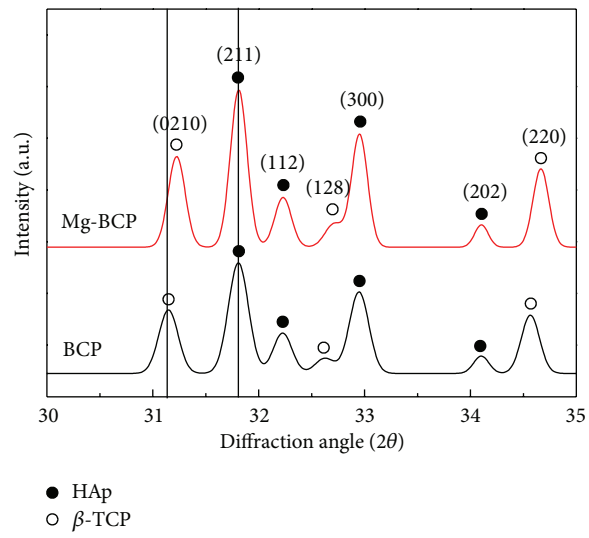


FIGURE 2: XRD patterns (●: HAp, JCPDS PDF no. 09-432, ○: β -TCP, JCPDS PDF no. 09-169) of spherical Mg-BCP microscaffolds.

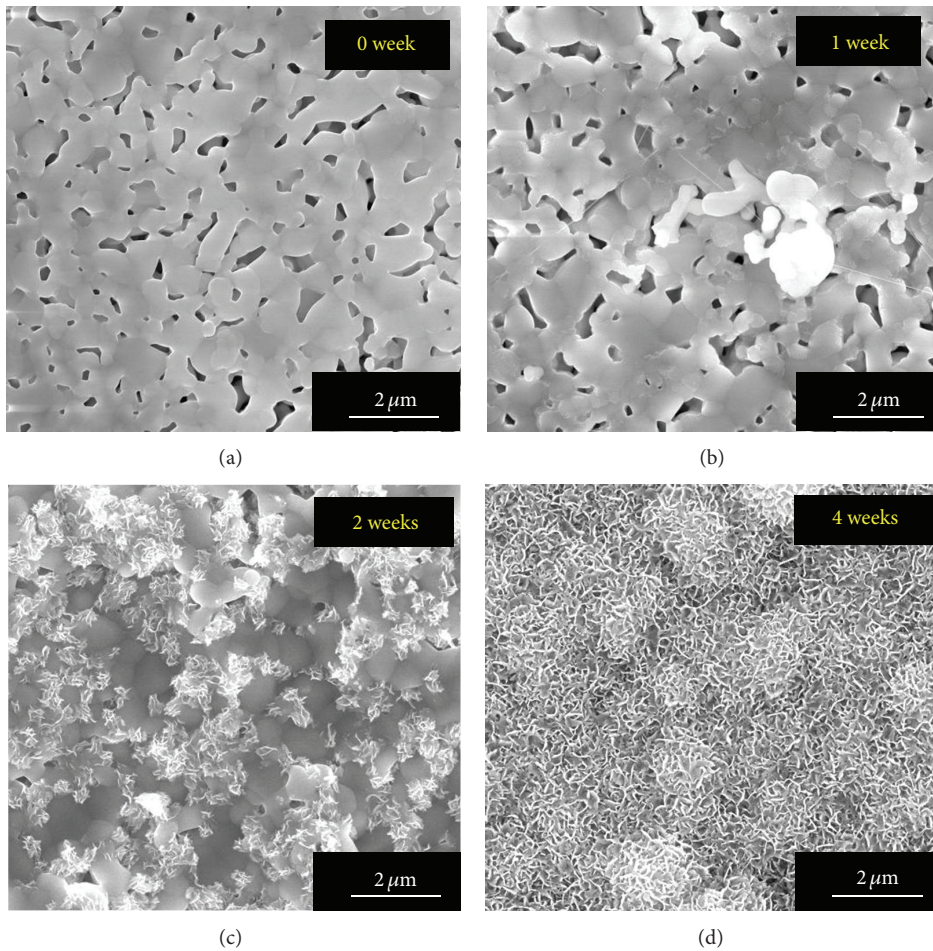


FIGURE 3: Surface morphologies of Mg-BCP microscaffolds after immersed in HBSS: (a) 0, (b) 1, (c) 2, and (d) 4 weeks.

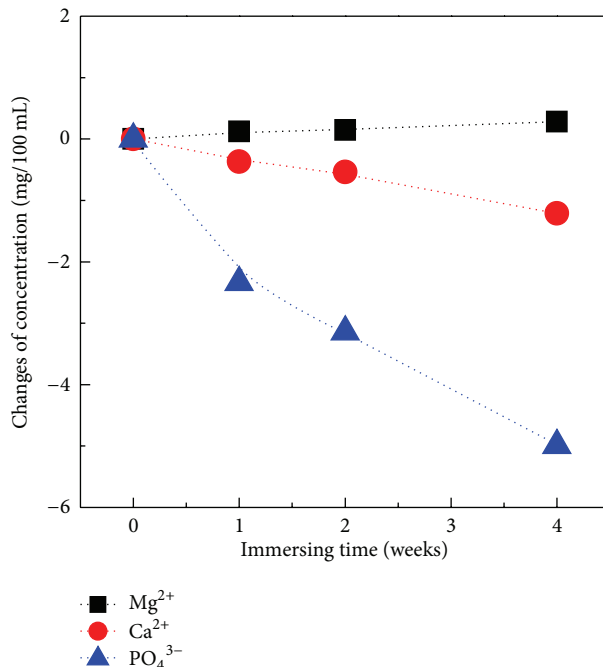


FIGURE 4: Change of Mg²⁺, Ca²⁺, and PO₄³⁻ ion concentrations in HBSS immersed with Mg-BCP microscaffolds during 4 weeks.

1, 2, and 4 weeks, respectively. As can be seen in Figure 3(a), the surface morphology of Mg-BCP microscaffolds showed primary particle-interconnected structure with micropores. The Mg-BCP microscaffolds were partially degraded during immersion in HBSS after 1 and 2 weeks (Figures 3(b) and 3(c)). The Mg-BCP microscaffolds, shown in Figure 3(d) were formed with individual flake-like nanocrystalline calcium deficient apatite (CDA) after 4 weeks.

The ICP-AES analysis reveals the changes of Mg²⁺, Ca²⁺, and PO₄³⁻ concentrations in HBSS after immersing the Mg-BCP microscaffolds, as shown in Figure 4. The Mg²⁺ ions were slowly released with increasing immersion time, which indicated that the Mg²⁺ ions were released from the β -TCP phase in Mg-BCP. On the other hand, the concentration of Ca²⁺ and PO₄³⁻ ions in HBSS continually decreased with increasing immersion time, suggesting that the decrease in concentration of Ca²⁺ and PO₄³⁻ ions might be a result of the formation of new CDA.

3.3. In Vitro Proliferation and Osteogenic Differentiation of hAT-MSCs with Mg-BCP Microscaffolds. Figure 5 shows *in vitro* biological properties of Mg-BCP microscaffolds related to hAT-MSCs. As can be seen in Figure 5(a), hAT-MSCs spread out around the surface of Mg-BCP microscaffolds, demonstrating the biocompatibility of Mg-BCP microscaffolds and had elongated phenotype for 3 days. Thus, cell attachment behaviors on the surface of Mg-BCP microscaffolds showed good biocompatibility indicated of hAT-MSCs growth and proliferation for 7 and 14 days, respectively. From the SEM image as shown in Figure 5(b), it was also observed that hAT-MSCs had clearly attached on the surface

of Mg-BCP microscaffolds. Such behaviors might be caused to existence of blast related to hAT-MSCs in pores of Mg-BCP microscaffolds (Figure 5(c)). Cell viability results in Figure 5(d) indicated that Mg-BCP microscaffolds had no cytotoxic effects on hAT-MSCs and have good biocompatibility, which are consistent with the results presented in Figures 5(a), 5(b), and 5(c). In the osteoconductivity evaluation, hAT-MSCs with Mg-BCP microscaffolds showed enhanced osteogenic cell differentiation (Alizarin Red staining area was the osteogenic cell differentiation of hAT-MSCs) compared to pure hAT-MSCs as shown in Figure 6(a). From optical microscopy imaging as shown in Figure 6(b), it was also observed that osteogenic differentiated-hAT-MSCs have clearly attached on the surface of Mg-BCP microscaffolds.

3.4. In Vivo Test in Bone Defects of SCID Mice. In biological osteoconductivity evaluation of Mg-BCP microscaffolds via *in vivo* test, new bone generation behavior within the oval bone defects of SCID mice showed extreme difference in results between the two types of implant material. As shown in Figure 7, after 2 months *in vivo*, micro-CT images of sites implanted with hAT-MSCs containing Mg-BCP microscaffolds showed relative high-dense area due to new bone mineralization whereas the area implanted with pure hAT-MSCs had no new bone mineralization. Figure 8 shows FE-SEM image and SEM-EDX results of hAT-MSCs/Mg-BCP-implanted sample after 2 months. As shown in Figure 8(a), Mg-BCP micro-scaffold maintained its spherical morphology after the *in vivo* test and small particles were noted on the surface of the as-implanted sample due to the formation of new bone around the scaffold. In addition, result of

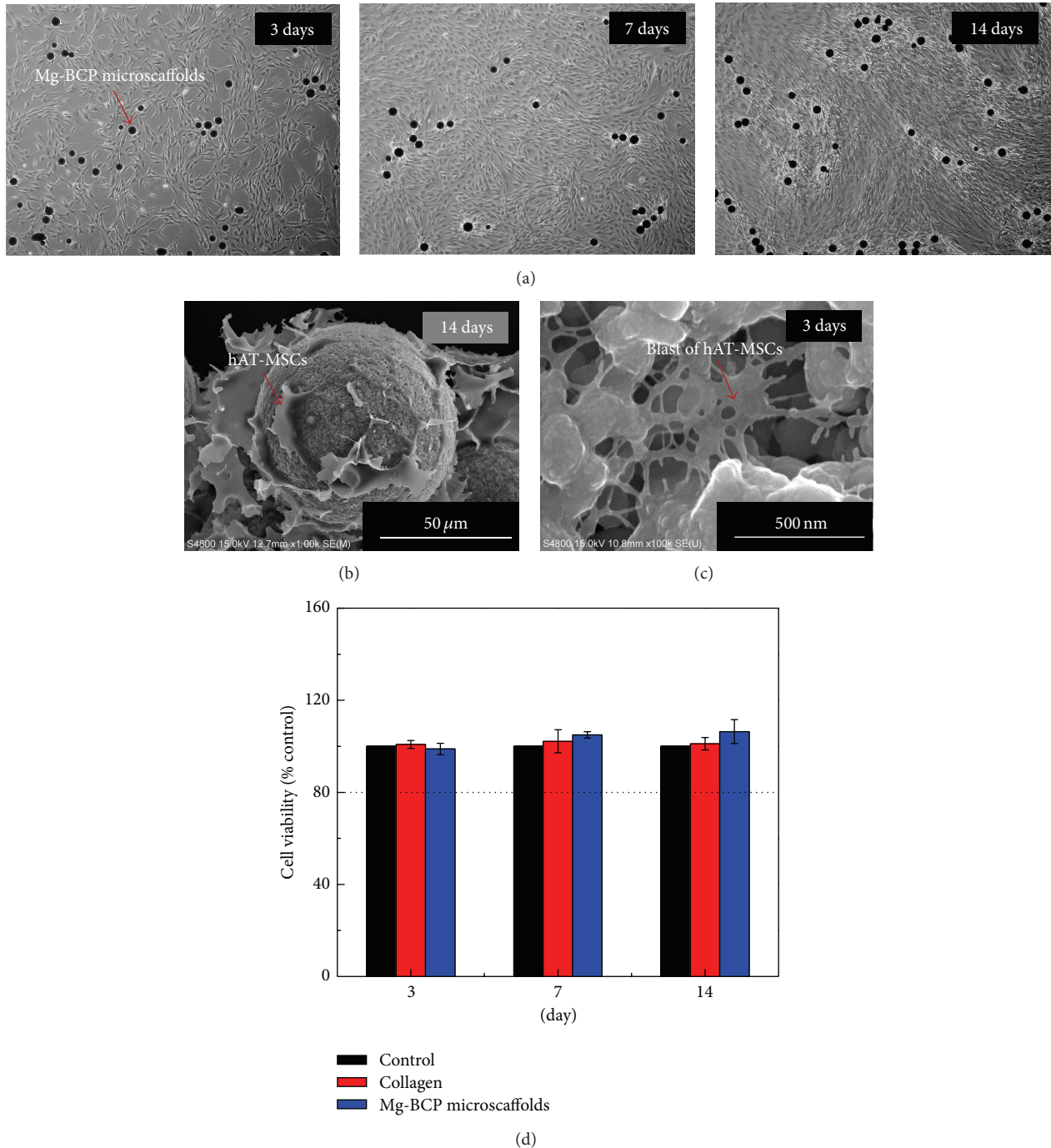


FIGURE 5: *In vitro* biological properties of hAT-MSCs with Mg-BCP microscaffolds: (a) morphological features of hAT-MSCs growth and proliferation, (b) SEM micrographs of hAT-MSCs-attached Mg-BCP microscaffolds, (c) blast of hAT-MSCs in micropore structure of Mg-BCP microscaffolds, and (d) cell viability results.

SEM-EDX mapping also shows that chemical composition atoms, indicated around the sample of implanted Mg-BCP microscaffolds, might be related to the formation of new generation bone and similar to main composition (Ca, P, and O atoms) of Mg-BCP micro-scaffold (Figure 8(b)). It can be

affirmed from these *in vivo* results that Mg-BCP microscaffolds were not only bioactive 3D extracellular tissue materials with enhanced osteoconductivity but are also suitable cell microcarriers for cell attachment and proliferation of hAT-MSCs.

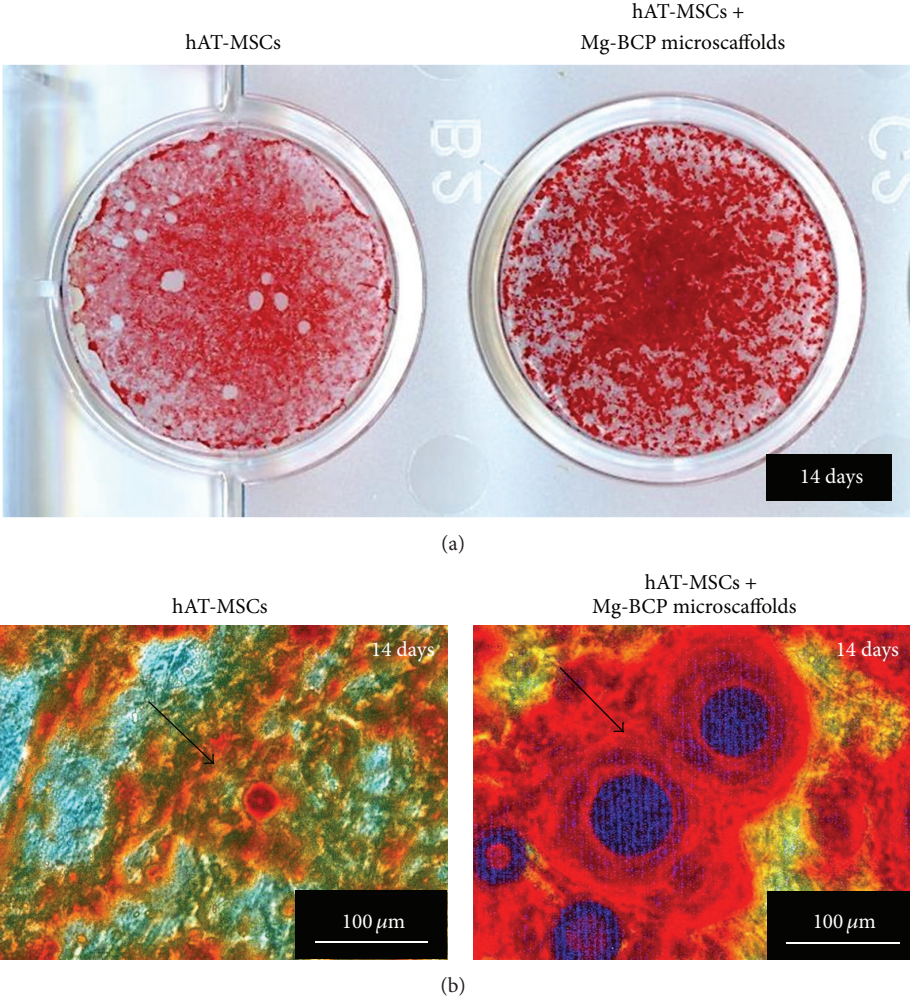


FIGURE 6: Osteogenic cell differentiation of hAT-MSCs after 14 days: (a) Alizarin Red staining area in dishes and (b) optical microscopy images.

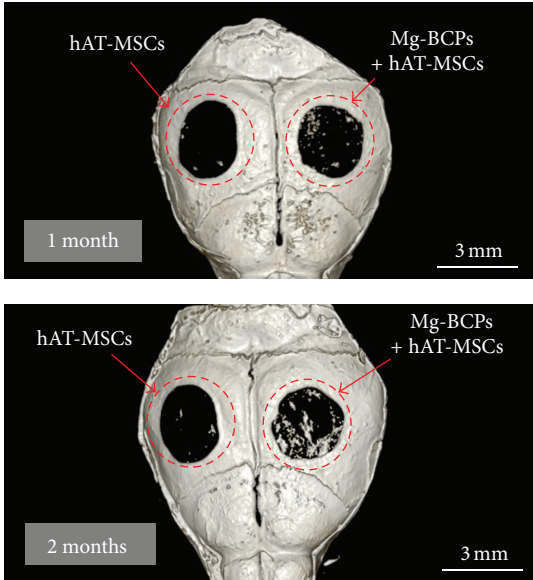


FIGURE 7: Micro-CT images of the mouse skulls after 2 months *in vivo*.

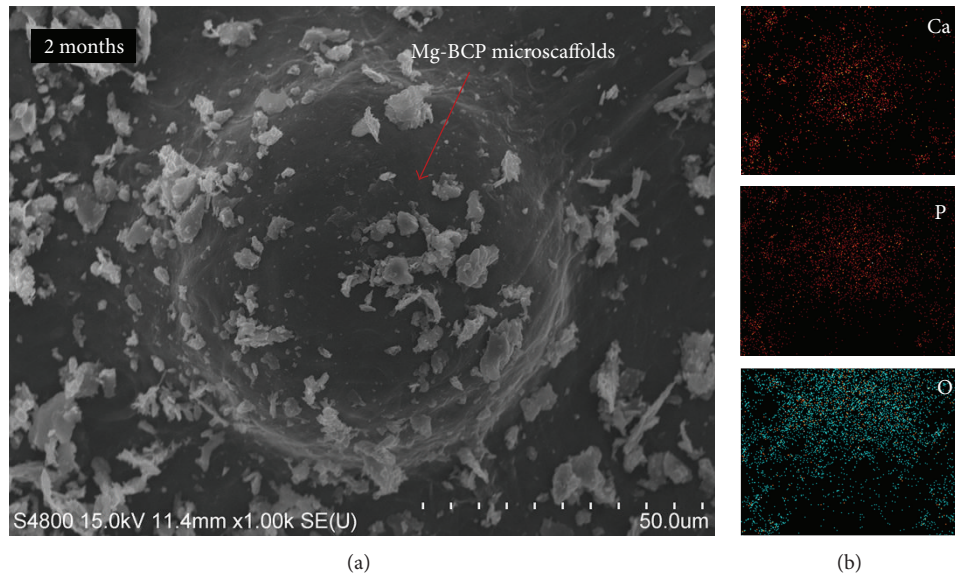


FIGURE 8: (a) FE-SEM micrographs and (b) SEM-EDX mapping results from as-implanted sample after 2 months *in vivo*.

4. Conclusions

Spherical Mg-BCP microscaffolds were successfully prepared using *in situ* coprecipitation and rotary spray drying atomization process. After immersion for 4 weeks in HBSS, Mg-BCP microscaffolds showed enhanced biodegradation and bioactivity. These biodegradation and bioactivity of Mg-BCP microscaffolds during soaking in HBSS results in the reduction of stability of the β -TCP structure due to distortion of crystal structure by the substitution of Mg^{2+} ion into Ca^{2+} sites in BCP, which has a different crystal structure. In this study, it was observed that osteogenic-differentiated hAT-MSCs have clearly attached on the surface of Mg-BCP microscaffolds. Therefore, Mg-BCP microscaffolds having enhanced biological properties related to biocompatibility and osteoconductivity could have potential application as hAT-MSCs microcarriers as seen from the *in vitro* and *in vivo* results. However, additional experimental research is needed to verify more detailed mechanism and to determine the mutual behaviors between Mg-BCP microscaffolds and hAT-MSCs.

Acknowledgments

This work was supported by the Industrial Infrastructure Program through the Korea Institute for Advancement of Technology (KIAT) grant funded by the Korea Government Ministry of Trade, Industry and Energy (no. N009700001). This research was also a part of the project titled "Development of Key Technology in Seawater Desalination Using Gas Hydrate Process" funded by the Ministry of Oceans and Fisheries and Korea Institute of Industrial Technology.

References

- [1] G. Daculsi, "Biphasic calcium phosphate concept applied to artificial bone, implant coating and injectable bone substitute," *Biomaterials*, vol. 19, no. 16, pp. 1473–1478, 1998.
- [2] B. H. Fella, O. Gauthier, P. Weiss, D. Chappard, and P. Layrolle, "Osteogenicity of biphasic calcium phosphate ceramics and bone autograft in a goat model," *Biomaterials*, vol. 29, no. 9, pp. 1177–1188, 2008.
- [3] H. Yuan, C. A. van Blitterswijk, K. de Groot, and J. D. de Bruijn, "Cross-species comparison of ectopic bone formation in biphasic calcium phosphate (BCP) and hydroxyapatite (HA) scaffolds," *Tissue Engineering*, vol. 12, no. 6, pp. 1607–1615, 2006.
- [4] M. P. Ginebra, M. Espanol, E. B. Montufar, R. A. Perez, and G. Mestres, "New processing approaches in calcium phosphate cements and their applications in regenerative medicine," *Acta Biomaterialia*, vol. 6, no. 8, pp. 2863–2873, 2010.
- [5] F. Tamimi, J. Torres, C. Kathan et al., "Bone regeneration in rabbit calvaria with novel monetite granules," *Journal of Biomedical Materials Research Part A*, vol. 87, no. 4, pp. 980–985, 2008.
- [6] W. Paul, J. Nesamony, and C. P. Sharma, "Delivery of insulin from hydroxyapatite ceramic microspheres: preliminary in vivo studies," *Journal of Biomedical Materials Research*, vol. 61, no. 4, pp. 660–662, 2002.
- [7] S. Labbaf, O. Tsigkou, K. H. Müller, M. M. Stevens, A. E. Porter, and J. R. Jones, "Spherical bioactive glass particles and their interaction with human mesenchymal stem cells in vitro," *Biomaterials*, vol. 32, no. 4, pp. 1010–1018, 2011.
- [8] Y. Gonda, K. Ioku, Y. Shibata et al., "Stimulatory effect of hydrothermally synthesized biodegradable hydroxyapatite granules on osteogenesis and direct association with osteoclasts," *Biomaterials*, vol. 30, no. 26, pp. 4390–4400, 2009.

- [9] D. J. Misiek, J. N. Kent, and R. F. Carr, "Soft tissue responses to hydroxylapatite particles of different shapes," *Journal of Oral and Maxillofacial Surgery*, vol. 42, no. 3, pp. 150–160, 1984.
- [10] B. Chang, C. Lee, K. Hong et al., "Osteoconduction at porous hydroxyapatite with various pore configurations," *Biomaterials*, vol. 21, no. 12, pp. 1291–1298, 2000.
- [11] S. V. Dorozhkin, "Biphasic, triphasic and multiphasic calcium orthophosphates," *Acta Biomaterialia*, vol. 8, no. 3, pp. 963–977, 2012.
- [12] E. Boanini, M. Gazzano, and A. Bigi, "Ionic substitutions in calcium phosphates synthesized at low temperature," *Acta Biomaterialia*, vol. 6, no. 6, pp. 1882–1894, 2010.
- [13] S. Kannan, S. I. Vieira, S. M. Olhero et al., "Synthesis, mechanical and biological characterization of ionic doped carbonated hydroxyapatite/ β -tricalcium phosphate mixtures," *Acta Biomaterialia*, vol. 7, no. 4, pp. 1835–1843, 2011.
- [14] L. Saldaña, S. Sánchez-Salcedo, I. Izquierdo-Barba et al., "Calcium phosphate-based particles influence osteogenic maturation of human mesenchymal stem cells," *Acta Biomaterialia*, vol. 5, no. 4, pp. 1294–1305, 2009.
- [15] A. Bigi, G. Falini, E. Foresti, M. Gazzano, A. Ripamonti, and N. Roveri, "Rietveld structure refinements of calcium hydroxylapatite containing magnesium," *Acta Crystallographica Section B*, vol. 52, no. 1, pp. 87–92, 1996.
- [16] A. Yasukawa, S. Ouchi, K. Kandori, and T. Ishikawa, "Preparation and characterization of magnesium-calcium hydroxyapatites," *Journal of Materials Chemistry*, vol. 6, no. 8, pp. 1401–1405, 1996.
- [17] T. W. Kim, H. S. Lee, D. H. Kim et al., "In situ synthesis of magnesium-substituted biphasic calcium phosphate and in vitro biodegradation," *Materials Research Bulletin*, vol. 47, no. 9, pp. 2506–2512, 2012.
- [18] J. H. Lee, J. W. Rhie, D. Y. Oh, and S. T. Ahn, "Osteogenic differentiation of human adipose tissue-derived stromal cells (hASCs) in a porous three-dimensional scaffold," *Biochemical and Biophysical Research Communications*, vol. 370, no. 3, pp. 456–460, 2008.
- [19] Y. J. Kim, S. W. Bae, S. S. Yu, Y. C. Bae, and J. S. Jung, "miR-196a regulates proliferation and osteogenic differentiation in mesenchymal stem cells derived from human adipose tissue," *Journal of Bone and Mineral Research*, vol. 24, no. 5, pp. 816–825, 2009.
- [20] J. I. Huang, S. R. Beanes, M. Zhu, H. P. Lorenz, M. H. Hedrick, and P. Benhaim, "Rat extramedullary adipose tissue as a source of osteochondrogenic progenitor cells," *Plastic and Reconstructive Surgery*, vol. 109, no. 3, pp. 1033–1041, 2002.
- [21] P. A. Zuk, M. Zhu, H. Mizuno et al., "Multilineage cells from human adipose tissue: implications for cell-based therapies," *Tissue Engineering*, vol. 7, no. 2, pp. 211–228, 2001.
- [22] P. A. Zuk, M. Zhu, P. Ashjian et al., "Human adipose tissue is a source of multipotent stem cells," *Molecular Biology of the Cell*, vol. 13, no. 12, pp. 4279–4295, 2002.
- [23] J. Shi, X. Zhang, Y. Pi, J. Zhu, C. Zhou, and Y. Ao, "Nanopolymer delivery of the bone morphogenetic protein-4 plasmid to mesenchymal stem cells promotes articular cartilage repair in vitro and in vivo," *Journal of Nanomaterials*, vol. 2012, Article ID 236953, 9 pages, 2012.
- [24] K. S. Moon, S. H. Yu, J. M. Bae, and S. Oh, "Biphasic osteogenic characteristics of human mesenchymal stem cells cultured on TiO₂ nanotubes of different diameters," *Journal of Nanomaterials*, vol. 2012, Article ID 252481, 8 pages, 2012.
- [25] G. Chen, W. Song, and N. Kawazoe, "Dependence of spreading and differentiation of mesenchymal stem cells on micropatterned surface area," *Journal of Nanomaterials*, vol. 2011, Article ID 265251, 9 pages, 2011.
- [26] S. Kannan, I. A. F. Lemos, J. H. G. Rocha, and J. M. F. Ferreira, "Synthesis and characterization of magnesium substituted biphasic mixtures of controlled hydroxyapatite/ β -tricalcium phosphate ratios," *Journal of Solid State Chemistry*, vol. 178, no. 10, pp. 3190–3196, 2005.

Research Article

The Investigation of Bioactivity and Mechanical Properties of Glass Ionomer Cements Prepared from Al_2O_3 - SiO_2 Glass and Poly(γ -glutamic acid)

Jinkun Liu,¹ Yoshimitsu Kuwahara,¹ Yuki Shirosaki,² and Toshiki Miyazaki¹

¹ Graduate School of Life Science and Systems Engineering, Kyushu Institute of Technology, 2-4 Hibikino, Wakamatsu-ku, Kitakyushu 808-0196, Japan

² Frontier Research Academy for Young Researchers, Kyushu Institute of Technology, 2-4 Hibikino, Wakamatsu-ku, Kitakyushu 808-0196, Japan

Correspondence should be addressed to Toshiki Miyazaki; tmiya@life.kyutech.ac.jp

Received 11 April 2013; Accepted 21 May 2013

Academic Editor: Mamoru Aizawa

Copyright © 2013 Jinkun Liu et al. This is an open access article distributed under the Creative Commons Attribution License, which permits unrestricted use, distribution, and reproduction in any medium, provided the original work is properly cited.

The glass ionomer cement as one of the dental cements has been subjected to be widespread application in restoring tooth structure. Most of glass ionomer cements employ the poly(acrylic acid) (PAA) as the liquid phase, but the presence of PAA inhibits the apatite formation on the surface in the body environment, which is an essential requirement for exhibiting bone-bonding ability (bioactivity). In this study, poly(γ -glutamic acid) (γ -PGA), a kind of biopolymer, was utilized for cement preparation. The effort of preparation parameters including the glass powders/liquid ratio (P/L) and the concentration of γ -PGA on diametral tensile strength were investigated. A maximum diametral tensile strength value of 11.88 ± 1.43 MPa was obtained when the cement sample was prepared by P/L ratio of 1:1 and the γ -PGA concentration of 30% after aging for 3 days. The TF-XRD patterns, SEM images, and EDX spectra suggested that the cement induced a precipitation of calcite on the surface after 7 days of immersion in stimulated body fluid (SBF), although the apatite formation was not observed. The present results suggest that the cement has potential to show bioactivity *in vivo*, because calcite is also reported to be bioactive.

1. Introduction

Glass ionomer cements (GICs), one kind of restorative materials, have been successfully used in dentistry for more than three decades [1]. Recently, the application is extending to implant fixation [2] and reconstructive surgical procedures [3]. Their attributes in dental role include direct adhesion to tooth mineral and release of fluoride ions to defend against dental caries [4]. Compared with other restorative cements, GICs present ease of molding, fast setting reaction, no obvious shrinkage, no significant increase in temperature [5], and better biocompatibility without inflammatory response in mouth [6].

Commercial products for cement preparation consist of $\text{CaO-Al}_2\text{O}_3$ - SiO_2 - CaF_2 glass powders and about 40–50% m/m (mass per mass) PAA solution. GICs can bond chemically to the tooth structure by developing an ion

enriched layer due to the reaction occurred between carboxyl group ($-\text{COOH}$) of PAA and calcium from the dentine or enamel [7]. When implanted into the body, negatively charged Si-OH groups on the surface of glass particles and $-\text{COOH}$ groups in PAA can attract Ca^{2+} ions easily [8]. The bonding between cements and bone is attributed to mechanical interlocking rather than a bioactive mineralized layer. Kamitakahara et al. revealed that the existence of PAA even in ppm grade inhibited the apatite formation on the GIC surface, which means that any PAA-containing GICs will lose their bioactivity in body environment [9]. If such cements are intended for orthopaedic use, a new substitution of polyalkenoic acid must be developed.

In order to provide GICs with bioactivity, a microbial γ -PGA will be adopted as an alternative acidic polymer to prepare cements. γ -PGA is a polypeptide in which the repetitive units of D- and L-glutamic acids are copolymerized

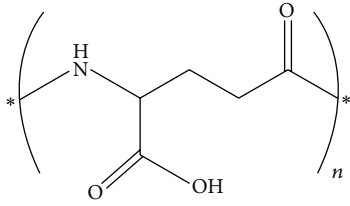


FIGURE 1: Chemical structure of poly(γ -glutamic acid).

through the chemical bond between the amino and the carboxylic groups to give the chemical structure shown in Figure 1. The polymer comes from a natural component of Natto, one kind of Japanese soybeans [10], owing water solubility, bioresorption, and nontoxicity to human beings and environment. Due to its rich $-\text{COOH}$ groups, γ -PGA as a biomaterial has been applied in drug delivery [11] and water absorption hydrogels [12]. Apatite formation on Ca^{2+} -modified γ -PGA hydrogels in simulated body fluid (SBF) has been reported by the present authors [13]. The analysis of FT-IR spectra in the literature indicated that the formation process of cement prepared by γ -PGA is similar to that described for cement prepared by PAA [14], but the information related to the bioactivity of cement is not reported.

In the present study, the aim was to build bioactive glass ionomer cements with better mechanical strength. Besides the bioactivity testing, the preparation parameters in improving the mechanical properties of cements were also optimized.

2. Materials and Methods

2.1. Poly(γ -glutamic acid). The poly(γ -glutamic acid) (γ -PGA) used in this study was a food grade polymer supplied by Meiji Seika Kaisha, Japan. The range of molecular mass was from 800,000 to 1,200,000, and the concentrations (m/m) of the γ -PGA solutions were set as 10%, 20%, 30%, and 40%, respectively.

2.2. Glass Synthesis. Glass of the basic composition of (in wt%) 50 SiO_2 , 50 Al_2O_3 was synthesized by sol-gel method [15]. The molar ratios of raw materials $\text{Si}(\text{OC}_2\text{H}_5)_4$ (Nacalai tesque, Inc., Kyoto, Japan), $\text{Al}(\text{NO}_3)_3 \cdot 9\text{H}_2\text{O}$ (Wako Pure Chemical Industries, Osaka, Japan), $\text{C}_2\text{H}_5\text{OH}$ (Wako Pure Chemical Industries, Osaka, Japan), distilled water, and hydrochloric acid (HCl, Nacalai tesque, Inc., Kyoto, Japan) as a catalyst were maintained at 1:1.18:10:50:0.02. The initial sol solutions were divided into two parts. Solution A was the mixture of 0.1 kmol m^{-3} HCl solution, half of the $\text{C}_2\text{H}_5\text{OH}$, and $\text{Al}(\text{NO}_3)_3 \cdot 9\text{H}_2\text{O}$ dissolved in the distilled water. Solution B contained $\text{Si}(\text{OC}_2\text{H}_5)_4$ and the remaining $\text{C}_2\text{H}_5\text{OH}$ and was stirred with a magnetic stirrer for 1 h at ambient temperature. Then, solution A was added dropwise to the continuous stirring solution B; the totally mixed solution was stirred for another hour and then moved into an 358 K drying oven standing for 3 days. The gel was grinded and calcined in

an electrically heated furnace in an air atmosphere at 1073 K for 2 h, where the heating rate was controlled at 5 K/min. The glass powders passed through a $<45 \mu\text{m}$ mesh sieve were adopted to prepare the filler of the cements.

2.3. Cement Preparation. Cement pastes were obtained by homogeneous mixing of glass powders with different concentration of γ -PGA solution and 10% m/m (+) tartaric acid (Wako Pure Chemical Industries, Osaka, Japan) solution on a glass slab with a spatula. The mixing ratios of powder/liquid (P/L, g/g) were increased from 1:1 to 2:1, 0.25 as an interval, and the liquid was the combination of γ -PGA and (+) tartaric acid solution. The pastes packed into the cylindrical poly(meth acrylic) molds were allowed to set and aged at 310 K in an incubator with a relative humidity (RH) of 98%.

2.4. Mechanical Strength Measurement. The mechanical strength of cements was assessed by the diametral tensile strength (DTS). The samples removed from the molds (8 mm in diameter, 4 mm in height) were applied to DTS measurement after 3 days of aging. Before the DTS testing, the diameter and length of each specimen need to be remeasured with a micrometer. The samples were crushed in diametrical direction at a crosshead speed of 1 mm/min using a computer-controlled Universal Testing Machine (Autograph AG-1, Shimadzu Co., Kyoto, Japan). The DTS values can be calculated by an equation: $\text{DTS} = 2P/\pi DL$, where P is the maximum applied load recorded at the fracture and D and L are the diameter and length of the sample, respectively. The DTS shown in the figure were average values of 10 specimens, and the bars represented standard deviation.

2.5. Incubation in Simulated Body Fluid. The simulated body fluid (SBF) was prepared by dissolving reagents of NaCl, NaHCO_3 , KCl, $\text{K}_2\text{HPO}_4 \cdot 3\text{H}_2\text{O}$, $\text{MgCl}_2 \cdot 6\text{H}_2\text{O}$, CaCl_2 , and Na_2SO_4 in ultrapure water with stirring constantly and buffering at pH 7.40 with tris(hydroxymethyl)aminomethane ($(\text{CH}_2\text{OH})_3\text{CNH}_2$) and an appropriate volume of 0.1 kmol m^{-3} HCl solution; all reagents were supplied by Nacalai tesque, Inc., Kyoto, Japan, and the details about SBF preparation were described in the literature [16]. The final composition was Na^+ 142.0, K^+ 5.0, Mg^{2+} 1.5, Ca^{2+} 2.5, Cl^- 147.8, HCO_3^- 4.2, HPO_4^{2-} 1.0 and SO_4^{2-} 0.5 in mol m^{-3} , which is nearly equal to that of human blood plasma [17].

The aged cements with the highest mechanical strength were chosen for SBF trial to evaluate the bioactivity in terms of the changes on surface structure and morphology. The cylindrical specimens with dimensions of $\phi 8 \text{ mm} \times 4 \text{ mm}$ stored in the plastic containers filled with 30 mL SBF were incubated at 310 K. After 7 days of immersion, the samples were removed, rinsed with distilled water, and dried at room temperature.

2.6. Characterization. The X-ray powder diffraction patterns were performed by thin-film X-ray diffractometer (TF-XRD; MXP3V, MAC Science Ltd., Yokohama, Japan) operated at 40 kV and 30 mA using $\text{CuK}\alpha$ as a radiation; the angle of the incident beam was anchored as 1° against the specimen

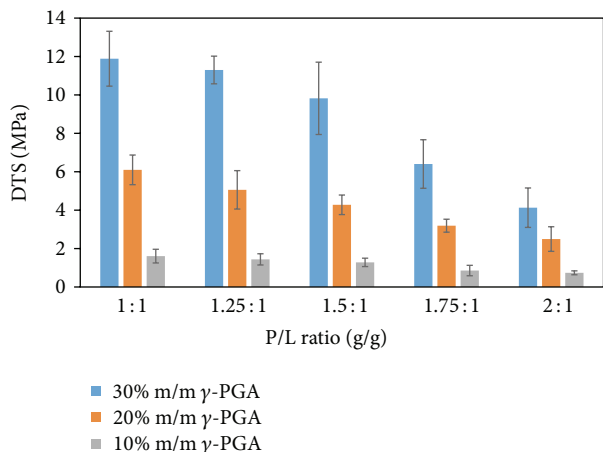


FIGURE 2: Diametral tensile strength as a function of preparation parameters of the mixing P/L ratio and the concentration of γ -PGA.

surface, and the record was using a step scanning mode with steps at 0.02° steps and 1 s. All samples were scanned from 20° to 60° in 2θ (where θ is the Bragg angle). Surface morphological features of the SBF-soaked cements were examined by scanning electron microscope (SEM; S-3500N, Hitachi High-Technologies, Tokyo, Japan) using energy-dispersive X-ray microanalyzer (EDX; EMAX Energy, Horiba Ltd., Kyoto, Japan) after sputter coating a thin film of gold on them.

3. Results and Discussion

Solid specimens stable in SBF were obtained at 10 to 30% of γ -PGA. Rough setting time of the cements was about 1 hour. When the concentration was increased up to 40%, a tendency to gelation was found in this γ -PGA solution, and the high viscosity created difficulties in the stage of measuring the amount of liquid phase and mixing the cement paste.

Figure 2 summarizes the DTS values of the cement specimens using P/L ratio of 1:1 to 2:1 and the γ -PGA concentration of 10% to 30% after 3 days of aging. The highest strength (11.88 ± 1.43 MPa) was obtained with the P/L ratio of 1:1 and the 30% m/m γ -PGA solution. It was clearly found that the preparation parameters produced significant variation on the DTS. The deterioration of DTS was following the increase of P/L ratio, and this change trend was consistent at various concentrations of the γ -PGA solution. In addition, the increase of the concentration of γ -PGA brought about apparent increase in DTS under the same P/L ratio.

When the glass powders are mixed together with the liquid, Al^{3+} ions are released from the surface of glass particles by acid attack and then leached into the aqueous medium. The leached ions bind with the polyanion chains via the carboxyl groups to precipitate a hard polycarboxylic salts gel [18–20]. The set cement consists of unreacted glass particles with a surrounding siliceous hydrogel bound together by a matrix of polyanions cross-linked by ionic bridges [21]. In the cement components, the hydrated salts composed of aluminum ion and polymer were the dominant phase

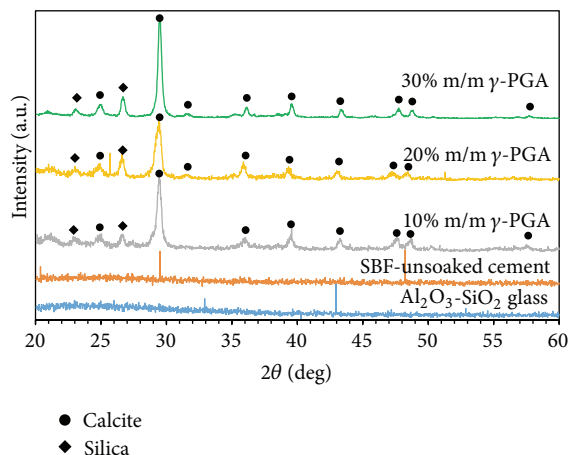


FIGURE 3: TF-XRD patterns of the surface of SBF-uns soaked cement prepared by the γ -PGA concentration of 10% m/m and P/L ratio of 1:1, the Al_2O_3 - SiO_2 glass powders, and the surfaces of cements prepared by different concentration of γ -PGA solution using P/L ratio of 1:1, after soaking in SBF for 7 days.

in determining the mechanical strength. Enhancement of physical properties can be attributed to the increase in the amount of ionic cross-links between Al^{3+} and polymer chains [22].

In this Al_2O_3 - SiO_2 glass/ γ -PGA cement, increasing concentration of γ -PGA manifested the increase in the amount of polymer chains. In addition, boosting the acidity of liquid forced more Al^{3+} ions to be released from particles. The increased polymer chains and Al^{3+} ions were sources of ionic cross-links, which implied that more aluminum polymer salts would be formed to improve the mechanical properties. Similarly, in the case of a limited content of liquid, excessive powders did not produce more ionic cross-links. Consequently, they brought about the decline in the proportion of polymer salts which resulted in the deterioration of mechanical strength, as shown in the results of DTS.

Measured maximum DTS value of the present cements is about 70% of the commercially available GICs [23]. It is reported that mechanical properties can be improved by the addition of polymer with high molecular weight [24]. Enhancement of the mechanical properties should be attempted through control in component and composition in future research.

The TF-XRD patterns of the surface of SBF-uns soaked cement, the Al_2O_3 - SiO_2 glass powders, and the surfaces of cements after soaking in SBF for 7 days are depicted in Figure 3. No crystalline peaks except a broad band centered at $2\theta = 22.8^\circ$ which is the characteristic of amorphous SiO_2 (JCPDS Card no. 29-0085) were observed, meaning that the Al_2O_3 - SiO_2 glass still maintained noncrystalline structure without forming any precipitations even after soaking in SBF. The SBF-uns soaked specimen was prepared by the γ -PGA concentration of 10% m/m and P/L ratio of 1:1; the TF-XRD pattern is similar to Al_2O_3 - SiO_2 glass's, which indicated that the powders were the main component in the cement and no crystalline phase was created during the setting and

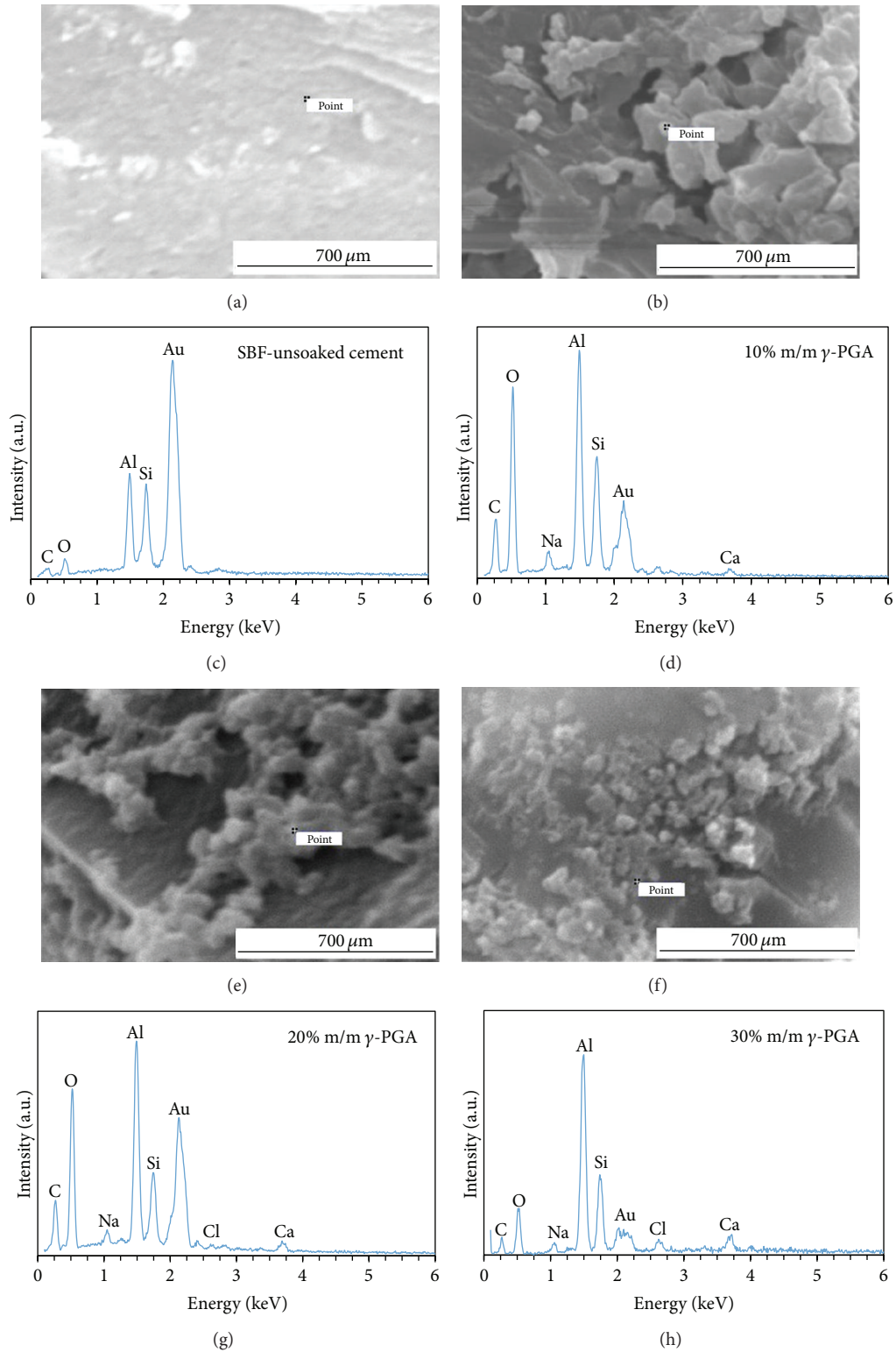


FIGURE 4: SEM micrographs and EDX spectra of the SBF-unsaturated cement surface, the deposits precipitating on the surfaces of cements, after soaking in SBF for 7 days. PGA concentration of the SBF-unsaturated cement is 10% m/m.

aging process. Moreover, the cements prepared by 20% m/m and 30% m/m γ -PGA solution had almost the same patterns before soaking in SBF. The peaks appearing at about 23.1°, 29.5°, 36.0°, 39.4°, 43.1°, 47.7°, and 48.6° in 2θ on the diffraction pattern of cements surfaces were assigned to a diffraction envelope of (102), (104), (110), (113), (202), (018), and (116) that resulted from the calcite (JCPDS Card no. 05-0586). Besides the calcite as main phase, the peaks assigned to the low-crystalline silica (JCPDS Card no. 33-1161) were also detected. The rest peaks were still unknown. The TF-XRD patterns of cements have illustrated that a chemical compound was deposited on the surfaces of cements irrespective of the concentration of γ -PGA, after soaking in SBF.

Figure 4 shows SEM micrographs combined with EDX spectra of the SBF-unsoaked cement surface and deposits. Except the elements of cement itself, no other substances were discovered on the surface of SBF-unsoaked cement according to the EDX spectra, which made it look flat and smooth in SEM micrograph. These deposits looked like spherical particles, and the range of size was from 0.5 μm and up, most of them agglomerated with each other into larger particles and precipitated on the surface of the cement. It was more obvious in the micrograph of the cement prepared by 20% m/m γ -PGA solution. The Ca peaks were detected in EDX spectra; it was an evidence that the deposits were calcium-containing compound, and the specific phase was confirmed by the TF-XRD results of cements. Besides, the amount and the size of deposits in micrographs and the intensity of calcium peak in spectra seemed not to increase with the increase in the concentration of γ -PGA.

The bioactive materials achieve the osteoconduction which is considered as a chemical attaching to bone by the formation of a biologically active apatite layer on their surfaces via chemical reactions with the surrounding body fluid [25]. This bioactive layer can prevent the materials being encapsulated by tissues then isolated from the bone [26]. The nucleation of the apatite layer is initiated by specific functional groups such as Si-OH [27], Ti-OH [28], carboxyl group (-COOH), and phosphate group [29, 30] derived from the surface of the materials. In this study, the Si-OH groups were the main constituents of a siliceous hydrogel surrounding the glass particles; the carboxyl groups may come from the unreacted γ -PGA; both of them would be ideal sites to induce the Ca^{2+} ions precipitating on the surface of the cements.

However, unlike the commercial bioactive ceramics, the precipitates were assigned as the calcite instead of the apatite. No precipitations were formed in the Al_2O_3 - SiO_2 glass filler itself even after soaking in SBF (see Figure 3). This means that the combination of the glass with γ -PGA and tartaric acid would produce preferable condition for the calcite precipitation. It is known that γ -PGA has high potential to adsorb Ca^{2+} . It is therefore assumed that the mixture of γ -PGA and other components of the cements may adsorb a lot of Ca^{2+} to produce the surface able to favorably deposit the calcite, unlike the pure γ -PGA able to deposit the calcium phosphate. The detailed mechanism on this result should be investigated in the next research.

The calcite is also considered as bioresorbable biomaterial applied in drug delivery [31]. In addition, it is reported that not only the apatite, but also the calcite can bond to rabbit tibia, although apatite layer formation in the body is not observed unlike typical bioactive materials [32]. On the basis of the report, the prepared GIC may also exhibit bioactivity.

4. Conclusions

The glass ionomer cements have been successfully attempted by using glass powders of 50 wt% SiO_2 -50 wt% Al_2O_3 composition mixed with γ -PGA solution. Increasing the concentration of γ -PGA or decreasing the P/L ratio can enhance the cross-linking degree of acidic polymers and the proportion of aluminum polymer salts in cements; both are key roles in determining the mechanical properties. The cement prepared by the P/L ratio (g/g) of 1:1 and the γ -PGA concentration of 30% m/m exhibited the highest diametral tensile strength (11.88 ± 1.43 MPa) after aging for 3 days. The calcite phase was deposited on the surface after 7 days of immersion in SBF, meaning that this Al_2O_3 - SiO_2 glass/ γ -PGA cement may own the bioactivity. Based on the diametral tensile strength and bioactivity testing result, the γ -PGA can be chosen as another alternative polyalkenoic acid in the preparation of glass ionomer cement.

Conflict of Interests

The present authors declare no conflict of interests related to this paper.

Acknowledgment

This study was supported by a Grant-in-Aid for Scientific Research ((C) 24550234) from the Japan Society for the Promotion of Science.

References

- [1] A. D. Wilson and B. E. Kent, "A new translucent cement for dentistry. The glass ionomer cement," *British Dental Journal*, vol. 132, no. 4, pp. 133–135, 1972.
- [2] I. M. Brook and P. V. Hatton, "Glass-ionomers: bioactive implant materials," *Biomaterials*, vol. 19, no. 6, pp. 565–571, 1998.
- [3] R. T. Ramsden, R. C. D. Herdman, and R. H. Lye, "Ionomeric bone cement in neuro-otological surgery," *Journal of Laryngology and Otology*, vol. 106, no. 11, pp. 949–953, 1992.
- [4] J. W. McLean, "Glass-ionomer cements," *British Dental Journal*, vol. 164, no. 9, pp. 293–300, 1988.
- [5] R. G. Hill and A. D. Wilson, "Some structural aspects of glasses used in ionomer cements," *Glass Technology*, vol. 29, no. 4, pp. 150–159, 1988.
- [6] J. W. Nicholson, "Chemistry of glass-ionomer cements: a review," *Biomaterials*, vol. 19, no. 6, pp. 485–494, 1998.
- [7] M. J. Tyas and M. F. Burrow, "Adhesive restorative materials: a review," *Australian Dental Journal*, vol. 49, no. 3, pp. 112–121, 2004.

- [8] T. Kokubo, H. Kim, and M. Kawashita, "Novel bioactive materials with different mechanical properties," *Biomaterials*, vol. 24, no. 13, pp. 2161–2175, 2003.
- [9] M. Kamitakahara, M. Kawashita, T. Kokubo, and T. Nakamura, "Effect of polyacrylic acid on the apatite formation of a bioactive ceramic in a simulated body fluid: fundamental examination of the possibility of obtaining bioactive glass-ionomer cements for orthopaedic use," *Biomaterials*, vol. 22, no. 23, pp. 3191–3196, 2001.
- [10] M. Kunioka, "Biosynthesis and chemical reactions of poly(amino acid)s from microorganisms," *Applied Microbiology and Biotechnology*, vol. 47, no. 5, pp. 469–475, 1997.
- [11] K. Hoste, E. Schacht, and L. Seymour, "New derivatives of polyglutamic acid as drug carrier systems," *Journal of Controlled Release*, vol. 64, no. 1–3, pp. 53–61, 2000.
- [12] H. J. C. Hyuk Joon Choi and M. Kunioka, "Preparation conditions and swelling equilibria of hydrogel prepared by γ -irradiation from microbial poly(γ -glutamic acid)," *Radiation Physics and Chemistry*, vol. 46, no. 2, pp. 175–179, 1995.
- [13] A. Sugino, T. Miyazaki, and C. Ohtsuki, "Apatite-forming ability of polyglutamic acid hydrogels in a body-simulating environment," *Journal of Materials Science: Materials in Medicine*, vol. 19, no. 6, pp. 2269–2274, 2008.
- [14] A. S. Ledezma-Pérez, J. Romero-García, G. Vargas-Gutiérrez, and E. Arias-Marín, "Cement formation by microbial poly(γ -glutamic acid) and fluoroaluminosilicate glass," *Materials Letters*, vol. 59, no. 24–25, pp. 3188–3191, 2005.
- [15] M. Taira and M. Yamaki, "Preparation of SiO_2 - Al_2O_3 glass powders by the sol-gel process for dental applications," *Journal of Materials Science: Materials in Medicine*, vol. 6, no. 4, pp. 197–200, 1995.
- [16] T. Kokubo and H. Takadama, "How useful is SBF in predicting *in vivo* bone bioactivity?" *Biomaterials*, vol. 27, no. 15, pp. 2907–2915, 2006.
- [17] T. Kokubo, S. Ito, Z. T. Huang et al., "Ca, P-rich layer formed on high-strength bioactive glass-ceramic A—W," *Journal of Biomedical Materials Research*, vol. 24, no. 3, pp. 331–343, 1990.
- [18] S. Crisp and A. D. Wilson, "Reactions in glass ionomer cements: I. Decomposition of the powder," *Journal of Dental Research*, vol. 53, no. 6, pp. 1408–1413, 1974.
- [19] S. Crisp, M. A. Pringuer, D. Wardleworth, and A. D. Wilson, "Reactions in glass ionomer cements: II. An infrared spectroscopic study," *Journal of Dental Research*, vol. 53, no. 6, pp. 1414–1419, 1974.
- [20] S. Crisp and A. D. Wilson, "Reactions in glass ionomer cements: III. The precipitation reaction," *Journal of Dental Research*, vol. 53, no. 6, pp. 1420–1424, 1974.
- [21] V. H. W. Khouw-Liu, H. M. Anstice, and G. J. Pearson, "An *in vitro* investigation of a poly(vinyl phosphonic acid) based cement with four conventional glass-ionomer cements. Part I: flexural strength and fluoride release," *Journal of Dentistry*, vol. 27, no. 5, pp. 351–357, 1999.
- [22] S. Crisp, B. G. Lewis, and A. D. Wilson, "Characterization of glass-ionomer cements I. Long term hardness and compressive strength," *Journal of Dentistry*, vol. 4, no. 4, pp. 162–166, 1976.
- [23] D. Xie, W. A. Brantley, B. M. Culbertson, and G. Wang, "Mechanical properties and microstructures of glass-ionomer cements," *Dental Materials*, vol. 16, no. 2, pp. 129–138, 2000.
- [24] A. H. Dowling and G. J. P. Fleming, "Can poly(acrylic) acid molecular weight mixtures improve the compressive fracture strength and elastic modulus of a glass-ionomer restorative?" *Dental Materials*, vol. 27, no. 11, pp. 1170–1179, 2011.
- [25] D. Arcos, I. Izquierdo-Barba, and M. Vallet-Regí, "Promising trends of bioceramics in the biomaterials field," *Journal of Materials Science: Materials in Medicine*, vol. 20, no. 2, pp. 447–455, 2009.
- [26] L. L. Hench, "Bioceramics," *Journal of the American Ceramic Society*, vol. 81, no. 7, pp. 1705–1727, 1998.
- [27] P. Li, C. Ohtsuki, T. Kokubo, K. Nakanishi, N. Soga, and K. de Groot, "The role of hydrated silica, titania, and alumina in inducing apatite on implants," *Journal of Biomedical Materials Research*, vol. 28, no. 1, pp. 7–15, 1994.
- [28] M. Uchida, H. Kim, T. Kokubo, S. Fujibayashi, and T. Nakamura, "Structural dependence of apatite formation on titania gels in a simulated body fluid," *Journal of Biomedical Materials Research A*, vol. 64, no. 1, pp. 164–170, 2003.
- [29] M. Tanahashi and T. Matsuda, "Surface functional group dependence on apatite formation on self-assembled monolayers in a simulated body fluid," *Journal of Biomedical Materials Research A*, vol. 24, no. 2, pp. 305–315, 1997.
- [30] T. Miyazaki, C. Ohtsuki, Y. Akioka et al., "Apatite deposition on polyamide films containing carboxyl group in a biomimetic solution," *Journal of Materials Science: Materials in Medicine*, vol. 14, no. 7, pp. 569–574, 2003.
- [31] J. Wang, J. Chen, J. Zong et al., "Calcium carbonate/carboxymethyl chitosan hybrid microspheres and nanospheres for drug delivery," *Journal of Physical Chemistry C*, vol. 114, no. 44, pp. 18940–18945, 2010.
- [32] Y. Fujita, T. Yamamuro, T. Nakamura, S. Kotani, C. Ohtsuki, and T. Kokubo, "The bonding behavior of calcite to bone," *Journal of Biomedical Materials Research*, vol. 25, no. 8, pp. 991–1003, 1991.

Research Article

Mineralization and Osteoblast Cells Response of Nanograde Pearl Powders

Jian-Chih Chen,¹ Jung-Chang Kung,² Chih-Hsin Hsieh,¹ Mei-Ju Hou,³
Chi-Jen Shih,³ and Chun-Cheng Hung^{4,5}

¹ Department of Orthopaedics, Kaohsiung Medical University Hospital, Kaohsiung Medical University, Kaohsiung 807, Taiwan

² Department of Family Dentistry, Kaohsiung Medical University Hospital, Kaohsiung Medical University, Kaohsiung 807, Taiwan

³ Department of Fragrance and Cosmetic Science, Kaohsiung Medical University, 100 Shi-Chuan 1st Road, Kaohsiung 80708, Taiwan

⁴ School of Dentistry, College of Dental Medicine, Kaohsiung Medical University, Kaohsiung 807, Taiwan

⁵ Department of Prosthodontics, Kaohsiung Medical University Hospital, Kaohsiung Medical University, Kaohsiung 807, Taiwan

Correspondence should be addressed to Chi-Jen Shih; cjshih@kmu.edu.tw and Chun-Cheng Hung; chuchh@cc.kmu.edu.tw

Received 10 March 2013; Revised 7 May 2013; Accepted 7 May 2013

Academic Editor: Eng San Thian

Copyright © 2013 Jian-Chih Chen et al. This is an open access article distributed under the Creative Commons Attribution License, which permits unrestricted use, distribution, and reproduction in any medium, provided the original work is properly cited.

The main objective of this study is to characterize the thermal, mineralization, and osteoblast cells response of pearl nanocrystallites. The results obtained from X-ray diffraction, FTIR spectra demonstrate that the pearl nano-crystallites can induce the formation of an HA layer on their surface in SBF, even after only short soaking periods. The in vitro cell response to nano-grade pearl powders is assessed by evaluating the cytotoxicity against a mouse embryonic fibroblast cell line and by characterizing the attachment ability and alkaline phosphatase activity of mouse bone cells (MC3T3-E1, abbreviated to E1) and bone marrow stromal precursor (D1) cells. The cytotoxicities of pearls were tested by the filtration and culture of NIH-3T3 mouse embryonic fibroblast cells. The viability of the cultured cells in media containing pearl crystallites for 24 and 72 h is greater than 90%. The bone cells seen in these micrographs are elongated and align predominately along the pearl specimen. The cells observed in these images also appeared well attached and cover the surface almost completely after 1 h. The pearl nanocrystallites had a positive effect on the osteogenic ability of ALP activity, and this promoted the osteogenic differentiation of MSCs significantly at explanations.

1. Introduction

Pearl, which is composed of nacre, is produced in an active physiological environment by molluscs. Pearl, nacre, and bone are all biomineralization products of organisms. Pearl and nacre are basically composed of calcium carbonate (aragonite, CaCO_3), whereas bone mainly consists of calcium phosphate or hydroxyl apatite (HA); although their components are different, parts of the complex machineries that direct their formation may be homologous [1, 2]. Nacre has been reported to contain one or more signal molecules [3, 4] similar to bone morphogenetic proteins (BMPs), bone growth factors present in human bone that can activate the osteogenic bone marrow cells both in vivo and in vitro and lead to bone formation. Atlan et al. [5] conducted an important bone repair experiment of eight female patients

using nacre powder, finding that osteoblasts were clearly attracted to the nacre, and new bone formed throughout the implanted material after six months. This activity is thought to be due to the similarity between the growth proteins present in nacre and those in bone. Nacres are considered suitable natural materials for dental and bone restorations [6–13]. In addition to their worldwide availability and low cost, they can initiate and induce mineralized tissue formation by human osteoblasts in vitro, and they also exhibit osteogenic and osteoinductive features due to their ability to bond with bone. At present, nacre is considered a promising osteoinductive material. Pearl contains more organic substances and trace elements, so it is expected that pearl will show better osteogenic activity than shell nacre since it is a natural carrier of bone growth factors. Moreover, pearls are currently cultured on a large scale in many countries, so

pearls are now commercially available at an affordable price [14].

In this study, morphology evaluation using the Brunauer, Emmett, and Teller (BET) method was performed in conjunction with high resolution transmission electron microscope (HRTEM). The mineralization of pearl powders was tested by immersing the pearl samples in simulated body fluid (SBF). The formation of a crystalline phase on the surface of the pearls was identified by scanning electron microscopy and X-ray diffraction. The *in vitro* cell response to nanograde pearl powders is assessed by evaluating the cytotoxicity against a mouse embryonic fibroblast cell line and by characterizing the attachment ability and alkaline phosphatase activity of mouse bone cells (MC3T3-E1, abbreviated to E1) and bone marrow stromal precursor (D1) cells.

2. Experimental Procedure

2.1. Nanograde Pearl Crystallite Preparation. The nanoparticles were prepared using the wet polish method with a ball grinding machine (Just Nanotech Co., JBM-B035, Taiwan). A mixture of dry ingredients composed of 8 g of pearl powder and 1.6 g of dispersant was added to 240 mL of deionized water to make slurry. The slurry was premixed for 1.5 h and then placed in a grind chamber with 500 g of 0.1 mm zirconium particles for 1.0 h at 2000 rpm. After grinding, the slurry was passed through a 200 mesh sieve to remove the larger particles. The slurry was then dried by freeze-drying at 218 K under vacuum. The original morphologies of the specimens were characterized by scanning electron microscopy (SEM) as shown in Figure 1.

2.2. Thermal Characterization. Differential thermal and thermogravimetric analyses (DT/TGA) were conducted on powder samples in 50 mg quantities at heating rates of 5°C/min. Samples were heated from 25°C to 1200°C in air. Crystalline phases were identified using X-ray diffraction (XRD) analysis. XRD was performed using an X-ray diffractometer with Cu K α radiation and a Ni filter operated at 30 kV and 20 mA, with a scanning rate of 4°/min. Fourier transform infrared (FTIR) absorption spectra were obtained with a spectral resolution of 4 cm⁻¹. For FTIR, each sample was mixed with KBr (in a 1:10 glass:KBr mass ratio) and pressed into a 200 mg pellet with a diameter of 12 mm. Infrared absorption spectra were obtained over the frequency range of 400–4000 cm⁻¹. Composite spectra presented for each sample represent an average of 64 scans, normalized to the spectrum of a blank KBr pellet. The specific surface areas of the samples were measured using the conventional BET method (ASAP 2010, Micromeritics, USA) with nitrogen as the absorbent.

2.3. *In Vitro* Bioactivity Test. The mineralization of the pearl powders was assessed in a simulated body fluid (SBF) similar to human plasma [15]. The *in vitro* bioactivity of the powders was tested by immersing the samples in simulated body fluid (SBF) at a solid:liquid ratio of 1 mg/mL at 37°C. The formation of hydroxyapatite on the surface of the sample was

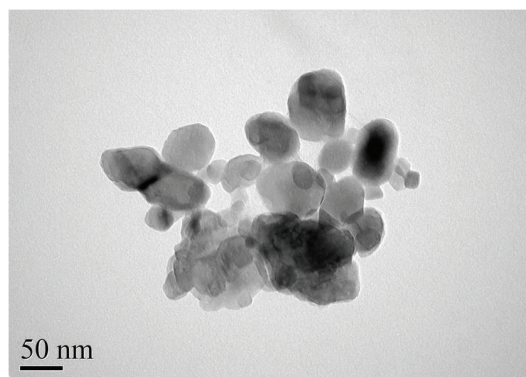


FIGURE 1: TEM image of ground pearl powders.

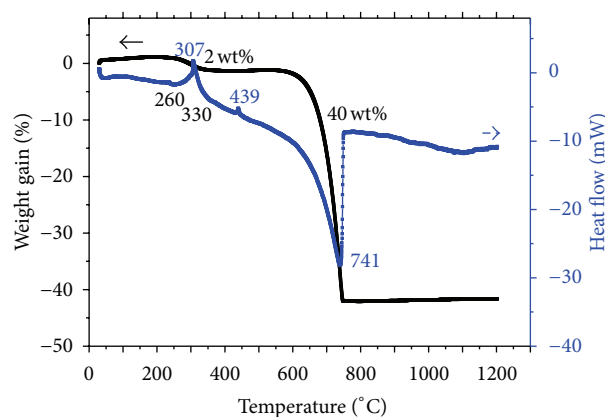


FIGURE 2: DTA/TGA curves of pearl powders at a heating rate of 5°C/min in air.

studied as a function of time. The crystalline phase was identified by scanning electron microscopy ((SEM) Philips XL40 FE-SEM) and X-ray diffraction ((XRD) Shimadzu, XRD-6000). XRD was performed using an X-ray diffractometer with Cu K α radiation and a Ni filter operated at 30 kV, 20 mA and a scanning rate of 4° min⁻¹.

2.4. Cytotoxicity of Pearl Powders. The cytotoxicities of the MBGs were tested by filtration and culture of the fibroblast cells (NIH 3T3, abbreviated 3T3). The cells were provided by the National Institute of Health (NIH) in Taiwan. The 3T3 cells were derived from newborn mouse fibroblasts and cultured in Dulbecco's modified Eagle's medium (DMEM) (Gibco, Invitrogen Taiwan Ltd., MD) containing 10% bovine serum (BS) (Biological Industries, Haemek, Israel). An XTT Cell Viability Assay Kit provided a simple method to count live cells using an absorbance reader. The cells' adhesive and reproductive abilities were measured at two early stages: 24 h and 72 h. After the cultured time, the cells on the sample surface were washed with phosphate-buffered saline (PBS) and transferred to 200 μ L of culture medium with a 100 μ L XTT kit and were incubated for another 4 h. The reaction medium was then measured spectrophotometrically at 490 nm using an ELISA microplate reader UVM-340 (ASYS Hitech GmbH, Eugendorf, Austria). Finally, the cell

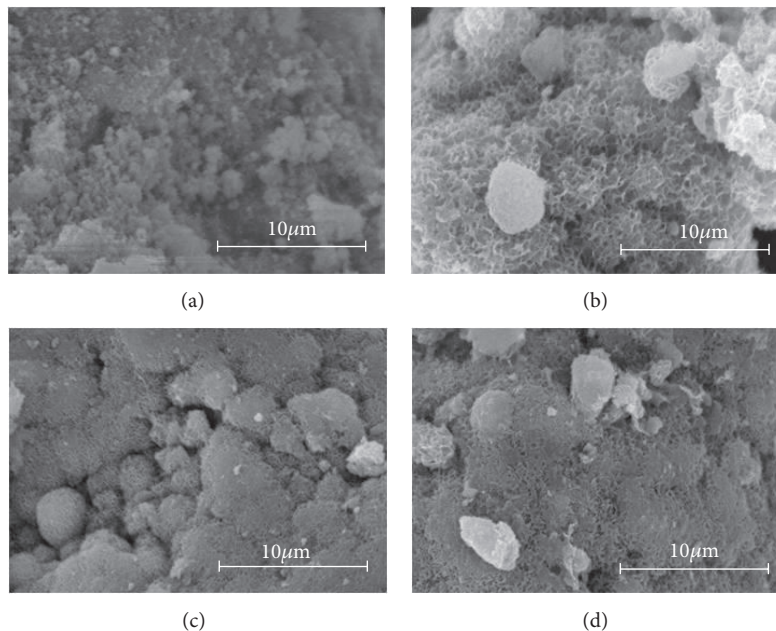


FIGURE 3: FE-SEM micrograph spectra of pearl powders before (a) and after being immersed in SBF for (b) 4 h, (c) 6 h, and (d) 24 h.

numbers were determined from a plot of absorbance (OD values) versus the 3T3 cells after adjustment via XTT assays. Each experiment was performed five times ($n = 5$). The statistical analyses of the results were analyzed using one-way ANOVA to investigate the significant group comparisons between different populations using the JMP 9.0 software (SAS Institute, Inc., Cary, NC, USA). In all cases, the results were considered to be significantly different when $P < 0.05$.

2.5. Cell Seeding and SEM Specimen Preparation. E1 cells were cultured on pearl disks placed in a 96-well culture plate at an initial density of 1×10^5 cells/cm². The cells were incubated for 1, 24, 72, and 168 h. The pearl disks were then fixed in a 25% glutaraldehyde, 4% paraformaldehyde matrix for 1 h at 4°C. The cells were washed in wash buffer containing 4% sucrose in PBS and postfixed in 1% osmium tetroxide in PBS for 1 h at 4°C. The samples were then dehydrated sequentially in graded ethanol (30%, 50%, 70%, 95%, and 100% ethanol). The specimens were dried in hexamethyldisilazane (HMDS) for 3 min before they were coated with gold for SEM analysis. The morphological characteristics of the cells attached to the pearl disks were determined using field-emission SEM. To quantitatively evaluate the E1 cells adhered to the pearl disks over time, an alamarBlue assay kit (AbD Serotec, Oxford, UK) was used. After 1, 24, 72, and 168 h, the tested samples were washed with PBS and moved to a new plate. Then, 500 mL of culture medium and 50 mL of alamarBlue were added to the samples, and the samples were incubated for 2 h. After incubation, 100 mL of the reactants were extracted and measured using the ASYS UVM 340 microplate reader. The absorbance values of the reactants ($n = 5$) were monitored at 570 and 600 nm. After 30 min, the reaction was stopped by adding solutions of 25 µL of 3 M NaOH. The

statistical analyses of the results were analyzed using one-way ANOVA to investigate the significant group comparisons between different populations using the JMP 9.0 software (SAS Institute, Inc., Cary, NC, USA). In all cases, the results were considered to be significantly different when $P < 0.05$.

2.6. Osteogenic Evaluations. The ALP and TRAP activities were detected using a TRACP and ALP Double-Staining Kit (TaKaRa Bio Inc., Shiga, Japan) according to the manufacturer's instructions. Elevation in ALP activity in D1 cells reflects those osteogenic cells that were undergoing terminal differentiation. D1 cells were seeded at 1×10^5 cell/well in a 48-well plate. Cells were cultured for 1, 24, 72, and 168 h. D1 cells were harvested and washed with PBS. After washing, solutions of 500 µL p-nitrophenyl phosphate (FASTTM pNPP Substrate Tablet Set (Sigma Chemical Co., Poole, Dorset, UK) in 0.05 M Tris buffer) were added to the wells. After 30 min, the reaction was stopped by adding 25 µL 3 M NaOH. Absorption was measured at 405 nm.

3. Results and Discussion

3.1. Morphology and Thermal Behavior of Pearl Crystallites. The morphology of the milled pearl crystallites was characterized by transmission electron microscopy (TEM) as shown in Figure 1. The ultrafine particle size was less than 100 nm, and the specific surface area of the pearl crystallites (N₂, BET) was found to be 28.9 m²/g. DTA/TG heating curves of pearl powders measured at a heating rate of 5°C/min from 25°C to 1200°C are shown in Figure 2. There is an endothermic peak at about 307°C accompanied by a 2% weight loss ascribed to the organic species of the materials included in the pearl powder. This observation provides

further evidence that pearl is not entirely inorganic, with protein molecules incorporated into each layer [15, 16]. The exothermic peak at 439°C is due to the aragonite to calcite transformation of the CaCO_3 nanoparticles. During the heating from 580 to 750°C, the weight loss and exothermic peak around 741°C are ascribed to the decomposition of CO_2 .

3.2. Mineralization of Pearl Nanocrystallites In Vitro. One significant characteristic of bioactive materials is their ability to bond with living tissue, in this case bone. Bonding occurs through the formation of an HA interface layer on the surface, both in vitro and in vivo [17]. The in vitro bioactivity of the pearl nanocrystallites was investigated by soaking them in simulated body fluid. SEM images of the pearl before and after soaking in SBF for 4 h, 6 h, and 24 h are shown in Figure 3. The pearl surface was smoothed before soaking in SBF. The surfaces of these pearls show important changes after soaking in SBF for 4 h. The surface was fully covered with a layer of needle-shaped crystallites. Furthermore, the thickness of the HA layer and the spherical particles with needle-like crystallites increases with increasing soaking times. The above results indicate that these pearls can induce the formation of an HA layer on their surface in SBF even for short soaking periods, which demonstrates the excellent in vitro bone forming bioactivity of pearls. The XRD patterns of the pearl powders before and after soaking in SBF are shown in Figure 4, which indicate the aragonite phase of CaCO_3 before soaking. After soaking in SBF for 4 h, two diffraction peaks at 31.7° and 25.8° appeared, corresponding to the (211) and (002) reflections of hydroxide apatite. Figure 5 summarizes the FTIR spectra of the pearl powders before and after soaking in SBF. Before soaking, the CO_3^{2-} ion bending and stretching vibrations that give rise to absorption at 700–864 and 844–1090 cm^{-1} are present. The strong IR band detected at 1792 cm^{-1} could also be attributed to the C=O groups of the carbonate ions. After 4 h of soaking in SBF, the band at 603 cm^{-1} split into a doublet at 562 and 603 cm^{-1} , corresponding to a crystalline phosphate. This agrees with the results of the XRD patterns. After soaking in SBF for 4 h, reflections of hydroxide apatite appeared. Similar phenomena have also been observed in the in vitro osteogenic activity of pearl [14]. HA can be formed on pearl surface in SBF based on a dissolution-binding-precipitation mechanism. HRTEM analysis provides direct microstructural evidence for poorly crystallized HA, it indicates that there are so many arranged dislocations and shuttle-like amorphous areas in HA particles, and calcium surplus in HA crystal structure is found, which implies that HA is formed on pearl surface in their study [14].

3.3. Cytotoxicity of Nanograde Pearl Crystallites. The in vitro cell response was assessed by evaluating the cytotoxicity of these materials against the mouse embryonic fibroblast cell line. Cell proliferation in the presence of nanograde pearl crystallites was evaluated using an XTT assay. Cells were assessed in both the absence and presence of nanograde pearl crystallites as a function of culture time. NIH-3T3 mouse

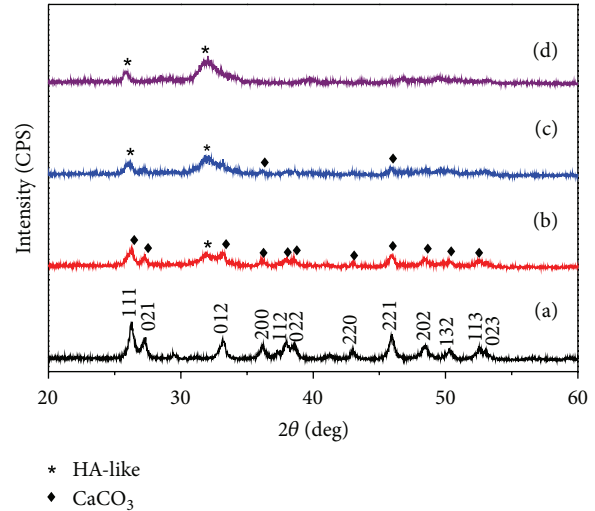


FIGURE 4: XRD patterns of pearl powders before (a) and after being immersed in SBF for 4 h (b), 6 h (c), and 24 h (d).

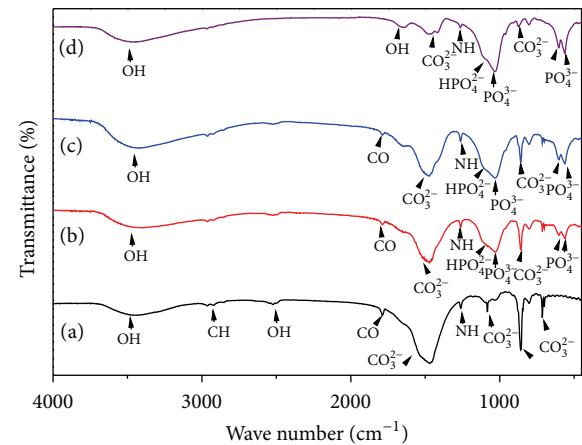


FIGURE 5: FTIR spectra of pearl powders (a) before and after being immersed in SBF for (b) 4 h, (c) 6 h, and (d) 24 h.

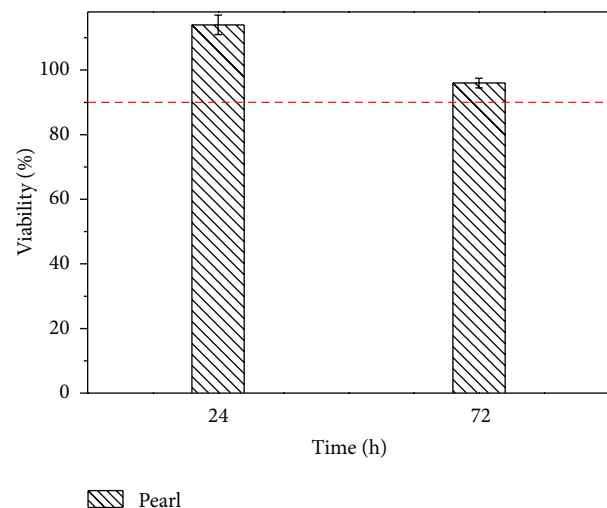


FIGURE 6: Viability of NIH-3T3 cells for various durations cultured for 72 h and immersed in the media. ($n = 5$, $P < 0.05$).

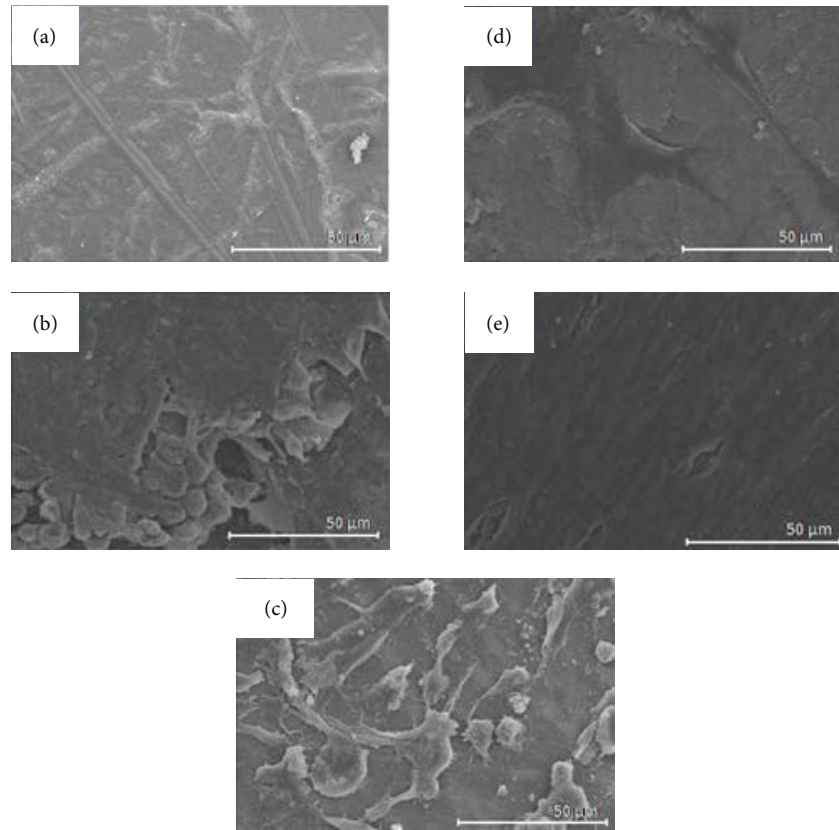


FIGURE 7: SEM images of the attachment of MC3T3-E1 cultured on pearls: (a) initial, (b) 1 h, (c) 24 h, (d) 72 h and (e) 168 h.

embryonic fibroblast cells were cultured in media containing pearl crystallites for 24 and 72 h, as depicted in Figure 6. As the culture time increased from 24 to 72 h, the viability of the cultured cells did not change considerably. The viability of the cultured cells in media containing pearl crystallites for 24 and 72 h is greater than 90%.

3.4. Bone Cell Attachment onto Pear Disks. The cells were cultured for 1, 24, 72, and 168 h each to determine their adhesive and initial proliferative abilities. Figure 7 indicates that the E1 cells adhere to the pearl disks in different stages. Initially, the osteoblastic cells seen in these micrographs are elongated, with alignment predominately along the specimen. The cells shown in these images appear well attached and almost completely cover the surface after 1 h. To quantitatively investigate the E1 cells adhered to pearl disks over time, the number of cells was monitored as a function time, as illustrated in Figure 8. A significant increase initially from 5.68×10^4 to 8.81×10^4 (about 55% increases) from 1 h to 24 h. There are not many differences between 24 h and 72 h and abruptly increased to 1.13×10^5 (about 99.2% increases) between 72 h and 168 h. Based on the above-mentioned results, it is therefore believed that pearls can facilitate bone cell adhesion, differentiation, and proliferation.

3.5. Osteogenic Evaluations. The ALP activities were significantly larger over time when compared with the initial

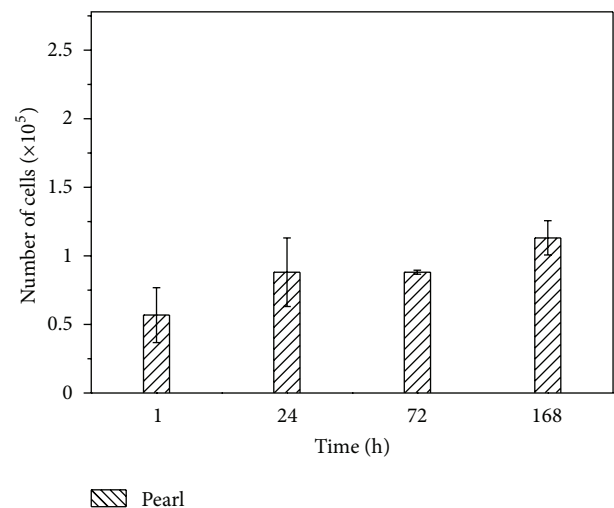


FIGURE 8: MC3T3-E1 cell numbers were counted after (a) 1 h (b) 24 h (c) 72 h, and (d) 168 h. ($n = 5$, $P < 0.05$).

time points. The examination of ALP quantities via staining confirmed this phenomenon. A longer incubation time greatly increased the level of ALP (Figure 9). To quantitatively investigate the ALP activities to pearl disks over time, the ALP activities were monitored as a function time, as illustrated in Figure 10. The ALP activities significantly increased initially

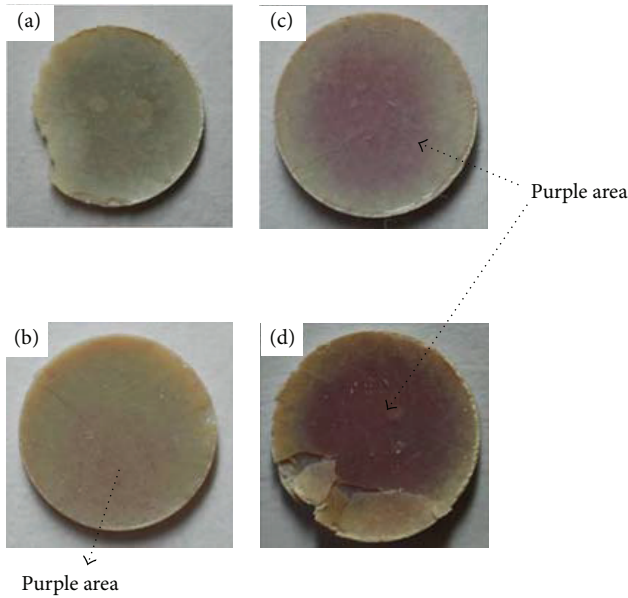


FIGURE 9: Light photos of the pearl promoted the ALP activity of cell line D1 at (a) initial (b) 24 h (c) 72 h and (d) 168 h.

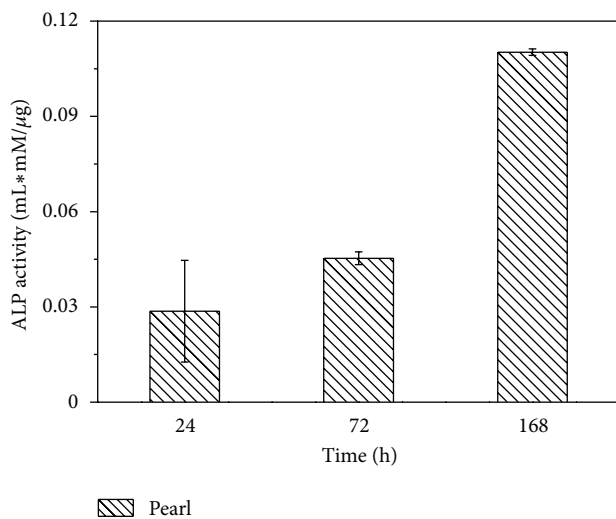


FIGURE 10: Pearl promoted the ALP activity of cell line D1 at 24 h, 72 h and 168 h. ($n = 5$, $P < 0.05$).

from 0.029 to 0.045 in the range of 24 h to 72 h and then increased to 0.11 between 72 h and 168 h. Our results show that the pearl nano-crystallites had a large positive effect on osteogenic ALP activity, and this promoted the osteogenic differentiation of MSCs significantly at explanations.

4. Conclusion

The main objective of this study is to characterize the morphology, mineralization, and osteoblast cells response of pearl nano-crystallites. Results are summarized as follows.

- (1) DTA/TG heating showed an endothermic peak at about 307°C accompanied by a 2% weight loss

ascribed to the decomposition of the organic species of the materials included in the pearl powder. The exothermic peak at 439°C is due to the aragonite to calcite transformation of the CaCO_3 nanoparticles. During the heating from 580 to 750°C , the weight loss and exothermic peak around 741°C are ascribed to the decomposition of CO_2 .

- (2) X-ray diffraction (XRD), Fourier transform infrared (FTIR) absorption spectra, and analysis showed further evidence that pearls can induce the formation of an HA layer on their surface in SBF, even for short soaking periods.
- (3) Nanograde pearl powders induced the formation of apatite layer on their surface after soaking in SBF for 4 h, which demonstrates the excellent in vitro bone forming bioactivity of nanograde pearls.
- (4) The cytotoxicities of pearls were tested by the filtration and culture of NIH-3T3 mouse embryonic fibroblast cells. The viability of the cultured cells in media containing pearl crystallites for 24 and 72 h is greater than 90%.
- (5) Bone cells adhered to the pearl disks, as evidenced by scanning electron micrographs. Specifically, these micrographs of E1 cells were adhered to pearl disks taken over a culture interval of 1 h. The osteoblastic cells shown in these micrographs are elongated, with their alignment predominately along the specimen. The cells shown in these images also appear well attached and cover the surface almost completely after 1 h. It is therefore believed that pearls can facilitate bone cell adhesion.
- (6) The pearl nanocrystallites had a positive effect on the osteogenic ability of ALP activity, and this promoted the osteogenic differentiation of MSCs significantly at explanations.

Authors' Contribution

J.-C. Chen and J.-C. Kung contributed equally to this work.

Acknowledgments

This work was financially support of a Grant from the National Science Council of Taiwan (NSC 98-2622-E-037-001-CC3). The authors also acknowledge the supported by Grants from the Kaohsiung Medical University Hospital (KMUH100-0 M25, KMUH100-0 M51) and Grants from the Kaohsiung Medical University Research Foundation (KMU-M110008, KMU-M102006).

References

- [1] P. Westbroek and F. Marin, "A marriage of bone and nacre," *Nature*, vol. 392, no. 6679, pp. 861–862, 1998.
- [2] M. Rousseau, L. Pereira-Mouriès, M. J. Almeida, C. Milet, and E. Lopez, "The water-soluble matrix fraction from the nacre of *Pinctada maxima* produces earlier mineralization of

- MC3T3-E1 mouse pre-osteoblasts,” *Comparative Biochemistry and Physiology B*, vol. 135, no. 1, pp. 1–7, 2003.
- [3] M. Lamghari, M. J. Almeida, S. Berland et al., “Stimulation of bone marrow cells and bone formation by nacre: in vivo and in vitro studies,” *Bone*, vol. 25, no. 2, pp. 91S–94S, 1999.
- [4] I. M. Weiss, W. Göhring, M. Fritz, and P. K. Mann, “Perlustrin, a *Haliotis laevis* (abalone) nacre protein, is homologous to the insulin-like growth factor binding protein N-terminal module of vertebrates,” *Biochemical and Biophysical Research Communications*, vol. 285, no. 2, pp. 244–249, 2001.
- [5] G. Atlan, N. Balmain, S. Berland, B. Vidal, and E. Lopez, “Reconstruction of human maxillary defects with nacre powder: histological evidence for bone regeneration,” *Comptes Rendus de l’Academie des Sciences III*, vol. 320, no. 3, pp. 253–258, 1997.
- [6] C. M. Zaremba, D. E. Morse, S. Mann, P. K. Hansma, and G. D. Stucky, “Aragonite-hydroxyapatite conversion in gastropod (abalone) nacre,” *Chemistry of Materials*, vol. 10, no. 12, pp. 3813–3824, 1998.
- [7] G. Atlan, O. Delattre, S. Berland et al., “Interface between bone and nacre implants in sheep,” *Biomaterials*, vol. 20, no. 11, pp. 1017–1022, 1999.
- [8] H. Liao, H. Mutvei, M. Sjöström, L. Hammarström, and J. Li, “Tissue responses to natural aragonite (*Margaritifera* shell) implants in vivo,” *Biomaterials*, vol. 21, no. 5, pp. 457–468, 2000.
- [9] H. Liao, C. Brandsten, C. Lundmark, T. Wurtz, and J. Li, “Responses of bone to titania-hydroxyapatite composite and nacreous implants: a preliminary comparison by in situ hybridization,” *Journal of Materials Science*, vol. 8, no. 12, pp. 823–827, 1997.
- [10] E. Lopez, B. Vidal, S. Berland, S. Camprasse, G. Camprasse, and C. Silve, “Demonstration of the capacity of nacre to induce bone formation by human osteoblasts maintained in vitro,” *Tissue and Cell*, vol. 24, no. 5, pp. 667–679, 1992.
- [11] C. Silve, E. Lopez, B. Vidal et al., “Nacre initiates biomineralization by human osteoblasts maintained in vitro,” *Calcified Tissue International*, vol. 51, no. 5, pp. 363–369, 1992.
- [12] M. J. Almeida, C. Milet, J. Peduzzi et al., “Effect of water-soluble matrix fraction extracted from the nacre of *Pinctada maxima* on the alkaline phosphatase activity of cultured fibroblasts,” *Journal of Experimental Zoology*, vol. 288, pp. 327–334, 2000.
- [13] M. Ni and B. D. Ratner, “Nacre surface transformation to hydroxyapatite in a phosphate buffer solution,” *Biomaterials*, vol. 24, no. 23, pp. 4323–4331, 2003.
- [14] Y. Shen, J. Zhu, H. Zhang, and F. Zhao, “In vitro osteogenic activity of pearl,” *Biomaterials*, vol. 27, no. 2, pp. 281–287, 2006.
- [15] M. Suzuki, K. Saruwatari, T. Kogure et al., “An acidic matrix protein, Pif, is a key macromolecule for nacre formation,” *Science*, vol. 325, no. 5946, pp. 1388–1390, 2009.
- [16] N. Kröger, “The molecular basis of nacre formation,” *Science*, vol. 325, no. 5946, pp. 1351–1352, 2009.
- [17] T. Kokubo and H. Takadama, “How useful is SBF in predicting in vivo bone bioactivity?” *Biomaterials*, vol. 27, no. 15, pp. 2907–2915, 2006.

Research Article

Fabrication of Novel Biodegradable α -Tricalcium Phosphate Cement Set by Chelating Capability of Inositol Phosphate and Its Biocompatibility

Toshiisa Konishi,^{1,2} Minori Mizumoto,² Michiyo Honda,²
Yukiko Horiguchi,³ Kazuya Oribe,³ Hikaru Morisue,⁴ Ken Ishii,^{2,4} Yoshiaki Toyama,⁴
Morio Matsumoto,^{2,4} and Mamoru Aizawa^{1,2}

¹ Department of Applied Chemistry, School of Science and Technology, Meiji University, 1-1-1 Higashimita, Tama-ku, Kawasaki 214-8571, Japan

² Kanagawa Academy of Science and Technology (KAST), KSP East 404, 3-2-1 Sakado, Takatsu-ku, Kawasaki 213-0012, Japan

³ Showa Ika Kohgyo Co., Ltd., 8-7 Hanei-nishimachi, Toyohashi 441-8026, Japan

⁴ Department of Orthopaedic Surgery, School of Medicine, Keio University, 35 Shinanomachi, Shinjuku-ku, Tokyo 160-8582, Japan

Correspondence should be addressed to Toshiisa Konishi; ap-konishi@newkast.or.jp

Received 8 April 2013; Accepted 8 May 2013

Academic Editor: Eng San Thian

Copyright © 2013 Toshiisa Konishi et al. This is an open access article distributed under the Creative Commons Attribution License, which permits unrestricted use, distribution, and reproduction in any medium, provided the original work is properly cited.

Biodegradable α -tricalcium phosphate (α -TCP) cement based on the chelate-setting mechanism of inositol phosphate (IP6) was developed. This paper examined the effect of the milling time of α -TCP powder on the material properties of the cement. In addition, biocompatibility of the result cement *in vitro* using osteoblasts and *in vivo* using rabbit models will be studied as well. The α -TCP powders were ballmilled using ZrO₂ beads in pure water for various durations up to 270 minutes, with a single-phase α -TCP obtained at ballmilling for 120 minutes. The resulting cement was mostly composed of α -TCP phase, and the compressive strength of the cement was 8.5 ± 1.1 MPa, which suggested that the cements set with keeping the crystallite phase of starting cement powder. The cell-culture test indicated that the resulting cements were biocompatible materials. *In vivo* studies showed that the newly formed bones increased with milling time at a slight distance from the cement specimens and grew mature at 24 weeks, and the surface of the cement was resorbed by tartrate-resistant acid phosphatase-(TRAP-)positive osteoclast-like cells until 24 weeks of implantation. The present α -TCP cement is promising for application as a novel paste-like artificial bone with biodegradability and osteoconductivity.

1. Introduction

Hydroxyapatite (Ca₁₀(PO₄)₆(OH)₂; HAp) has been used as bioceramics for bone grafting due to its biocompatibility and osteoconductivity. HAp is used clinically in the following forms: granule, dense ceramics, porous ceramics, and cement (paste-like artificial bone). In particular, the cement, that is, calcium-phosphate cement (CPC), has an advantage in that desired shape can be easily formed during surgery operation and has therefore received much attention [1–4].

CPCs generally consist of a mixture of a calcium-phosphate powder and an aqueous solution, and they are classified into two types. One type is based on hydrolysis of

α -tricalcium phosphate (α -Ca₃(PO₄)₂; α -TCP) put forward by Monma and Kanazawa [5]. The other type is based on acid-base reaction of tetracalcium phosphate (Ca₄O(PO₄)₂; TTCP) and acidic dicalcium phosphate dihydrate (CaHPO₄·2H₂O; DCPD) put forward by Brown and Chow [6]. Both CPCs are set by precipitation of calcium-deficient HAp (CDHA) or HAp; thus, they are stable in a host body for a long time [7].

We have developed a novel CPC using inositol phosphate (C₆H₆(OPO₃H₂)₆; IP6) as a chelating agent [8–11]. IP6 is found in wheat, rice, corn, and soybean [12], and it has a strong chelating capability to calcium ions, similar to chelating compounds such as ethylenediaminetetraacetic

acid (EDTA) [13]. The newly developed cement was created by mixing HAp powders that were surface modified with IP6 and suitable mixing solutions, and it could set by the chelate bonding of IP6. In addition, this cement showed excellent biocompatibility both *in vitro* and *in vivo* [11]. Meanwhile, we have previously developed biodegradable cement consisting of a single-phase β -TCP based on the chelate-setting mechanism of IP6, which was biodegradable and osteoconductive *in vivo* using rabbit models [14–16].

The order in relative dissolution of the calcium phosphates is α -TCP > β -TCP > HAp [17, 18]. Thereby, more soluble and reactive α -TCP than β -TCP is used mainly as a fine powder in hydraulic cement [5, 17, 18], and it is impossible to fabricate a single-phase α -TCP cement using neutral liquid component; that is, cement set with keeping a crystalline phase of starting reactant. Yamada et al. [19] have reported a histological and histomorphometrical study of porous β -TCP and α -TCP blocks as bone graft materials for augmenting alveolar ridges, in which the α -TCP block notably started degrading after 4 weeks, whereas degradation of β -TCP blocks had just begun at that time and scarcely progressed after 8 weeks. These results suggest that resorption of α -TCP is faster than that of β -TCP. Therefore, it is hypothesized that a novel biodegradable cement using more soluble α -TCP powder compared with β -TCP powder can develop on the basis of the chelate-setting mechanism of IP6, which will be a more biodegradable cement than β -TCP cement.

Our final goal is to develop injectable α -TCP cement with suitable mechanical property, biodegradability, and biocompatibility, on the basis of the chelate-setting mechanism of IP6. In this paper, the α -TCP cement based on chelate-setting mechanism of IP6 was fabricated. The α -TCP powders for cement fabrication were prepared by grinding and then modifying their surface with IP6, and mechanical property of the α -TCP cement was investigated in order to obtain the basic findings for development of injectable CPC. Moreover, biocompatibility of the α -TCP cement was examined *in vitro* using osteoblasts model and *in vivo* using rabbit models.

2. Materials and Methods

2.1. Preparation of the Ball-Milled α -TCP Powders and Their Surface Modification with IP6. The IP6 (50 mass % phytic acid, Wako Pure Chemical Industries, Ltd., Japan) solution was prepared with a concentration of 1000 ppm and was adjusted to pH 7.3 using an aqueous solution of NaOH (0.1 mol·dm⁻³). 10 grams of commercially available α -TCP powder (α -TCP-A, Taihei Chemical Industrial Co., Ltd., Japan) were ground using a planetary mill (Pulverisette 6, Fritsch, Germany) for 30, 60, 90, 120, 180, 240, and 270 minutes at a rotation rate of 300 rpm in a ZrO₂ pot with fifty 10 mm diameter ZrO₂ beads under wet conditions (40 cm³ of pure water). After ball-milling, the slurry mixtures were filtrated, and freeze-dried for 24 h to prepare ball-milled α -TCP powder without surface modification with IP6. To prepare the IP6 surface modified α -TCP powder, the filter cake obtained was added into the IP6 solution (400 cm³), stirred at 400 rpm for 24 h, filtrated, and freeze dried for 24 h.

Hereafter, samples are denoted according to the milling time; for example, the α -TCP powder ball-milled for 120 minutes is denoted as “ α -TCP120”, and the α -TCP120 powder surface modified with IP6 is denoted as “IP6- α -TCP120”. The as-received α -TCP-A powder is denoted as “ α -TCP0”.

2.2. Characterization of the Prepared α -TCP Powders. X-ray diffraction (XRD; Ultima IV, Rigaku, Japan) analysis of the powders was conducted using a CuK α radiation source. Data were collected in the range of $2\theta = 25 - 40^\circ$ with a step size of 0.02° and counting time of 1.2 s/step. The crystal phase was identified with respect to the JCPDS reference patterns for α -TCP (#09-0348) and HAp (#09-0432). The HAp content in the α -TCP powders with and without IP6 surface modification was calculated using the typical peaks of α -TCP ($2\theta = 30.75^\circ$) and HAp ($2\theta = 31.77^\circ$) by (1) as follows:

$$\text{HAp content (\%)} = \frac{I_{\text{HAp}(t)}}{I_{\alpha\text{-TCP}(t)} + I_{\text{HAp}(t)}} \times 100, \quad (1)$$

where $I_{\alpha\text{-TCP}(t)}$ and $I_{\text{HAp}(t)}$ are the XRD intensities of the α -TCP ($2\theta = 30.75^\circ$) and HAp ($2\theta = 31.77^\circ$) in the ball-milled powder for t min ($t = 0 - 270$), respectively. The crystallite size of the ball-milled α -TCP powders was calculated using Scherrer's equation:

$$\text{Crystallite size (nm)} = \frac{K\lambda}{\beta \cos \theta}, \quad (2)$$

where K is the shape coefficient ($K = 0.9$), λ is the wavelength ($\lambda = 0.15405$ nm), and β is the half width at $2\theta = 30.75^\circ$.

The specific surface area and median particle size of the ball-milled α -TCP powders were measured with a surface area analyzer (Flowsorb III, Shimadzu, Japan) and a laser particle size analyzer (LA-300, Horiba, Japan), respectively. The particle morphology of the ball-milled α -TCP sputter coated with Au was observed with a scanning electron microscope (SEM; VE-9800, Keyence, Japan) at an accelerating voltage of 10 kV.

Dissolution of Ca²⁺ ions released from the ball-milled α -TCP powder with and without IP6 surface modification was measured using ion-selective potentiometry (F-73, Horiba, Japan). Twenty-five milligrams of each α -TCP powder were added to 0.2 dm³ of 0.05 mol·dm⁻³ tris (hydroxymethyl) aminomethane hydrochloric acid (Tris-HCl) buffer at pH 7.3 and 25 ± 3°C with stirring at 430 rpm. The concentration of free Ca²⁺ ions in the solution was measured as a function of time up to 180 minutes.

2.3. Fabrication of the α -TCP Cement Specimens and Their Material Properties. Cement specimens were fabricated by mixing 0.25 g of prepared α -TCP powder with and without surface modification with IP6 and pure water at powder/liquid (P/L) ratio of 1/0.40 [g/cm³], and packing into a 5 mm diameter cylindrical stainless mold. The resulting cement specimens (5 mm in diameter, 7 mm in height) were kept at room temperature for 24 h.

The compressive strength of the cement specimens was measured using a universal testing machine (Autograph

AGS-X, Shimadzu, Japan) with a 5 kN load cell at a crosshead speed of $500 \mu\text{m}\cdot\text{min}^{-1}$. XRD patterns of the cement after the compressive strength testing were measured to determine the HAp content after setting for 24 h, and the HAp content in the cement specimen was also calculated by (1). The microstructure of the fracture cement sputter coated with Au was observed with SEM at an accelerating voltage of 10 kV. The bulk density of the cylindrical cement specimens was calculated by measuring the diameter, height, and weight of the cement. The relative density of the cement specimen was calculated from the bulk density divided by the theoretical density of α -TCP/HAp, which was calculated by (3) as follows:

$$\begin{aligned} & \text{Theoretical density of } \alpha\text{-TCP/HAp (g/cm}^3\text{)} \\ &= \frac{2.86 \times (100 - \text{HAp content (\%)})}{100} \\ &+ \frac{3.16 \times (\text{HAp content (\%)})}{100}, \end{aligned} \quad (3)$$

where 2.86 and 3.16 [g/cm^3] are theoretical density of the α -TCP and HAp, respectively.

2.4. In Vitro Evaluation of the α -TCP Cement Specimens. In order to evaluate the biocompatibility of the cement specimens, we have compared cell proliferation between polystyrene plate (control) and cement specimens (both α -TCP120 and IP6- α -TCP120). The IP6- α -TCP120 cement with the highest compressive strength and the lowest HAp contents was selected, which would be expected as the most biodegradable material.

The cement specimens for *in vitro* evaluation were prepared by mixing the α -TCP powder and pure water at P/L ratio of 1/0.4 [g/cm^3], and packing into a cylindrical stainless mold. The resulting cement specimens (5 mm in diameter, 7 mm in height) were kept at room temperature under atmospheric conditions for 24 h, and they were sterilized with ethylene oxide gas (EOG).

Osteoblast-like cells (MC3T3-E1) were seeded into 12 well tissue culture plates at a density of 6×10^4 cells/well and precultured for 1 day. The cement specimens were then set on a membrane of Transwell kit (Corning, USA) to culture the cells in a humidified 5% CO_2 balanced-air incubator at 37°C . The number of proliferated cells was counted after culturing for 1, 2, and 4 days.

2.5. In Vivo Evaluation of the α -TCP Cement Specimens. Based on *in vitro* cell proliferation assay, biodegradability and biocompatibility of the IP6- α -TCP120 cement specimens *in vivo* were evaluated.

In vivo studies of the IP6- α -TCP120 cement specimens were performed using 16-week-old male rabbits (average weight: 3 kg) according to the guidelines of the laboratory animal center at Keio University. The cement specimens for *in vivo* evaluation were prepared in the same manner as described in Section 2.4. The dimensions of the resulting cement specimens were 4 mm in diameter and 7 mm in height. The cement specimens were sterilized with EOG.

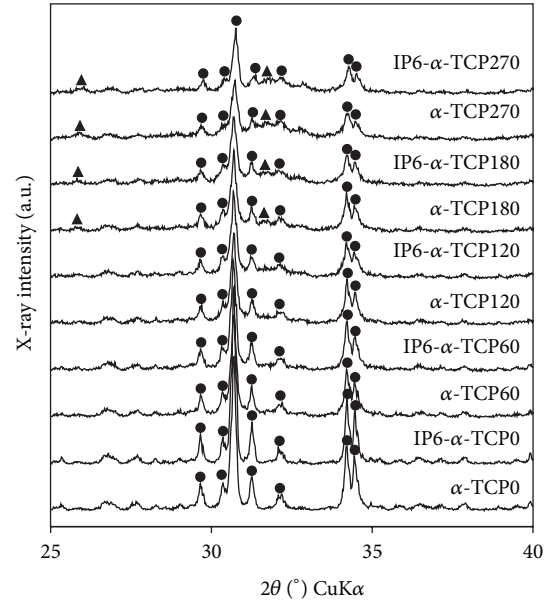


FIGURE 1: XRD patterns of the prepared α -TCP powders with and without IP6 surface modification. Closed circles indicated typical α -TCP peaks, and closed triangles indicated typical HAp peaks. The single-phase α -TCP was maintained up to 120 minutes of milling, and the α -TCP powders over 120 minutes of milling were composed of both α -TCP and HAp phases.

A cylindrical defect (4.4 mm diameter) was drilled in the epiphysis of a rabbit's tibia. The cement specimen was implanted into the defect for 4, 8, and 24 weeks. At appropriate period, the rabbit was sacrificed using sodium pentobarbital and the tibia was removed. Decalcified and undecalcified sections were then prepared for histological evaluation. The decalcified sections were stained with tartrate-resistant acid phosphatase (TRAP) and the undecalcified sections were stained with hematoxylin and eosin (HE). The histological sections were observed with an upright microscope (BX41, Olympus, Japan).

2.6. Statistical Analysis. A *t*-test was used to determine whether any significant differences existed between the mean values of the experimental groups. A difference between groups was considered to be significant at $P < 0.05$.

3. Results

3.1. Characterization of the Prepared α -TCP Powders. Typical XRD patterns, crystallite size, and HAp content of the prepared α -TCP powders were shown in Figures 1 and 2, respectively. The XRD patterns of the as-received α -TCP powder (α -TCP0) and the IP6 surface modified powder (IP6- α -TCP0) showed that α -TCP had a single phase with high crystallinity. The XRD patterns of the α -TCP powders ball milled up to 120 minutes and their surface-modified powders showed mostly α -TCP phase.

In Figure 2, the crystallite size of the prepared α -TCP powders with and without IP6 surface modification

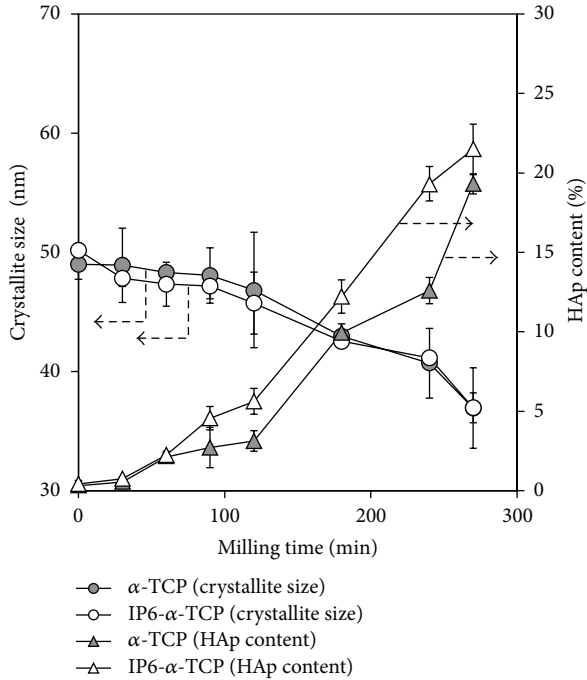


FIGURE 2: Crystallite size and HAp content of the prepared α -TCP powders with and without IP6 surface modification as a function of milling time. Error bars indicated standard error of the mean ($n = 3$). The crystallite size of the prepared α -TCP powders with and without IP6 surface modification decreased with milling time, and HAp contents of the prepared α -TCP powders with and without IP6 surface modification increased with milling time.

decreased with milling time, and the prepared α -TCP powders were composed of nanosized α -TCP crystals less than 50 nm. Although the α -TCP180 and IP6- α -TCP180 powders were mostly composed of α -TCP phase, small amount of HAp phase was contained: $9.9 \pm 0.6\%$ for the α -TCP180 and $12.2 \pm 1.1\%$ for the IP6- α -TCP180. The HAp contents in the IP6 surface modified α -TCP powders over 90 minutes of ball milling were more than those of the α -TCP powders without IP6 surface modification, which suggested that the α -TCP powders without IP6 surface modification were hydrolyzed during IP6 surface modification.

Specific surface area and median particle size of the prepared α -TCP powders were shown in Figure 3. Specific surface area of the α -TCP powders up to 120 minutes of ball milling did not change before and after IP6 surface modification; however, that of the IP6 surface modified α -TCP powders over 180 minutes of milling was higher than that of the α -TCP powders before IP6 surface modification. The results corresponded to the increase in HAp contents of IP6 surface modified α -TCP powders over 180 minutes of milling in Figure 2. Median particle size of the prepared α -TCP powders decreased with increasing milling time, and that of the prepared α -TCP powders with and without IP6 surface modification did not change. Although the median particle size of IP6- α -TCP0 powder was about $9.2 \pm 0.2 \mu\text{m}$, that of IP6- α -TCP120 powder composed of a single phase α -TCP decreased to approximately $3.1 \pm 0.04 \mu\text{m}$.

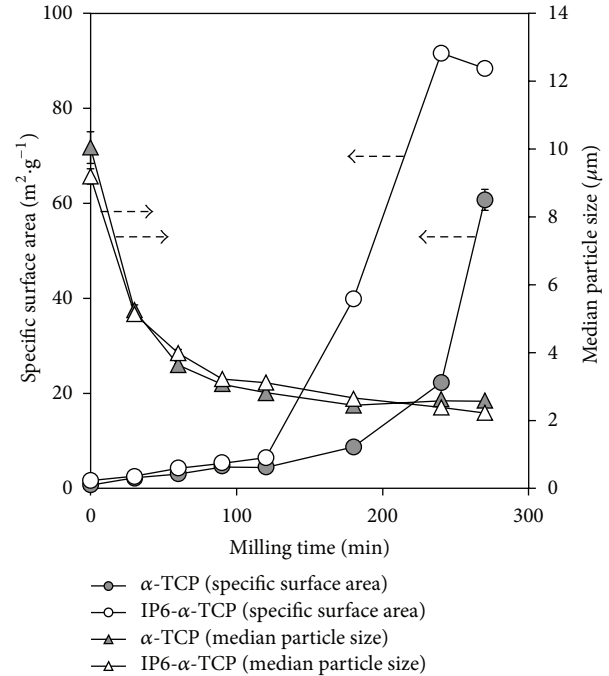


FIGURE 3: Specific surface area and median particle size of the prepared α -TCP powders with and without surface modification as a function of milling time. Error bars indicated standard error of the mean ($n = 3$). The specific surface area of the α -TCP powders up to 120 minutes of ball milling did not change before and after IP6 surface modification; however, that of the IP6 surface modified α -TCP powders over 180 minutes of milling was higher than that of the α -TCP powders before IP6 surface modification. Median particle size of the prepared α -TCP powders decreased with increasing milling time.

Figure 4 showed particle morphology of the prepared α -TCP powders. In Figures 4(a) and 4(b), the α -TCP0 and IP6- α -TCP0 powders were tens of microns of grains; however, the particle size of the α -TCP powders decreased with increasing milling time (Figures 4(c)–4(h)). The results were consistent with the decrease in median particle size and crystallite size of the prepared α -TCP powders. The α -TCP180 and IP6- α -TCP180 powders were composed of small particles and aggregates as indicated by arrows (Figures 4(g) and 4(h)), and in highly magnification images these aggregates were composed of needle-shaped crystals (data not shown). In addition, no obvious difference in the particle morphology with and without IP6 surface modification was observed.

The dissolution of Ca^{2+} ions from the prepared α -TCP powders was shown as a function of time up to 180 minutes (Figure 5). Dissolution of the IP6- α -TCP powders was lower than that of α -TCP powders without IP6 surface modification, whereas dissolution of the α -TCP powders with and without IP6 surface modification increased with milling time.

3.2. Evaluation of the α -TCP Cement Specimens. XRD patterns of the cement specimens, after setting for 24 h, fabricated from the α -TCP powders with and without IP6 surface

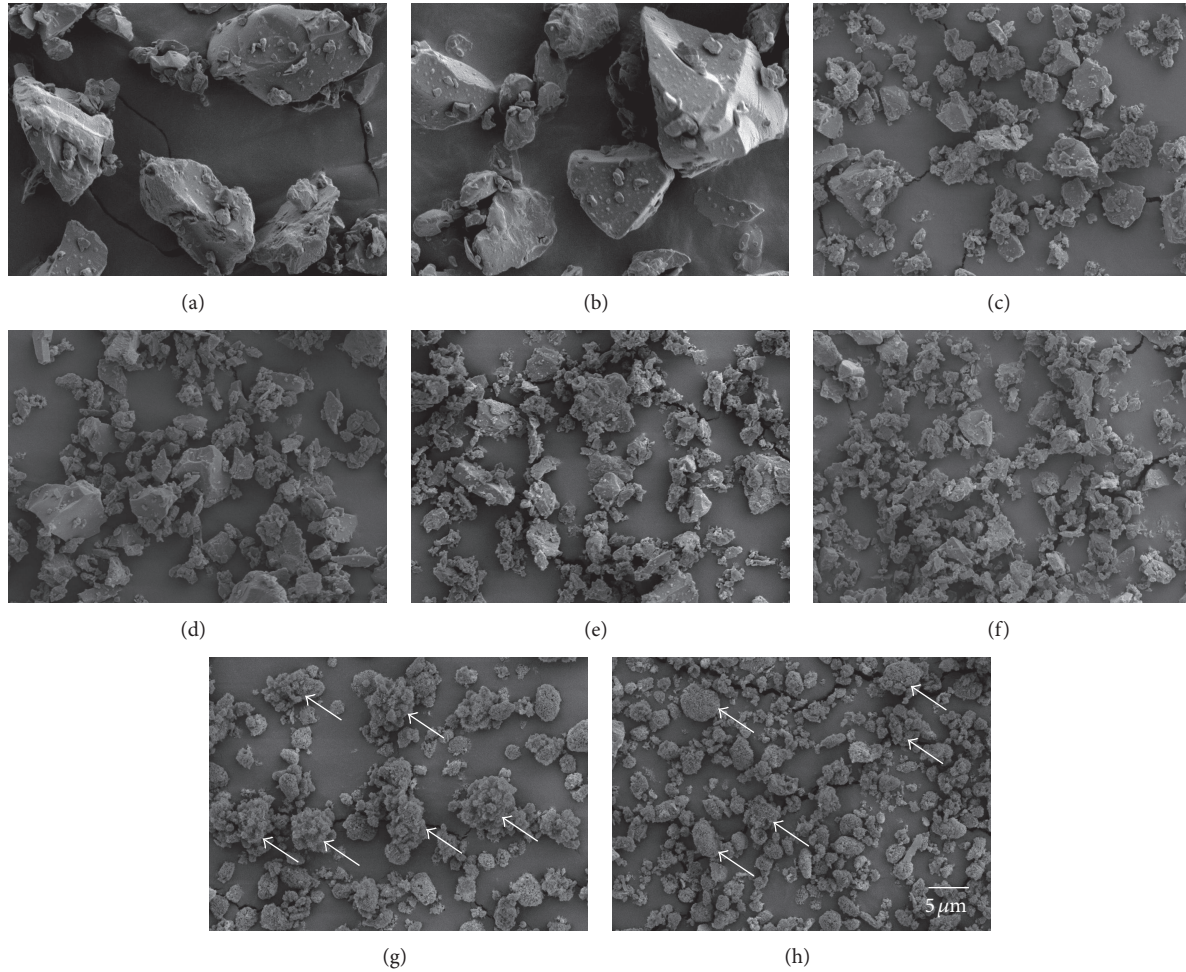


FIGURE 4: Particle morphology of the prepared α -TCP powders: (a) α -TCP0, (b) IP6- α -TCP0, (c) α -TCP60, (d) IP6- α -TCP60, (e) α -TCP120, (f) IP6- α -TCP120, (g) α -TCP180, and (h) IP6- α -TCP180. In (a) and (b), the α -TCP0 and IP6- α -TCP0 powders were tens of microns of grains; however, the particle size of the α -TCP powders decreased with increasing milling time ((c)–(h)). The α -TCP180 and IP6- α -TCP180 powders were composed of small particles and aggregates as indicated by arrows ((g) and (h)).

modification at the $P/L = 1/0.40$ [g/cm^3] were measured, and HAp content of those cement specimens was calculated using (1) (Figure 6). The XRD patterns of α -TCP0, α -TCP60, and α -TCP120 cement specimens with and without IP6 surface modification showed mostly α -TCP phase, whereas HAp contents in those cement specimens slightly increased with milling time and were more than those in the starting cement powders. The HAp contents in the α -TCP180 and IP6- α -TCP180 cement specimens were two times more than those in other cement specimens. The HAp contents in the IP6- α -TCP120 and IP6- α -TCP180 cement specimens were significantly more than those in the α -TCP120 and α -TCP180 cement specimens, respectively ($P < 0.05$).

The compressive strength and relative density of the cement specimens fabricated from the α -TCP powders with and without IP6 surface modification were shown in Figure 7. The maximum compressive strength of the IP6- α -TCP cement specimens mostly composed of α -TCP phase was 8.5 ± 1.1 MPa for the IP6- α -TCP120 cement specimen. In contrast, the compressive strength of the α -TCP180 cement

specimens composed of α -TCP/HAp biphasic was significantly higher (19.0 ± 2.7 MPa) than that of IP6- α -TCP180 cement specimens ($P < 0.05$). No significant difference in the relative density between the α -TCP and IP6- α -TCP cement specimens was confirmed.

Figures 8(a) and 8(e) showing the microstructure of fracture cement provided many voids among the grains in the fracture surface. In Figures 8(b)–8(d) and 8(f)–8(h), small particles packed among the grains were observed, and small particles increased with milling time. No obvious difference in the microstructure of fracture cement between α -TCP and IP6- α -TCP cement specimens was observed.

Next, in order to evaluate the biocompatibility of the cement specimens, we have compared cell proliferation between polystyrene plate and cement specimens (α -TCP120 and IP6- α -TCP120). We have selected the IP6- α -TCP120 cement with the highest compressive strength, and lowest HAp contents among the single-phase α -TCP cements were selected, because that would be expected as the most biodegradable material.

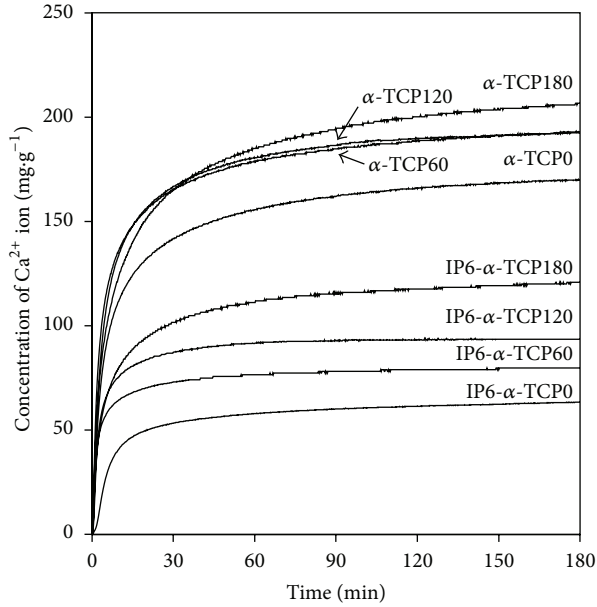


FIGURE 5: Dissolution of Ca^{2+} ions from the prepared α -TCP powders with and without IP6 surface modification. Dissolution of the IP6- α -TCP powders was lower than that of α -TCP powders without IP6 surface modification.

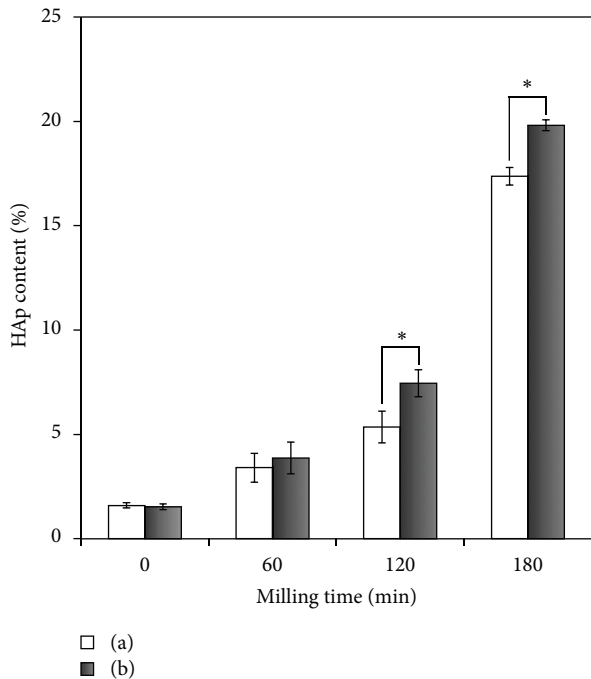


FIGURE 6: HAp content of the cement specimens after setting for 24 h, fabricated from the α -TCP powders with (a) and without (b) IP6 surface modification at $P/L = 1/0.40$ [g/cm^3]. Error bars indicated standard error of the mean ($n = 3$). The asterisks (*) showed that $P < 0.05$ by t test. HAp contents in α -TCP0, α -TCP60, and α -TCP120 cement specimens with and without IP6 surface modification slightly increased with milling time and were more than those in the starting cement powders. The HAp contents in the α -TCP180 and IP6- α -TCP180 cement specimens were two times more than those in other cement specimens.

3.3. *In Vitro Evaluation of the α -TCP Cement Specimens.* Figure 9 showed cell proliferation cocultured with the α -TCP120 and IP6- α -TCP120 cement specimens using Transwell kit. In comparison with cell proliferation of control (polystyrene plate) and α -TCP120 cement, no significant differences between control and α -TCP120 cement was observed. The results suggested that any component from α -TCP120 cement, which affected the cell proliferation, did not release into a medium.

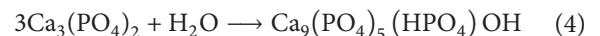
Next, in order to evaluate whether IP6 surface modification affected cell proliferation or not, cell proliferation assay using IP6- α -TCP120 cement was performed. The cell proliferation co-cultured with IP6- α -TCP120 cement was comparable with that of α -TCP120 cement, and no significance in the cell proliferation between α -TCP120 and IP6- α -TCP120 cements was confirmed. This indicated that IP6 surface modification did not have effects on the cell proliferation, and both the α -TCP120 and IP6- α -TCP120 cements were biocompatible materials.

3.4. *In Vivo Evaluation of the α -TCP Cement Specimens.* As a result of *in vitro* evaluation, no obvious changes in cell proliferation co-cultured with and without cement specimens were seen for each time point (Figure 9). Following the *in vitro* study, *in vivo* biodegradability and biocompatibility of the IP6- α -TCP120 cement specimen were evaluated due to their excellent cell proliferation *in vitro*.

Histological observation of the IP6- α -TCP120 cement specimens after 4, 8, and 24 weeks of implantation was performed using HE (Figures 10(a)–10(f)) and TRAP (Figures 10(g)–10(i)) stainings. Low-magnification images (Figures 10(a)–10(c)) showing the entire cement specimens (C) were not directly in contact with newly-formed bones (N). Figures 10(d)–10(f) showed high-magnification images of the areas indicated by dotted-line squares in Figures 10(a)–10(c), respectively, where the newly formed bones were evident by light pink staining and those increased with milling time at a slight distance from the cement specimens and grew mature at 24 weeks. In the areas of the newly formed bones, aligning osteoblast-like cells (arrows) forming the newly formed osteoids were confirmed in all of the implant periods (Figures 10(d)–10(f)). Meanwhile, TRAP-positive osteoclast-like cells (asterisk) on the surface of the cement specimen resorbing the cement specimens were observed throughout all of the implant periods (Figures 10(g)–10(i)). Rate of resorption, which was calculated from the sectional areas of the cement specimens before and after implantation for 4, 8, and 24 weeks using Figures 10(a)–10(c), was 13.7%, 14.1%, 16.2%, respectively.

4. Discussion

It is well known that α -TCP could be hydrolyzed, resulting in forming a CDHA as indicated by (4) [5, 20, 21] as follows:



The α -TCP was used as a solid component of the CPC because of its high reactivity, and, final product of the CPC

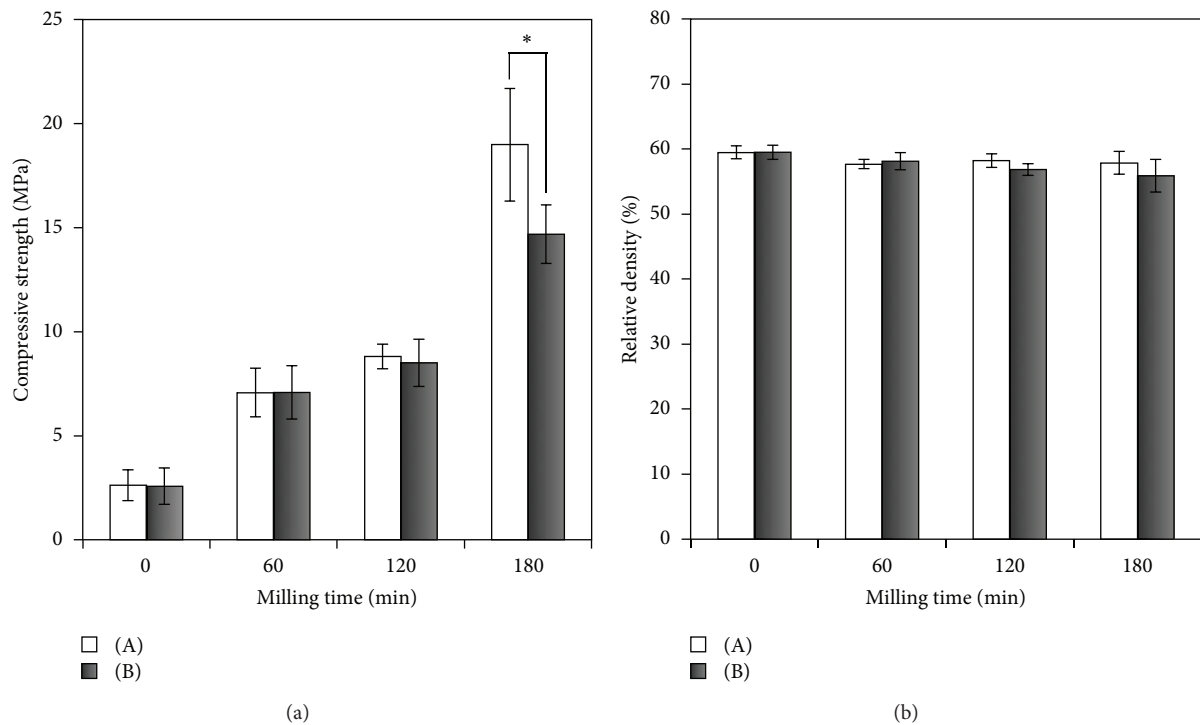


FIGURE 7: Compressive strength (a) and relative density (b) of the cement specimens after setting for 24 h, fabricated from the α -TCP powders with (A) and without (B) IP6 surface modification at $P/L = 1/0.40$ [g/cm^3]. Error bars indicated standard error of the mean ($n = 3$). The asterisk (*) showed that $P < 0.05$ by t test. The maximum compressive strength of the IP6- α -TCP cement specimens mostly composed of α -TCP phase was 8.5 ± 1.1 MPa for the IP6- α -TCP120 cement specimen; whereas, the compressive strength of the α -TCP180 cement specimens composed of α -TCP/HAp biphasic was the highest (19.0 ± 2.7 MPa).

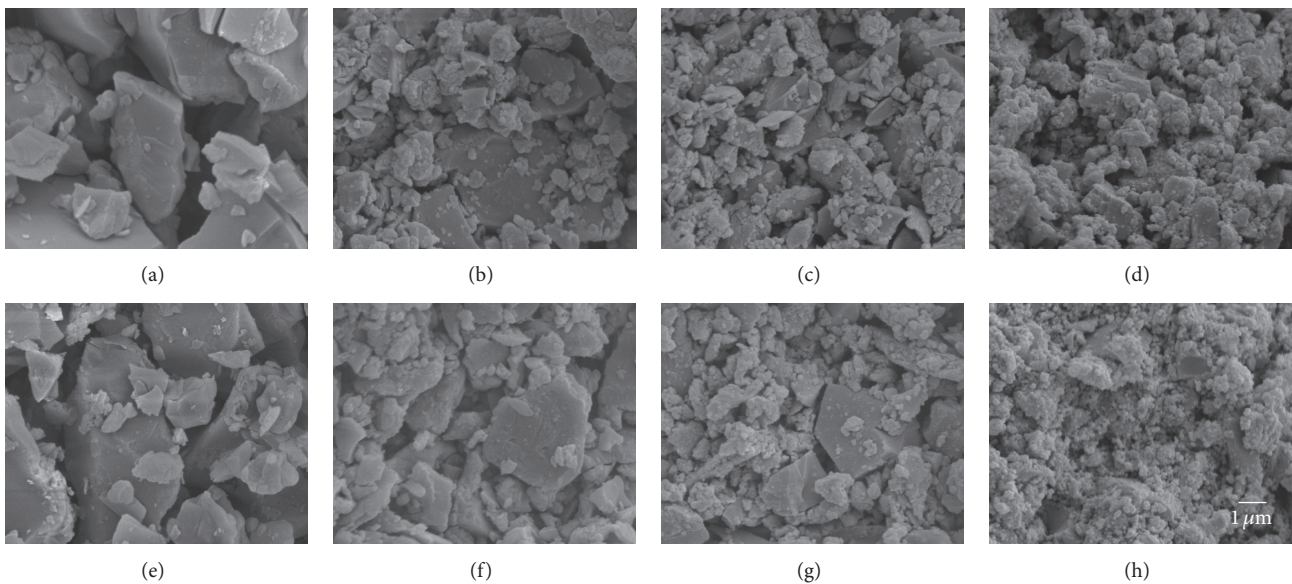


FIGURE 8: Microstructure of fractured cement surface, fabricated from the α -TCP powders with and without IP6 surface modification at $P/L = 1/0.40$ [g/cm^3]: (a) α -TCP0, (b) α -TCP60, (c) α -TCP120, (d) α -TCP180, (e) IP6- α -TCP0, (f) IP6- α -TCP60, (g) IP6- α -TCP120, and (h) IP6- α -TCP180. (a) and (e) provided many voids among the grains in the fracture surface. (b)–(d) and (f)–(h) showed small particles packed among the grains, and small particles increasing with milling time.

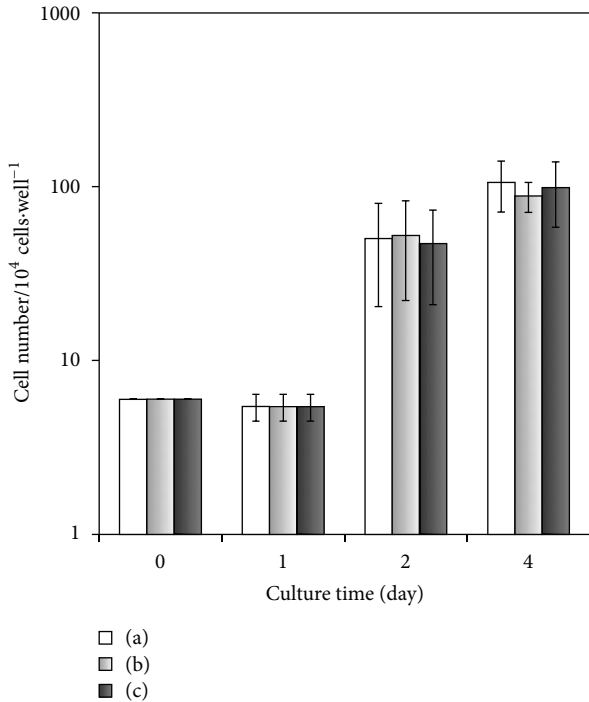


FIGURE 9: Cell proliferation co-cultured with the α -TCP120 and IP6- α -TCP120 cement specimens using Transwell kit: (a) control (polystyrene plate), (b) α -TCP120 ($P/L = 1/0.40$ [g/cm^3]), and (c) IP6- α -TCP120 ($P/L = 1/0.40$). The cement specimens were set on the membrane of Transwell after the cells were cultured for 24 h. Error bars indicated standard error of the mean ($n = 3$). The cell proliferation of polystyrene plate and two kinds of cement specimen was almost the same level, and no significant differences among them were observed.

was CDHA [22–24]. In order to adjust the particle size of α -TCP as a solid component of the CPC, the α -TCP was mechanically ball milled for appropriate periods [23–27]. Moreover, it was reported that the mechanically ball-milled α -TCP caused decrease in XRD intensities of α -TCP, and led to transformation from crystalline to amorphous state [23–27]. The decrease in XRD intensities and crystallite size of the α -TCP powders was confirmed with increasing of milling time (Figures 1 and 2), implying that the ball milled α -TCP powders contained the amorphous phase in part.

Most of α -TCP phase was maintained up to 120 minutes of milling, and the α -TCP powders over 120 minutes of milling were composed of the both α -TCP and HAp phases (Figure 1). The phase transformation of α -TCP to HAp in milling duration of 120 minutes and longer was due to hydrolysis of the α -TCP during ball-milling, which was evident by the increase in HAp content and specific surface area. In the previous report by Gbureck et al. [23], they showed that prolonged ball-milling of α -TCP did not lead to α -TCP and HAp biphasic but amorphous α -TCP in XRD pattern. They used a 99.9% of ethanol as a milling solvent; however, we used pure water as a milling solvent in this paper. Consequently, the α -TCP was hydrolyzed in pure water over 120 minutes of milling.

The particle size of the prepared IP6- α -TCP powders decreased with increasing milling time. As a consequence, the dissolution of the α -TCP powders with and without IP6 surface modification also increased. The results suggested that the decrease in particle size was dominant for dissolution of the α -TCP powders. In addition, IP6 can chelate with Ca^{2+} ions, as previously reported [28, 29]; thus, the adsorption of IP6 on the surface of α -TCP powders may inhibit the dissolution of α -TCP itself. As a result, the dissolution of the IP6- α -TCP powders was lower than that of α -TCP powders without IP6 surface modification, as shown in Figure 5. However, no direct evidence could be obtained that the IP6 was surface modified successfully. Because of low IP6 concentration used in this paper (1000 ppm), it was not detected by Fourier transform infrared spectroscopic analysis. Therefore, further analysis will be necessary for detection of IP6 on the surface of α -TCP.

The α -TCP cement based on chelating mechanism of IP6 was developed for the first time in this paper. The compressive strength of the α -TCP cement specimens with and without IP6 surface modification increased with milling time; however, the relative density of these cement specimens did not change and HAp contents of these cement specimens, excluding α -TCP180 and IP6- α -TCP180, also did not change compared to those of the cement powders. Increase in compressive strength of the α -TCP cement specimens was due to decrease in particle size of α -TCP powders, which was evident by increase in packing degree of the α -TCP powders in Figure 8. However, difference in the relative density of the cement specimens was not observed because of small change in the compressive strength. Furthermore, the cement specimens were fabricated with high P/L ratio (1/0.40 [g/cm^3]) and the α -TCP powders were barely hydrolyzed during setting of the cements; therefore, no change in HAp contents of α -TCP cement specimens, except for α -TCP180 and IP6- α -TCP180, was observed. Significances in the HAp contents between α -TCP120 and IP6- α -TCP120 and α -TCP180 and IP6- α -TCP180 were because of the higher HAp contents in the IP6- α -TCP120 and IP6- α -TCP180 powders than those of the α -TCP120 and α -TCP180 powders as shown in Figure 2. The HAp contents in α -TCP180 and IP6- α -TCP180 cement specimens were more than those of other cement specimens, and the compressive strength of the α -TCP180 cement specimen was significantly more than that of α -TCP180 cement specimen. The results indicated that the α -TCP180 and IP6- α -TCP180 powders were slightly hydrolyzed during setting of the cements. As a consequence, enhancement in compressive strength of these two cement specimens was not presumably caused by only increase in HAp contents but also entanglement of each particle and chelate-bonding of IP6. However, obvious needle-shaped or plate-shaped crystals formed by hydrolysis of the α -TCP, as reported by TenHuisen and Brown [21] and Ginebra et al. [22], were not observed in the microstructures (Figure 8).

Regarding *in vitro* evaluation of HAp cements, we have previously elucidated that IP6 surface modification of the HAp particles with 1000 ppm IP6 did not affect the biocompatibility of the cement specimen *in vitro* [8, 11]. The present cell-culture test using Transwell kit (Figure 9) indicated that

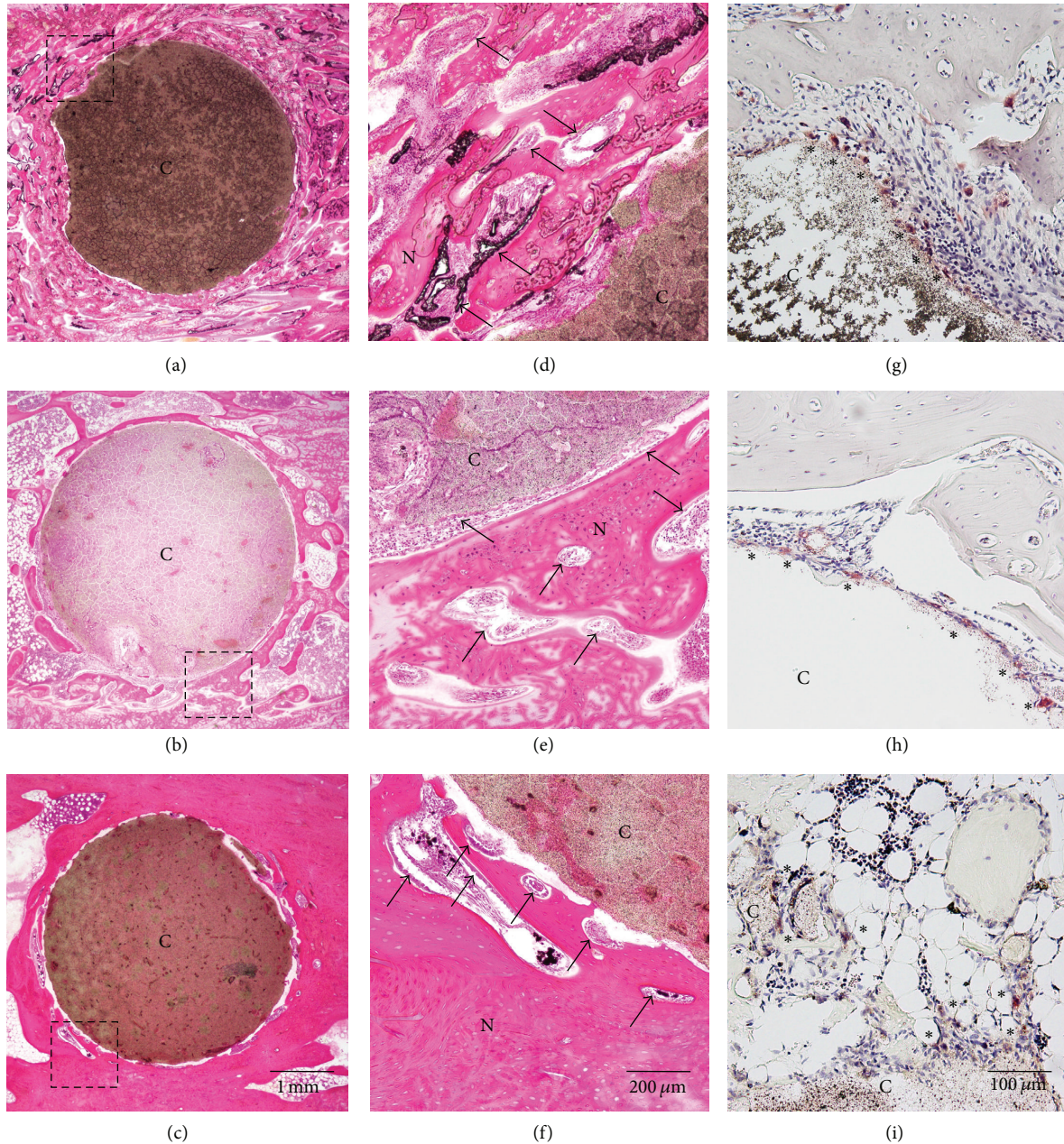


FIGURE 10: Histological sections showing IP6- α -TCP120 ($P/L = 1/0.40$ [g/cm^3]) cement specimens implanted into the rabbit tibia. (a)–(f): undecalcified sections stained with HE; (g)–(i): decalcified sections stained with TRAP. (a), (d), and (g): 4 weeks of implantation; (b), (e), and (h): 8 weeks of implantation; (c), (f), and (i): 24 weeks of implantation. The low-magnification images (a)–(c) showed the entire cement specimen (C), and (d)–(f) presented high-magnification images of the dotted square areas shown in (a)–(c), respectively, where the newly formed bones were evident by light pink staining. The arrows in (d)–(f) indicated aligning osteoblast-like cells forming the newly formed bones (N). The asterisks (*) in (g)–(i) represented TRAP-positive osteoclast-like cells resorbing the cement.

there was no significance in cell proliferation between α -TCP cements with and without IP6 surface modification, and both α -TCP cements did not affect the biocompatibility.

In vivo studies indicated that the newly formed bones increased with milling time at a slight distance from the cement specimens and grew mature at 24 weeks (Figures 10(d)–10(f)). The surface of the IP6- α -TCP120 cement specimens was resorbed by TRAP-positive osteoclast-like cells (Figures 10(g)–10(i)) throughout all of the implant periods.

The biological behavior of α -TCP has previously been studied in several *in vivo* studies [19, 30–34]; however, no report existed about α -TCP-based cement composed of α -TCP phase, because α -TCP was used as the solid component of hydraulic CPC [5, 17, 18]. Kihara et al. [33] reported that, in the implantation of α -TCP particles (~ 300 μm diameter) into cranial bone defects in rabbits, a “reticulate structure” was developed among the α -TCP particles after 1 week as a consequence of the degradation of α -TCP, and newly formed

bone was observed after 8 weeks. Yamada et al. [19] conducted a histological and histomorphometrical study of porous α -TCP blocks as bone graft material for augmenting alveolar ridges. The α -TCP block notably started degrading after 4 weeks, and was severely degraded after 8 weeks. Residual α -TCP particles surrounded by newly formed bone decreased over time, and both particles and newly formed bone were simultaneously resorbed by osteoclast-like cells. Both reports suggested that the α -TCP ceramics were potential biodegradable material. In this paper, the resorption of the cement specimens by osteoclast-like cells was observed throughout all of the implant periods; however, most of the cements (83.8%) remained even after 24 weeks of implantation. Oonishi et al. reported that α -TCP granules with 300 μm in diameter were mostly resorbed after 12 weeks of implantation in the rabbit model [31]. The present IP6- α -TCP120 cements were relatively dense ($56.8 \pm 0.9\%$ of relative density) with no interconnected pores in the cement, and they could be resorbed chemically and biologically only from the surface of the cement. Thus, the resorption rate of the IP6- α -TCP cement was slow. Furthermore, less dissolution of the IP6- α -TCP120 powder than that of the α -TCP120 powder as shown in Figure 5 suggested that the IP6- α -TCP120 cement was less soluble than the α -TCP120 cement. Therefore, long-term studies will be necessary to evaluate the complete degradability of the cement.

5. Conclusions

The single-phase α -TCP powder for fabrication of IP6- α -TCP cement was obtained by ball milling of α -TCP for 120 min. The resulting cement, which was fabricated by mixing the IP6- α -TCP120 and pure water, was mostly composed of α -TCP phase, and the compressive strength of the cement was 8.5 ± 1.1 MPa, which suggested that the cements set with keeping the crystallite phase of starting cement powder. The enhancement in the compressive strength with milling time was achieved by a decrease in particle size of the cement powders. *In vitro* cell-culture test indicated biocompatibility of the cement. *In vivo* studies showed that the newly formed bones increased with milling time at a slight distance from the cement specimens and grew mature at 24 weeks, and the surface of the cement was resorbed by TRAP-positive osteoclast-like cells up till 24 weeks of implantation. The present IP6- α -TCP cement with biodegradability and biocompatibility is a promising candidate for application as a novel paste-like artificial bone.

Conflict of Interests

None of the authors have any conflict of interests associated with this paper.

References

- [1] K. Ishikawa, S. Takagi, L. C. Chow, and Y. Ishikawa, "Properties and mechanisms of fast-setting calcium phosphate cements," *Journal of Materials Science*, vol. 6, no. 9, pp. 528–533, 1995.

- [2] U. Gbureck, J. E. Barralet, K. Spatz, L. M. Grover, and R. Thull, "Ionic modification of calcium phosphate cement viscosity. Part I: hypodermic injection and strength improvement of apatite cement," *Biomaterials*, vol. 25, no. 11, pp. 2187–2195, 2004.
- [3] J. E. Barralet, M. Tremayne, K. J. Lilley, and U. Gbureck, "Modification of calcium phosphate cement with α -hydroxy acids and their salts," *Chemistry of Materials*, vol. 17, no. 6, pp. 1313–1319, 2005.
- [4] Y. Miyamoto, K. Ishikawa, M. Takechi et al., "Histological and compositional evaluations of three types of calcium phosphate cements when implanted in subcutaneous tissue immediately after mixing," *Journal of Biomedical Materials Research A*, vol. 48, pp. 36–42, 1999.
- [5] H. Monma and T. Kanazawa, "The hydration of α -tricalcium phosphate," *Yogyo-Kyokai-Shi*, vol. 84, pp. 209–213, 1976.
- [6] W. E. Brown and L. C. Chow, "Dental restorative cement pastes," US Patent No. US4518430, 1985.
- [7] D. Apelt, F. Theiss, A. O. El-Warrak et al., "*In vivo* behavior of three different injectable hydraulic calcium phosphate cements," *Biomaterials*, vol. 25, no. 7-8, pp. 1439–1451, 2004.
- [8] M. Aizawa, Y. Haruta, and I. Okada, "Development of novel cement processing using hydroxyapatite particles modified with inositol phosphate," in *Archives of BioCeramics Research*, vol. 3, pp. 134–138, 2003.
- [9] Y. Horiguchi, A. Yoshikawa, K. Oribe, and M. Aizawa, "Fabrication of chelate-setting hydroxyapatite cements from four kinds of commercially-available powder with various shape and crystallinity and their mechanical property," *Nippon Seramikkusu Kyokai Gakujutsu Ronbunshi*, vol. 116, no. 1349, pp. 50–55, 2008.
- [10] T. Konishi, Z. Zhuang, M. Mizumoto, M. Honda, and M. Aizawa, "Fabrication of chelate-setting cement from hydroxyapatite powder prepared by simultaneously grinding and surface-modifying with sodium inositol hexaphosphate and their material properties," *Journal of the Ceramic Society of Japan*, vol. 120, pp. 1–7, 2012.
- [11] T. Konishi, Y. Horiguchi, M. Mizumoto et al., "Novel chelate-setting calcium-phosphate cements fabricated with wet-synthesized hydroxyapatite powder," *Journal of Materials Science*, vol. 24, pp. 611–621, 2013.
- [12] T. H. Dao, "Polyvalent cation effects on myo-inositol hexakis dihydrogenphosphate enzymatic dephosphorylation in dairy wastewater," *Journal of Environmental Quality*, vol. 32, no. 2, pp. 694–701, 2003.
- [13] C. J. Martin and W. J. Evans, "Phytic acid-metal ion interactions. II. The effect of pH on Ca(II) binding," *Journal of Inorganic Biochemistry*, pp. 2717–2730, 1986.
- [14] S. Takahashi, T. Konishi, K. Nishiyama et al., "Fabrication of novel bioresorbable β -tricalcium phosphate cement on the basis of chelate-setting mechanism of inositol phosphate and its evaluation," *Nippon Seramikkusu Kyokai Gakujutsu Ronbunshi/Journal of the Ceramic Society of Japan*, vol. 119, no. 1385, pp. 35–42, 2011.
- [15] T. Konishi, S. Takahashi, M. Mizumoto, M. Honda, K. Oribe, and M. Aizawa, "Effect of the addition of various polysaccharides on the material properties and cytotoxicity of chelate-setting β -tricalcium phosphate cement," *Phosphorus Research Bulletin*, vol. 26, pp. 59–64, 2012.
- [16] T. Konishi, S. Takahashi, and Z. Zetal, "Biodegradable β -tricalcium phosphate cement with anti-washout property based on chelate-setting mechanism of inositol phosphate," *Journal of Materials Science*, 2013.

- [17] F. H. Lin, C. J. Liao, K. S. Chen, J. S. Sun, and C. P. Lin, "Petal-like apatite formed on the surface of tricalcium phosphate ceramic after soaking in distilled water," *Biomaterials*, vol. 22, no. 22, pp. 2981–2992, 2001.
- [18] P. Ducheyne, S. Radin, and L. King, "The effect of calcium phosphate ceramic composition and structure on in vitro behavior. I. Dissolution," *Journal of Biomedical Materials Research*, vol. 27, no. 1, pp. 25–34, 1993.
- [19] M. Yamada, M. Shiota, Y. Yamashita, and S. Kasugai, "Histological and histomorphometrical comparative study of the degradation and osteoconductive characteristics of α - and β -tricalcium phosphate in block grafts," *Journal of Biomedical Materials Research B*, vol. 82, no. 1, pp. 139–148, 2007.
- [20] Y. Li, X. Zhang, and K. de Groot, "Hydrolysis and phase transition of alpha-tricalcium phosphate," *Biomaterials*, vol. 18, no. 10, pp. 737–741, 1997.
- [21] K. S. TenHuisen and P. W. Brown, "Formation of calcium-deficient hydroxyapatite from α -tricalcium phosphate," *Biomaterials*, vol. 19, no. 23, pp. 2209–2217, 1998.
- [22] M. P. Ginebra, E. Fernandez, F. C. M. Driessens et al., "The effects of temperature on the behaviour of an apatitic calcium phosphate cement," *Journal of Materials Science*, vol. 6, no. 12, pp. 857–860, 1995.
- [23] U. Gbureck, J. E. Barralet, L. Radu, H. G. Klinger, and R. Thull, "Amorphous α -tricalcium phosphate: preparation and aqueous setting reaction," *Journal of the American Ceramic Society*, vol. 87, no. 6, pp. 1126–1132, 2004.
- [24] C. L. Camiré, P. Nevsten, L. Lidgren, and I. McCarthy, "The effect of crystallinity on strength development of α -TCP bone substitutes," *Journal of Biomedical Materials Research B*, vol. 79, pp. 159–165, 2006.
- [25] C. L. Camiré, U. Gbureck, W. Hirsiger, and M. Bohner, "Correlating crystallinity and reactivity in an α -tricalcium phosphate," *Biomaterials*, vol. 26, no. 16, pp. 2787–2794, 2005.
- [26] M. Bohner, A. K. Malsy, C. L. Camiré, and U. Gbureck, "Combining particle size distribution and isothermal calorimetry data to determine the reaction kinetics of α -tricalcium phosphate-water mixtures," *Acta Biomaterialia*, vol. 2, no. 3, pp. 343–348, 2006.
- [27] T. J. Brunner, R. N. Grass, M. Bohner, and W. J. Stark, "Effect of particle size, crystal phase and crystallinity on the reactivity of tricalcium phosphate cements for bone reconstruction," *Journal of Materials Chemistry*, vol. 17, no. 38, pp. 4072–4078, 2007.
- [28] C. J. Martin and W. J. Evans, "Phytic acid-metal ion interactions. II. The effect of pH on Ca(II) binding," *Journal of Inorganic Biochemistry*, vol. 27, pp. 17–30, 1986.
- [29] B. M. Luttrell, "The biological relevance of the binding of calcium ions by inositol phosphates," *Journal of Biological Chemistry*, vol. 268, no. 3, pp. 1521–1524, 1993.
- [30] K. Ikami, M. Iwaku, and H. Ozawa, "An ultrastructural study of the process of hard tissue formation in amputated dental pulp dressed with α -tricalcium phosphate," *Archives of Histology and Cytology*, vol. 53, no. 2, pp. 227–243, 1990.
- [31] H. Oonishi, L. L. Hench, J. Wilson et al., "Comparative bone growth behavior in granules of bioceramic materials of various sizes," *Journal of Biomedical Materials Research*, vol. 44, no. 1, pp. 31–43, 1999.
- [32] M. Kitamura, C. Ohtsuki, H. Iwasaki, S. I. Ogata, M. Tanihara, and T. Miyazaki, "The controlled resorption of porous α -tricalcium phosphate using a hydroxypropylcellulose coating," *Journal of Materials Science*, vol. 15, no. 10, pp. 1153–1158, 2004.
- [33] H. Kihara, M. Shiota, Y. Yamashita, and S. Kasugai, "Biodegradation process of α -TCP particles and new bone formation in a rabbit cranial defect model," *Journal of Biomedical Materials Research B*, vol. 79, no. 2, pp. 284–291, 2006.
- [34] M. Nyan, D. Sato, H. Kihara, T. MacHida, K. Ohya, and S. Kasugai, "Effects of the combination with α -tricalcium phosphate and simvastatin on bone regeneration," *Clinical Oral Implants Research*, vol. 20, no. 3, pp. 280–287, 2009.